

DESIGN OF A MODULAR, AXIAL-FLUX DIRECT DRIVE PERMANENT
MAGNET GENERATOR FOR WIND TURBINES

A THESIS SUBMITTED TO
THE GRADUATE SCHOOL OF NATURAL AND APPLIED SCIENCES
OF
MIDDLE EAST TECHNICAL UNIVERSITY

BY

AYDIN BAŞKAYA

IN PARTIAL FULFILLMENT OF THE REQUIREMENTS
FOR
THE DEGREE OF MASTER OF SCIENCE
IN
ELECTRICAL AND ELECTRONICS ENGINEERING

JANUARY 2018

Approval of the thesis:

**DESIGN OF A MODULAR, AXIAL-FLUX DIRECT DRIVE PERMANENT
MAGNET GENERATOR FOR WIND TURBINES**

submitted by **AYDIN BAŞKAYA** in partial fulfillment of the requirements for the degree of **Master of Science in Electrical and Electronics Engineering Department, Middle East Technical University** by,

Prof. Dr. Gülbin Dural Ünver
Dean, Graduate School of **Natural and Applied Sciences** _____

Prof. Dr. Tolga Çiloğlu
Head of Department, **Electrical and Electronics Engineering** _____

Assist. Prof. Dr. Ozan Keysan
Supervisor, **Electrical and Electronics Eng. Dept., METU** _____

Examining Committee Members:

Prof. Dr. Muammer Ermiş
Electrical and Electronics Engineering Dept., METU _____

Assist. Prof. Dr. Ozan Keysan
Electrical and Electronics Engineering Dept., METU _____

Prof. Dr. Ali Nezh Güven
Electrical and Electronics Engineering Dept., METU _____

Assist. Prof. Dr. Murat Göl
Electrical and Electronics Engineering Dept., METU _____

Prof. Dr. Işık Çadircı
Electrical and Electronics Engineering Dept., Hacettepe Uni. _____

Date: 17.01.2018

I hereby declare that all information in this document has been obtained and presented in accordance with academic rules and ethical conduct. I also declare that, as required by these rules and conduct, I have fully cited and referenced all material and results that are not original to this work.

Name, Last Name : AYDIN BAŐKAYA

Signature :

ABSTRACT

DESIGN OF A MODULAR, AXIAL-FLUX DIRECT DRIVE PERMANENT MAGNET GENERATOR FOR WIND TURBINES

Başkaya, Aydın

M.S., Department of Electrical and Electronics Engineering

Supervisor: Assist. Prof. Dr. Ozan Keysan

January 2018, 154 pages

Wind energy technology is becoming more important issue in terms of renewable energy applications. Theoretical maximum of wind energy utilization is known (which is predetermined by Betz as 59%) and generally imperfections in blade manufacture reduce the actual energy yield of the turbine less than the useable energy. Therefore, maximum energy yield from generator topology is desired. According to fault statistics of wind turbines, most of the cases are related to gear-box failures. Mechanical losses and heat losses are again result from these gear-box drive train systems. In this thesis, axial flux permanent magnet direct drive (AFPM DD) topology is investigated because of its high energy yield, lower maintenance periods due to its modular direct-drive concept and axial length advantages. Proposed generator has an electrical output power of 5 MW at 12 rpm. Outer stator axial flux concept will be used in the air-cored generator. Genetic Algorithm (GA) Optimization is used in determining analytical parameters of the design. In this thesis, cost based optimization procedure is carried under 9 different wind speed conditions in order to get a more realistic design. Wind speed data are taken from

real field based measurement values of a sample wind power plant (WPP) located in Çanakkale, Turkey. The algorithm calculated the design parameters of the proposed AFPM generator based on a power generation reference of a commercial 5 MW Permanent Magnet Synchronous Generator (PMSG) wind turbine under aforementioned wind conditions. In addition, the algorithm also considers the wind speed time probabilistic and related generation incomes. In order to verify the validity of analytical design method, first a sample 50 kW AFPM design is simulated by using FEA (Finite Element Analysis) and then critical parameters such as air gap flux density, and induced emf values are compared with the analytical results. Comparison of the results of the designed generator supported the proposed analytical design method. Detailed electromagnetic and mechanical aspects of the designed 5MW/12 rpm modular generator and its simulation results are presented and verified by using FEA comparison. It is observed that in the proposed design, PMs contribute most in the total cost while PM mass is the least dominant component in total mass. Proposed generator has axial length advantage over other MW level generator counterparts although it suffers from a large diameter due to the selected direct-drive concept. Installation costs, crane costs for maintenance and installation, transportation costs and downtime costs can be reduced with modular design concept. When increasing importance of “reliability”, “modularity” and “fault-tolerance” taken into account, it is expected that the proposed modular AFPM generator system will contribute significantly in the MW level wind energy harvesting technologies both in onshore and offshore.

Keywords: Wind energy conversion, axial flux permanent magnet generator, direct drive modular generator, genetic algorithm optimization, finite element analysis (FEA)

ÖZ

RÜZGAR TÜRBİNLERİ İÇİN MODÜLER, EKSENEL AKILI DOĞRUDAN SÜRÜŞLÜ KALICI MIKNATISLI BİR GENERATÖR TASARIMI

Başkaya, Aydın

Yüksek Lisans, Elektrik ve Elektronik Mühendisliği Bölümü

Tez Yöneticisi: Yrd. Doç. Dr. Ozan Keysan

Ocak 2018, 154 sayfa

Rüzgar enerjisi teknolojisi, yenilenebilir enerji uygulamaları açısından daha önemli hale gelmektedir. Teorik olarak maksimum rüzgar enerjisi kullanımı bilinmektedir (Betz tarafından bu oran %59 olarak belirlenmiştir) ve türbin kanadı üretimindeki bozukluklar gerçek enerjiyi kullanılabilir enerjinin altına düşürmektedir. Bu nedenle, generatör topolojilerinden maksimum enerji üretimi beklenmektedir. Rüzgar türbini hata istatistiklerine göre, olayların çoğu dişli kutusu arızalarından kaynaklanmaktadır. Mekanik ve ısı kayıpları da yine aktarma organı kayıplarından kaynaklanmaktadır. Bu tez çalışmasında, eksenel akılı kalıcı mıknatıslı doğrudan sürüşlü (AFPM DD) topoloji yüksek enerji üretimi, modüler yapısı sayesinde düşük bakım periyotları ve eksenel uzunluk avantajları yüzünden araştırılmıştır. Önerilen generatör 12 rpm'de 5MW çıkış gücüne sahiptir. Hava çekirdekli generatörde, harici stator eksenel akı konsepti kullanılacaktır. Tasarımın analitik parametrelerini belirlenmesinde, genetik algoritma (GA) optimizasyonu kullanılmıştır. Bu tezde, daha gerçekçi bir tasarım elde edebilmek için, maliyet bazlı optimizasyon 9 farklı rüzgar hızı koşulu altında gerçekleştirilmiştir. Rüzgar hızı bilgisi, Çanakkale/Türkiye'de bulunan örnek bir rüzgar santralinin (WPP) gerçek

saha bazlı ölçüm değerlerinden alınmıştır. Algoritma önerilen AFPM generatör tasarım parametreleri hesaplamalarını ticari bir 5MW kalıcı mıknatıslı senkron generatörün (PMSG) yukarıda bahsedilen rüzgar koşulları altındaki güç üretim referansını baz alarak hesaplamıştır. Buna ek olarak, algoritma ayrıca rüzgar hızı istatistiklerini ve ilgili üretim gelirlerini göz önünde bulundurmıştır. Analitik tasarım yönteminin geçerliliğini doğrulamak için ilk başta örnek bir 50 kW AFPM tasarımı SEA (Sonlu Eleman Analizi) kullanılarak benzetilmiş daha sonra hava aralığı manyetik akı yoğunluğu ve endüklenen emf gibi kritik parametreler analitik sonuçlarla karşılaştırılmıştır. Tasarlanan generatörün karşılaştırma sonuçları önerilen analitik tasarım yöntemini desteklemektedir. Tasarlanan 5MW/12 rpm modüler generatörün detaylı elektromanyetik ve mekanik yönleri ve benzetim sonuçları sunulmuş ve SEA kullanılarak doğrulanmıştır. Önerilen tasarımda, kalıcı mıknatısların (PM) toplam maliyet içindeki katkısı en fazla iken PM kütesinin toplam kütle için en az baskın bileşen olduğu gözlemlenmiştir. Seçilen doğrudan sürüş konseptinden kaynaklı yüksek çapına rağmen önerilen generatörün diğer MW seviyesindeki rakiplerine göre aksel uzunluk avantajı vardır. Modüler tasarım konseptiyle; kurulum maliyetleri, kurulum ve bakım için gerekli vinç maliyetleri, taşıma maliyetleri ve devre dışı kalma maliyetleri düşürülebilir. “Güvenilirlik” , “Modülerlik” ve “Arıza-toleransı” nın artan önemi hesaba katıldığında, önerilen modüler AFPM generatör sisteminin karada ve denizdeki MW seviyesindeki rüzgar enerjisi kazanım teknolojilerine önemli katkı yapması beklenmektedir.

Anahtar Kelimeler: Rüzgar enerjisi dönüşümü, aksel akı kalıcı mıknatıslı generatör, doğrudan sürüşlü modüler generatör, genetik algoritma optimizasyonu, sonlu eleman analizi (SEA)

To my family

ACKNOWLEDGMENTS

Firstly, I would like to express my sincere gratitude to my supervisor Assist. Prof. Dr. Ozan Keysan for his continuous motivation, significant guidance and endless encouragement throughout this master thesis. I feel really lucky to be one of his first graduate students.

I wish to express my gratitude to Dr. H. Faruk Bilgin, Dr. Gökhan Şen, M. Barış Özkan and Umut Güvengir at TÜBİTAK MAM Energy Institute for their useful supports and valuable comments.

I would like to thank all my colleagues in Electrical Power Technologies Group of TÜBİTAK MAM Energy Institute, for their support, friendship and the great working environment.

I would like to thank Prof. Dr M. Timur Aydemir for his constant support and encouragement.

I express my gratitude to my invaluable friend, Reza Zeinali who was always available for discussions and help on my thesis work. I wish him great achievements during his Ph.D. studies.

I would like to thank my friends from METU Power Lab for providing me support and motivation that I need during the thesis study.

I would also like to acknowledge the support of my friends Alpsu, Tümay, Burak, Ogün, Abdullah and Yunus for their encouragement and continuous motivation.

Finally, and most importantly, I would like to express my deepest gratitude to my dear family for their enduring support and confidence in me throughout my thesis. I cannot forget my grandparents. This thesis would not be possible without their unconditional love and encouragement. I dedicate my thesis work to my family.

TABLE OF CONTENTS

ABSTRACT	v
ÖZ	vii
ACKNOWLEDGEMENTS	x
TABLE OF CONTENTS	xi
LIST OF TABLES.....	xiv
LIST OF FIGURES.....	xvi
CHAPTERS	
CHAPTER 1	1
INTRODUCTION	1
1.1. Background of Wind Energy Harvesting	1
1.2. Problem Statement and Research Objective.....	7
1.3. Thesis Outline.....	8
CHAPTER 2	11
REVIEW OF WIND ENERGY CONVERSION (WEC) SYSTEMS	11
2.1. Power Equations and Parameters	11
2.2. Challenges in WEC Systems	14
2.3. Current Wind Turbine Generator Technologies	18
2.3.1. Induction Generators.....	19
a) Squirrel Cage Induction Generators (SCIG)	19
b) Wound Rotor Induction Generators (WRIG).....	20
c) Doubly-fed Induction Generators (DFIG)	21
2.3.2. Synchronous Generators	23
a) Electrically Excited Synchronous Generators (EESG)	23
b) Permanent Magnet Synchronous Generators (PMSG)	25
2.4. Flux Orientations in PMSG Based Systems	27

2.4.1.	Radial Flux (RFPM).....	28
2.4.2.	Axial Flux (AFPM).....	29
2.4.3.	Transverse Flux (TFPM).....	38
2.5.	Importance of Modularity in WEC Systems and AFPM.....	39
2.6.	Conclusion	41
CHAPTER 3		43
DESIGN OF THE PROPOSED AXIAL FLUX GENERATOR		43
3.1.	Mechanical and Electrical Parameters.....	43
3.1.1.	Dimensions of the Proposed AFPM Generator.....	44
3.1.2.	Electromagnetic Design	52
3.1.3.	Structural Deflection	64
3.1.4.	Thermal Considerations	66
3.1.5.	Volume and Mass Equations.....	67
a)	Active Mass Calculation	68
b)	Structural Mass Calculation	69
3.1.6.	Losses.....	73
3.2.	Electromagnetic FEA vs Analytical Evaluation for Sample Dimensions	75
3.3.	Conclusion	79
CHAPTER 4		81
OPTIMIZATION AND DESIGN		81
4.1.	Introduction.....	81
4.2.	Evolutionary Algorithms (EA) and Genetic Algorithm (GA).....	81
4.3.	Genetic Algorithms Based Optimization.....	85
4.4.	Optimization Implementation	88
4.4.1.	MATLAB Toolbox and Configurations	88
4.4.2.	Flowchart and Objective Function	90
4.4.3.	Operating Conditions of the Generator	94
4.4.4.	Constants and Constraints	95
a)	Constants	95
b)	Constraints.....	98
4.5.	Optimized 5MW AFPM Generator	102
4.6.	Results.....	109

CHAPTER 5	111
FEA VERIFICATION OF ANALYTICAL DESIGN	111
5.1. Introduction	111
5.2. Magnetostatic Analysis	111
5.2.1. Magnetostatic FEA Configurations	111
5.2.2. Air gap Flux Density Verification	112
5.3. Transient Analysis	118
5.3.1. Transient FEA Configurations.....	118
5.3.2. No-load Model.....	119
a) Induced EMF Verification	119
5.3.3. Full-load Model	121
a) Phase Voltage Verification	121
b) Eddy Loss Coefficient Estimation	128
c) PM Demagnetization.....	130
5.4. Conclusion.....	132
CHAPTER 6	135
CONCLUSIONS AND FUTURE WORK	135
6.1. Proposed Model Comparison	135
6.2. Conclusions	137
6.3. Future Work.....	141
REFERENCES	143

LIST OF TABLES

Table 1-1. Recent MW level wind turbine generators worldwide.....	8
Table 3-1. Dimensions of the proposed AFPM generator at side view.....	44
Table 3-2. Dimensions of the proposed AFPM generator pole at counter view.....	46
Table 3-3. Dimension of the proposed AFPM generator coil at counter view.....	49
Table 3-4. Optimized design parameters of the sample 50 kW generator.....	74
Table 3-5. Comparison of the critical parameters of analytical and FEA results for the sample AFPM design.....	77
Table 4-1. Configuration parameters of the MATLAB optimization toolbox.....	85
Table 4-2. Independent variables of the optimization.....	87
Table 4-3. Wind speed distributions and reference generator ratings.....	92
Table 4-4. Conceptual optimization constants of the proposed AFPM generator..	93
Table 4-5. Material constants of the proposed AFPM generator.....	94
Table 4-6. Objective function penalty table.....	97
Table 4-7. Optimized generator independent variables at 12 rpm/5MW.....	100
Table 4-8. Optimized generator performance ratings.....	103
Table 4-9. The most salient features of the proposed AFPM generator at 12 rpm..	116
Table 5-1. Magnetostatic FEA configurations.....	109

Table 5-2. Comparison of the analytical and FEA results for the air gap flux density.....	114
Table 5-3. Transient FEA configurations.....	116
Table 5-4. Comparison of the analytical and FEA results for the induced emf per-phase.....	117
Table 5-5. Comparison of the analytical and FEA results for the phase voltage....	120
Table 5-6. Properties of the first 10 voltage harmonics of winding-1.....	122
Table 5-7. Properties of the first 10 voltage harmonics of winding-2.....	123
Table 5-8. Properties of the first 10 voltage harmonics of winding-3.....	124
Table 6-1. Properties of commercial wind turbine generator systems including the proposed generator.....	130

LIST OF FIGURES

Fig.1-1. Worldwide yearly installed wind capacity 2001-2016.....	2
Fig. 1-2. Worldwide total installed wind capacity 2001-2016.....	2
Fig. 1-3. Global wind energy market forecast.....	3
Fig. 1-4. Cumulative installations for wind power plants in Turkey.....	3
Fig. 1-5. Evolution of wind turbines.....	4
Fig. 1-6. Wind turbine types according to rotation axis (a) horizontal axis (b) vertical axis	5
Fig. 1-7. Conventional geared (left) and direct drive (right) wind turbines.....	7
Fig. 2-1. Wind speed probability density functions for Bozcaada region.....	12
Fig. 2-2. Failure frequency and downtime for different part of wind turbine.....	14
Fig. 2-3. NEG Micon wind turbine with gearbox.....	15
Fig. 2-4. Enercon E-66 wind turbine without gearbox.....	17
Fig. 2-5. SCIG Danish concept wind turbine schematic.....	18
Fig. 2-6. SCIG with back-to-back VSC converter.....	19
Fig. 2-7. WRIG schematic diagram.....	20
Fig. 2-8. Conventional grid connected DFIG, RSC: Rotor side converter, GSC: Grid side converter.....	21

Fig. 2-9. Market share of different wind turbine generators for Europe between 2006 and 2015.....	22
Fig. 2-10. Enercon E-126 EP4, 4.2 MW wind turbine during the installation.....	23
Fig. 2-11. EESG-Electrically Excited Synchronous Generator grid connection.....	23
Fig. 2-12. Permanent magnet synchronous generator with gear-box and full scale power electronic converter.....	24
Fig. 2-13. Multibrid M5000 5MW wind turbine generator (Courtesy of Multibrid and Areva).....	25
Fig. 2-14. Schematic of direct-driven PMSG.....	26
Fig. 2-15. RFPM with surface mounted permanent magnets.....	27
Fig. 2-16. RFPM with buried permanent magnets for flux concentration.....	28
Fig. 2-17. Conventional internal rotor RFPM complete view.....	28
Fig. 2-18. Classification of AFPM generators.....	30
Fig. 2-19. Single sided configuration of AFPM (single stator and single rotor).....	31
Fig. 2-20. Non slotted TORUS axial flux permanent magnet overview (left) and path of generated flux by permanent magnets (right).....	32
Fig. 2-21. NN-type slotted TORUS axial flux permanent magnet overview (left) and path of generated flux by permanent magnets (right).....	33
Fig. 2-22. NS-type slotted TORUS axial flux permanent magnet overview (left) and path of generated flux by permanent magnets (right).....	33
Fig. 2-23. NS-type coreless TORUS axial flux permanent magnet overview.....	34
Fig. 2-24. Slotless AFIR overview (left) and path of generated flux by permanent magnets (right).....	34
Fig. 2-25. Slotted AFIR overview (left) and path of generated flux by permanent magnets (right).....	35

Fig. 2-26. Multistage AFPM generator.....	36
Fig. 2-27. Coreless multistage AFPM generator flux path.....	37
Fig. 2-28. Transverse flux machine view.....	38
Fig. 2-29. Transverse flux machine three dimensional flux path.....	38
Fig. 3-1. 4-pole section of the proposed axial flux PM generator.....	42
Fig. 3-2. Induced voltage variation with respect to different τ_c/τ_p ratios.....	43
Fig 3-3. C-shaped core from side view with defined dimensions in Table 3-1.....	45
Fig. 3-4. Counter view of one pole of the generator core limb.....	46
Fig. 3-5. Effect of higher α_i in terms of leakage flux from the top view of the generator.....	48
Fig. 3-6. C-core coil with inner and outer length ratios at counter view.....	49
Fig. 3-7. Side view of the C-core for reluctances and flux paths.....	50
Fig. 3-8. Permanent magnet reluctance components.....	52
Fig. 3-9. Top view of the C-cores for reluctances and flux paths included leakage effect.....	52
Fig. 3-10. Leakage reluctance network.....	53
Fig. 3-11. Calculated airgap flux density square waveform (grey) and its sinusoidal fundamental frequency component (blue).....	57
Fig. 3-12. Equivalent circuit of the synchronous machine where E_a is the induced emf, I_a is the phase current, X_s is the synchronous reactance and V_t is the phase terminal voltage.....	58
Fig. 3-13. Phasor diagram of synchronous machine with load angle (δ) and power factor angle (Φ).....	58

Fig. 3-14. Positions of the conductors in the winding from top view. Shaded regions represent the effective window area.....	60
Fig. 3-15. C-core deflection due to attraction forces, deflected cores are shown with red dashed lines.....	63
Fig. 3-16. a) Beam model for the C core deflection. b) Model for uniformly distributed load (w_{udl}) is applied at $a=0$ c) Model for uniformly distributed load (w_{udl}) is applied at limited a units along the beam	63
Fig. 3-17. Proposed axial flux PM generator side view with three axial stacks.....	67
Fig. 3-18. Balanced and unbalanced forces of c-core limbs, left: inner limb case, right: outer limb case.....	67
Fig. 3-19. Torque arm structure with 6 arms and Top view of steel hollow bar dimensions.....	68
Fig. 3-20. Steel band.....	70
Fig. 3-21. Trapezoidal winding distances.....	71
Fig. 3-22. Airgap flux density vectors for the sample 50 kW design.....	75
Fig. 3-23. Airgap flux density graph with analytical results for the sample 50 kW design.....	76
Fig. 3-24. Induced emf per phase graph for the sample 50 kW design.....	76
Fig. 4-1. Classification of the search techniques.....	80
Fig. 4-2. Bit string cross-over operation between parent individuals.....	81
Fig. 4-3. Bit string mutation operation.....	81
Fig. 4-4. General flowchart of a GA optimization.....	84
Fig. 4-5. Optimization flowchart.....	90
Fig. 4-6. Wind speed density distribution from measurement data.....	91

Fig. 4-7. Best fitness variation.....	101
Fig. 4-8. Fitness distribution of the optimization individuals according to iterations.....	101
Fig. 4-9. Proposed AFPD generator whole machine view without structural parts.....	104
Fig. 4-10. Mass components of the optimized AFPD generator.....	105
Fig. 4-11. Material cost components of the optimized AFPD generator.....	105
Fig. 5-1. Magnetostatic model mesh plot.....	109
Fig. 5-2. Air gap flux density measurement lines side view.....	110
Fig. 5-3. Air gap flux density measurement lines top view.....	110
Fig. 5-4. Air gap flux density graph from FEA.....	111
Fig. 5-5. Airgap flux density vectors for the 5 MW design.....	111
Fig. 5-6. Airgap flux density vectors on the virtual sheet (side view).....	112
Fig. 5-7. Airgap flux density vectors on the virtual sheet (top view).....	112
Fig. 5-8. Flux density magnitude distribution over the steel cores of the design...	113
Fig. 5-9. Flux density magnitude distribution over the virtual sheet.....	113
Fig. 5-10. Airgap flux density graph with analytical results for the 5 MW design..	115
Fig. 5-11. FEA induced emf (E_a) measurement equivalent circuit.....	116
Fig. 5-12. Proposed design induced emf per phase results from FEA.....	117
Fig. 5-13. Full-load phase voltages and currents.....	118
Fig. 5-14. Proposed design phasor diagram including resistance.....	119
Fig. 5-15. Phase voltage waveforms imported from FEA to Simulink.....	121
Fig. 5-16. Simulation block in MATLAB/Simulink.....	121

Fig. 5-17. Harmonic component magnitudes and THD for winding-1 voltage.....	122
Fig. 5-18. Harmonic component magnitudes and THD for winding-2 voltage.....	123
Fig. 5-19. Harmonic component magnitudes and THD for winding-3 voltage.....	124
Fig. 5-20. Eddy loss calculated for the one block unit of PM in FEA.....	126
Fig. 5-21. Eddy current density vectors on magnet block.....	126
Fig. 5-22. Three phase short circuit fault schematic representation for the proposed system.....	128
Fig. 5-23. Demagnetization curve of the selected N50 grade PM.....	128
Fig. 5-24. Three phase short circuit current waveforms.....	129
Fig. 5-25. H field intensities under three phase short circuit condition in FEA.....	129

CHAPTER 1

INTRODUCTION

1.1. Background of Wind Energy Harvesting

Like many developments in technology, modern wind energy utilization by means of wind turbines started 40 years ago due to search for alternative energy sources except oil, whose deficiency and high prices were a global crisis issue. Besides, air pollution and other environmental problems made it indispensable to search for clean and renewable energy sources such as wind. To summarize, OPEC crisis in 1970s and environmental problems worked as a catalyst in development progress of wind turbines. First wind turbines were operating at fixed speed and their structure was very simple. This concept of Squirrel Cage Induction Generator (SCIG) was called later as “Danish concept” and became a milestone for modern wind turbines. Nowadays, there are different types of wind turbines exist in the market both in mechanical and electrical aspects. Global trend is going above 5MW of output power and especially generator technologies are under development in order to maximize produced energy [1]–[3].

Global annual and cumulative installed wind capacities between 2001 and 2016 are given in Fig. 1-1 and 1-2, respectively. As it can be seen from graphs, wind energy harvesting has an increasing trend.

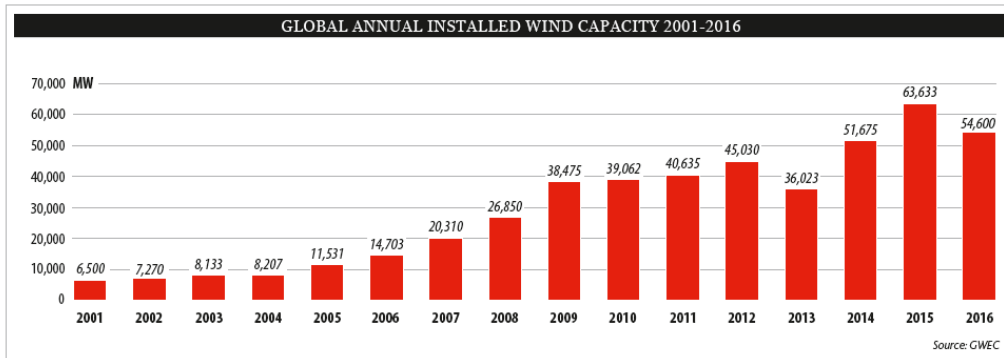


Fig. 1-1. Worldwide yearly installed wind capacity 2001-2016 [4]

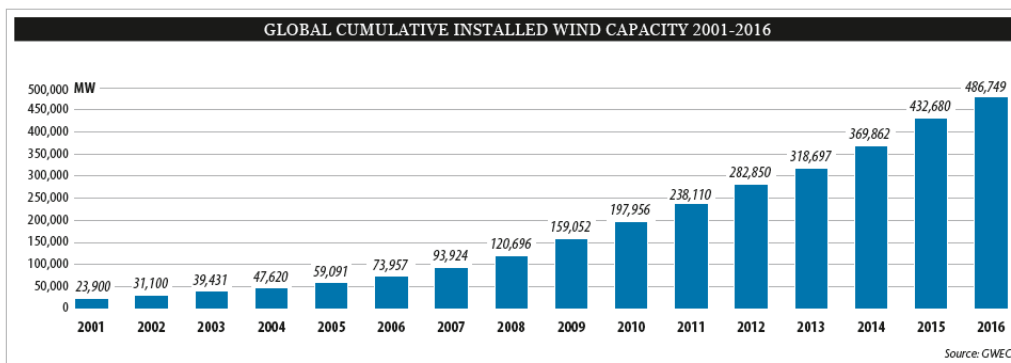


Fig. 1-2. Worldwide total installed wind capacity 2001-2016 [4]

According to annual market update report of Global Wind Energy Council (GWEC), it's expected to reach 791 GW of global cumulative wind energy capacity by 2020, although it's estimated that annual capacity growth rate will be stabilize around five percent level. Detailed market forecast of GWEC for 2016-2020 is given in Fig. 1-3.

Rise in the usage of wind energy in Turkey is very similar to global trends. Wind energy sources, contributed about 6% of Turkey's total electricity demand in 2015 [5]. Turkey has nearly stable increase rate of installation rate of wind power plants for past 5 years. Fig. 1-4 shows the variation of cumulative installations for wind power plants in Turkey. According to Turkish Wind Energy Association (TWEA), it's expected to reach total installed capacity of 10 GW, under the current regulatory framework. Turkey's total wind capacity is predicted more than 48 GW from zones with over 7 m/s speed at 50 meters altitude [5].

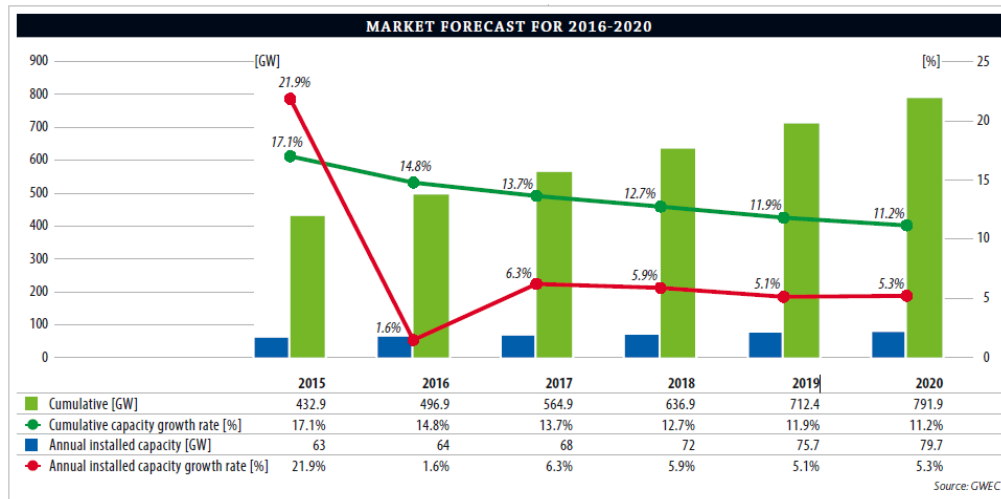


Fig. 1-3. Global wind energy market forecast [5]

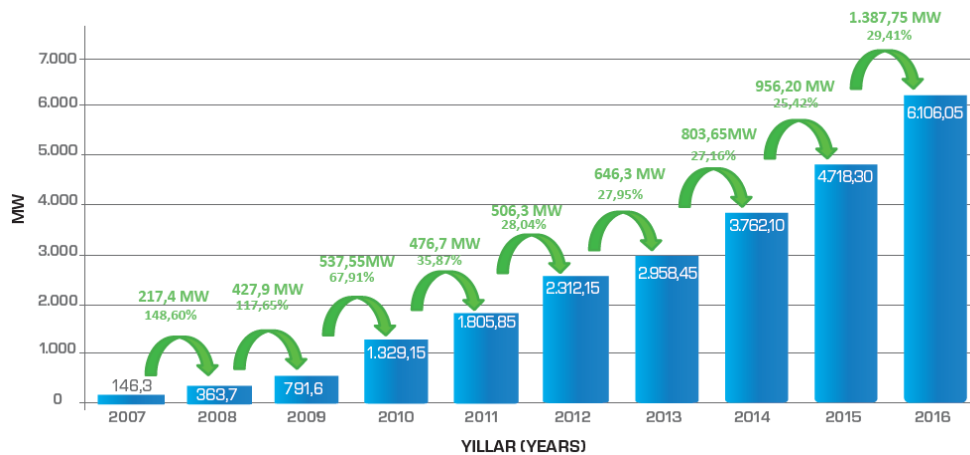


Fig. 1-4. Cumulative installations for wind power plants in Turkey [6]

Wind turbine design is an important issue for renewable energy. Especially during the last decade, its technology is substantially matured with variable speed applications. Although there are physical and aerodynamical limitations due to natural causes of wind phenomenon, different arrangements of wind turbine generator systems are invented to maximize the captured energy. By this improved technologies both in power electronics and generators, manufacturing and installation costs are reduced. Therefore, wind energy harvesting concepts started to penetrate the global markets. According to [7], today 83 countries use wind energy

harvesting applications commercially and 24 countries have installed wind power capacity of more than 1GW. Evolution of wind turbine sizes and fraction of power electronics stage capacities can be seen in Fig. 1-5. As the sizes and power levels of wind turbines are increased, importance of efficiency and grid connection subjects also increased. Because wind power plants gradually becomes inevitable parts of electrical grids in most countries and they are expected to conform the grid codes and fault ride through capabilities.

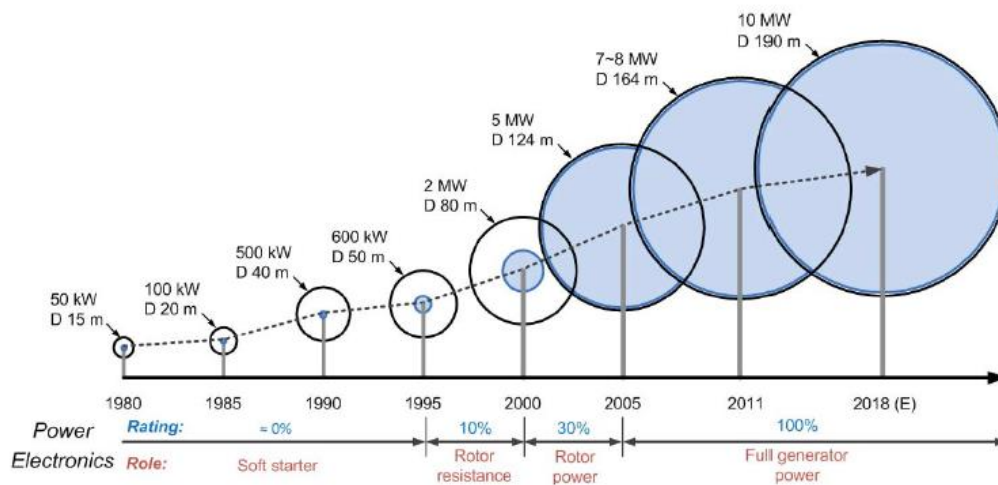


Fig. 1-5. Evolution of wind turbines [8]

When designing and investing a wind power stations, 3 main properties which are necessary to validate are given as follows:

- Low cost
- Long-lasting
- Low service requirement

If we go in detail of these conditions from the engineering point of view, lightweight, low cost, low speed, high torque and variable speed operation should be considered during the design stage of wind power plant (WPP) [9]. Wind turbine generators dominating the markets nowadays have MW-level power output capacity in average. Gearboxes are used in order to pair the low speed hub with the high speed generator shaft. However, gearboxes result in high mechanical wear, decreased

efficiency and lower life-span. Therefore, wind energy systems with geared drivetrain need regular maintenance. Low-speed generators and direct drive systems are introduced in order to omit the gearbox and increase the overall efficiency [7]. Higher overall efficiency, lower noise, reliability and reduced maintenance costs are the main advantages of direct drive concept. Direct drive solutions offer simpler and more efficient structures for drivetrain of wind turbines, therefore smaller nacelle can be obtained. One disadvantage of direct drive concept is that they have larger diameters than conventional geared wind turbines in order to provide same output power in low speeds. In addition, using modern rare-earth permanent magnets such as NdFeB, higher energy densities become reachable and more powerful novel generators can be manufactured. Generators with permanent magnets will be covered more detailed in the next chapter. In this study, direct drive axial flux permanent magnet topology is chosen to design among other topologies.

Wind turbines can be categorized into two types according to their rotational axis position:

- Horizontal axis wind turbines (HAWT), example of it is given in Fig. 1-6 (a)
- Vertical axis wind turbines (VAWT) example of it is given in Fig. 1-6 (b)



(a)



(b)

Fig. 1-6. Wind turbine types according to rotation axis (a) horizontal axis (b) vertical axis

As the name refers, in HAWTs, shaft axis is parallel with ground while in VAWTs shaft axis is perpendicular to ground. Horizontal axis wind turbines are dominant in the market due to its robust structure and high overall efficiency. Vertical axis turbines are generally used in small wind applications in levels of kW. In vertical axis wind turbines, angle of strike of the air is inherently varies with the rotation and it's hard to capture energy especially under unbalanced wind flow conditions, while pitch and yaw control of the turbine can be successfully implemented in horizontal axis turbines.

Another important issue is the speed control of these turbine blades in terms of aerodynamic means. At this point two main control techniques exist: stall control and pitch control. Generally in stall controlled technique, turbine blades are fixed aerodynamic structures and these turbines need high peak torque to limit turbine speed while in pitch control technique, blade pitch angle can be changed during operation of turbine i.e. angle of attack of air can be adjusted therefore these turbines do not need over torque for limit the speed [10]. In variable speed applications pitch control is a commonly used technique [11].

A usual wind turbine consists of turbine blades and shaft, gearbox and the generator. The main generators used in wind turbines are synchronous and induction generator concepts. In conventional applications, a gearbox is connected between turbine shaft and generator and used for increasing the low speed of turbine blades to high speed of generator. In direct drive wind turbines, the generator is directly coupled to main shaft of the turbine and operates at low speeds. Geared and direct drive schematics of wind turbines are shown in Fig. 1-7. Wind turbines can be categorized into three main groups according to generator rotational speed. These are fixed speed, limited variable speed and variable speed [12]. Although the first examples of wind turbines were generally fixed speed ones like the Danish concept, modern wind turbines nowadays use variable speed concept because of higher power and higher torque advantages. More detailed explanations and schematics about categorizing wind turbines according to their drivetrain, generators and flux orientations will be given in the next chapter.

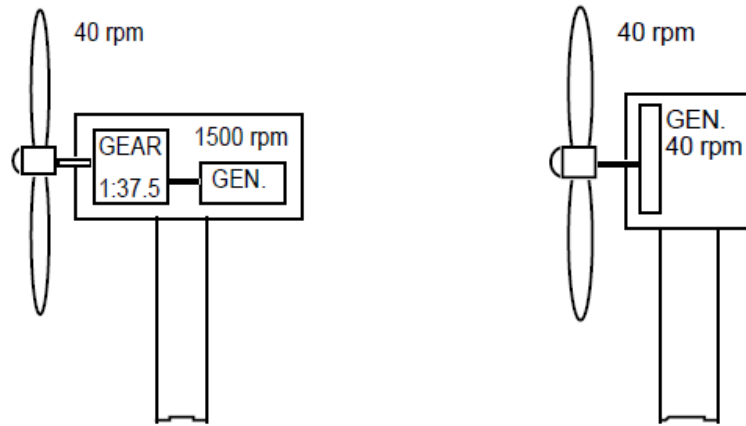


Fig. 1-7. Conventional geared (left) and direct drive (right) wind turbines [13]

1.2. Problem Statement and Research Objective

As the wind energy conversion systems become more capable player of the global energy sector and installed capacities of the WECs increased every year, reliability for these systems becomes more important issue. Especially with the increased power rates of these turbines, size and volumes also increase and modularity becomes vital.

In this thesis work, a Direct Drive Axial Flux Permanent Magnet wind turbine generator (AFPM-DD) is chosen and designed because of its high reliability, high torque density and volume advantages. The designed and proposed generator has an output power of 5 MW. Gearless drive train is chosen especially for increased overall efficiency and reduced maintenance costs. The proposed generator also has a modular structure, thus reliability and high efficiency is desired even in a fault-state. Parameters of the designed machine will be chosen according to genetic algorithm optimization and FEA validation. Also in this study, the proposed generator system is compared with its MW level counterparts in the last chapter. Table 1-1 shows the recent MW level wind turbine models with respect to their brand, origin, generator type and output power [14]–[23]. Based on these table values, it can be said that the trend is going towards 10 MW per turbine in a few years. When increasing importances of “reliability”, “modularity” and “fault-tolerance” are taken into account, it is expected that the proposed generator system

and its comparison with existed commercial counterparts will contribute significantly in the MW level wind energy harvesting technologies.

Table 1-1. Recent MW level wind turbine generators worldwide [14]–[24]

Brand	Origin	Power Level (MW)	Type	Drivetrain
Sinovel	China	1.5 - 6.0	DFIG	3 stage gearbox
Vestas	Denmark	3.45	PMSG	3 stage gearbox
		1.8 – 3.0	DFIG	
MHI-Vestas	Denmark	4.2 – 9.5	PMSG	3 stage gearbox
GE Wind	US	1.7- 3.8	DFIG	3 stage gearbox
		6.0	PMSG	Direct Drive
Goldwind	China	1.5 – 2.5	PMSG	Direct Drive
Gamesa	Spain	2 – 3.3	DFIG	3 stage gearbox
		5	PMSG	2 stage gearbox
Enercon	Germany	0.8 – 7.78	EESG	Direct Drive
Nordex	Germany	1.5 – 3.9	DFIG	3 stage gearbox
Siemens Wind	Germany	2.3 – 3.2	PMSG, SCIG	Gearbox
		3.3 – 8		Direct Drive
Suzlon	India	0.6 – 2.1	DFIG	3 stage gearbox
Senvion	Germany	2.0 – 3.6	DFIG, SCIG and EESG	3 stage gearbox
		6.2		

1.3. Thesis Outline

In Chapter 2, general overview of wind energy conversion systems and challenges in this area will be summarized. For this purpose, generator systems used in wind energy conversion systems will be classified according to electrical and mechanical aspects. Importance of modularity will be described. Finally, chosen direct drive AFPM generator system will be explained and advantages and disadvantages of it will be evaluated.

In Chapter 3, detailed analytical design equations of the proposed AFPM generator will be described and related drawings will be given. Following this chapter, FEA results and analytical calculation results for the sample 50 kW AFPM generator will be compared and results will be discussed in order to check the accuracy of the analytical design methodology proposed in this thesis.

In Chapter 4, optimization process will be introduced and optimized parameters of the proposed AFPM generator will be presented. First, evolutionary algorithm and nature of the genetic algorithm will be described. Then all details of the optimization procedure followed in this thesis will be described. Finally, optimized design parameters and analytically calculated performance values of the proposed 5MW 12 rpm generator will be presented. Discussion of the mass and cost components of the proposed design will be given at the end of this chapter.

In Chapter 5, finite element analysis of the proposed design is reviewed and results of this analysis will be compared with analytically calculated design parameters in order to verify the proposed AFPM design.

In Chapter 6, comparison of the proposed generator with similar MW-level wind turbine generators on both market and academic works will be presented in terms of power and torque density. Finally, conclusions and future works about this thesis study will be discussed.

CHAPTER 2

REVIEW OF WIND ENERGY CONVERSION (WEC) SYSTEMS

In the previous chapter, background of wind energy conversion systems is introduced and related wind energy statistics are summarized and tabulated. In this chapter, detailed survey of wind energy fundamentals and general overview of wind energy conversion systems will be summarized. To accomplish this, Chapter 2 is divided into five main parts. In the first part, wind power equations and key parameters will be discussed. This data especially used in wind turbine investment calculations and wind potential estimation techniques. Then challenges in wind energy conversion systems will be introduced and common problems will be addressed. In the next part, existing wind turbine technologies will be classified and evaluated according to their mechanical and electrical aspects. Then three main flux orientations in PM based systems will be shown and explained. Finally, the importance of modularity in wind energy conversion systems and the advantages and the disadvantages of axial flux PM machines will be evaluated. Also in the last part, reasons for choosing direct drive axial flux permanent magnet generator concept will be explained.

2.1. Power Equations and Parameters

The available shaft power (output power) P from a horizontal axis wind turbine can be expressed as a function of the wind speed as follows:

$$P = \frac{1}{2} \rho_{air} C_p(\lambda, \beta) \pi r^2 v^3 \quad (2-1)$$

where , ρ_{air} is the mass density of air , C_p is the power coefficient which is a function of the tip speed ratio λ and the pitch angle β , r is radius of the turbine blade and v is the wind velocity. Power coefficient, sometimes called performance coefficient, can be defined as the ratio of the captured wind power to the available input power of the wind. Therefore, it tells us how efficient the turbine is. Generally

imperfections in blade manufacture reduces the actual energy production of the turbine lower than the useable energy. Theoretically, maximum 59% (approximately 16/27) of the wind energy can be captured by an ideal wind turbine. This result is concluded by German physicist Albert Betz in 1919. This limitation is valid for both vertical and horizontal axis wind turbines. Maximum value of performance coefficient (C_p) is limited by Betz criterion. Since physical limitations exist in nature such as friction and other mechanical losses, maximum value of the performance coefficient C_p is always lower than theoretical maximum of Betz constant.

In [25], power coefficient is defined as a nonlinear function of TSR (λ) and pitch angle (β) as follows,

$$C_p(\lambda, \beta) = C_1 \left(\frac{C_2}{\lambda_i} - C_3\beta - C_3 \right) e^{\frac{-C_5}{\lambda_i}} + C_6\lambda \quad (2-2)$$

where,

$$\frac{1}{\lambda_i} = \frac{1}{\lambda + 0.08\beta} - \frac{0.035}{\beta^3 + 1} \quad (2-3)$$

These coefficients shown above depend on the turbine physical characteristics. Investigation of these values is out of scope of this thesis. Tip speed ratio (TSR- λ) is defined as a ratio of linear tip speed of turbine blade to wind speed as shown in Eq. (2-4). This ratio is very useful when designing a wind turbine. Optimal TSR is desired to obtain maximum power from wind as much as possible.

$$\lambda = \frac{R\omega_M}{v} \quad (2-4)$$

where, v is the wind speed, ω_m is the rotational rotor speed and R is the rotor radius. TSR is a kind of measurement of how fast turbine blades rotate. Until a proper limit, higher rotational speeds leads to higher output power levels. Therefore, high TSR is aimed when designing a wind turbine. Each wind turbine has unique value of TSR regardless of the generator topology used in manufacture [26]. Approximate optimal TSR for a conventional three blade wind turbine system is given as 5~6 in [27].

Minimum wind speed that is needed to start to rotate the blades is cut-in wind speed, while the cut-out speed is the maximum speed of wind that turbine is allowed to

continue operation. Intermittent nature of the wind determines the production variation of the WECs. There are some approaches for estimate the wind profile at a given place. Weibull distribution is used to represent the wind speed distribution and it indicates the occurrence frequency of the wind speeds according to time for a given site measurement. This indication is required because of the probabilistic nature of wind. Weibull distribution and Rayleigh distributions are used to estimate and analyze the wind speed distribution. IEC 61400 standard, which is specialized for design requirements of wind turbine, mentions Rayleigh and Weibull distributions as the most common distributions for wind profile [28]. Weibull (F_w) and Rayleigh (F_R) cumulative probability functions are given in Eq. (2-5) and Eq. (2-6), respectively.

$$F_w(v) = 1 - \exp\left[-\left(\frac{v}{c}\right)^k\right] \quad (2-5)$$

$$F_R(v) = 1 - \exp\left[-\left(\frac{\pi}{4}\right)\left(\frac{v}{v_m}\right)^2\right] \quad (2-6)$$

where v , v_m , c and k are wind speed, mean wind speed, scale parameter and shape parameters. In Rayleigh distributions, shape parameter is equal to 2 and mean wind speed value is required. In [29], authors calculate the wind speed probability density values of the Bozcaada region of Turkey from both time series measured data and distributions of Weibull and Rayleigh. This distribution can be seen in Fig. 2-1.

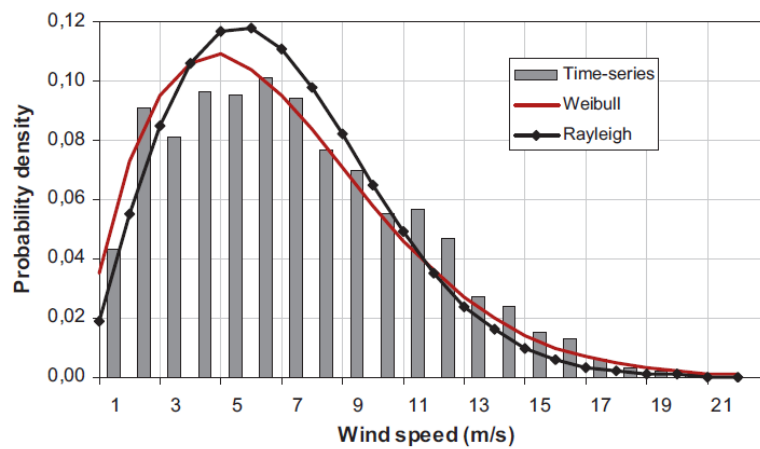


Fig. 2-1. Wind speed probability density functions for Bozcaada region [29]

2.2. Challenges in WEC Systems

Main focus and effort during the design and implementation of wind turbines is to obtain more efficient and cost effective solutions hence to reduce the cost of energy, which can be considered as a key issue. Therefore, every detail about machine design, grid connection and other technical trend parameters have to fulfill this economical objective.

As the power scales of wind turbines increase, penetration of these energy sources into electrical grid becomes inevitable. Demand side management techniques and different storage technologies such as flywheels and batteries are developed for grid connection and disturbance support such as short term fluctuations. This integration dictates wind turbines to conform the grid codes in which quality and requirements of power plants are described in terms of frequency and voltage support. Therefore, modern wind turbines with high power capacities have to keep connected and support grid in terms of voltage regulation and reactive power during the disturbances. This ability is also called low voltage ride through (LVRT) capability.

Another important challenge about wind turbines is the ease of maintenance. Reliability is related to failure rates of different parts of a wind turbine. Thus performance of every component of wind turbine determines the reliability of the wind turbine. Especially, for offshore wind turbines where access for repair and maintenance is difficult, improving reliability becomes an important key parameter during the design [30]. For example, mechanical parts which have high withstand ability for humidity is preferable for offshore wind turbines. Failure rates and corresponding downtimes for different parts of generator are obtained in [30] and given in Fig. 2-2. According to this statistics based on collected data, it can be concluded that main failures and longest downtimes result from gearboxes and electrical systems.

As a rule of thumb in generator design it is important to avoid gearbox because of its mechanical parts and need for periodic maintenance and lubrication. Increased maintenance periods are big advantage for wind turbines whose locations are hard to reach such as offshore wind turbines [31]. Drivetrain of a VSCF (variable speed constant frequency) turbine generally consists of blades, low and high speed shafts,

gear-box and generator. Turbine shaft can be referred as low speed shaft while generator shaft is referred as high speed shaft. Gearbox in a wind turbine system is responsible of transmission of aerodynamic power from turbine to the generator shaft. In geared type of generator, turbine blades with hub structure connected to shaft of the generator via a gear-box, which increases the rotational speed of the low-speed shaft. Gearbox allows generator to operate at high speeds, therefore smaller diameters can be used with same amount of torque needs. Gear ratio is a measure of relationship between output and input speeds of dynamic system. Drawings of nacelles of two commercial wind turbines which are geared and gearless are given in Fig. 2-3 and Fig. 2-4, respectively.

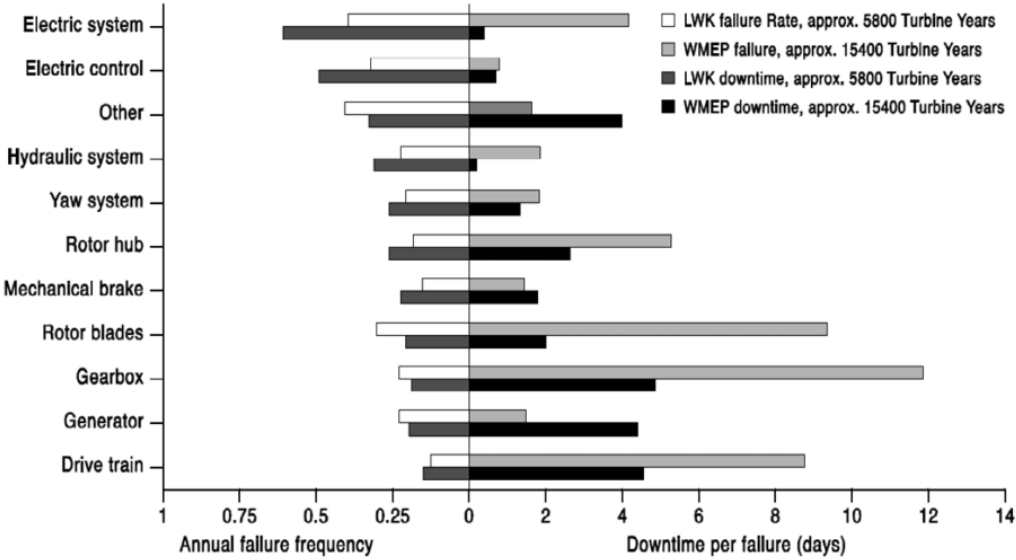


Fig. 2-2. Failure frequency and downtime for different part of wind turbine [30]

Gearboxes are the main source of mechanical faults and losses in wind turbine systems. Also, it's necessary to make regular maintenance for gearbox components in order to avoid an unexpected failure. Moreover, they result in mechanical and thermal losses hence reduced efficiency. Environmental drawback of the gearbox is audible noise created by mechanical parts [12]. Because of these reasons, manufacturers and designers start to develop gearless drive systems for wind turbines from early 1990s. However, geared systems still offer cheaper solutions than large diameter direct drive systems [32].

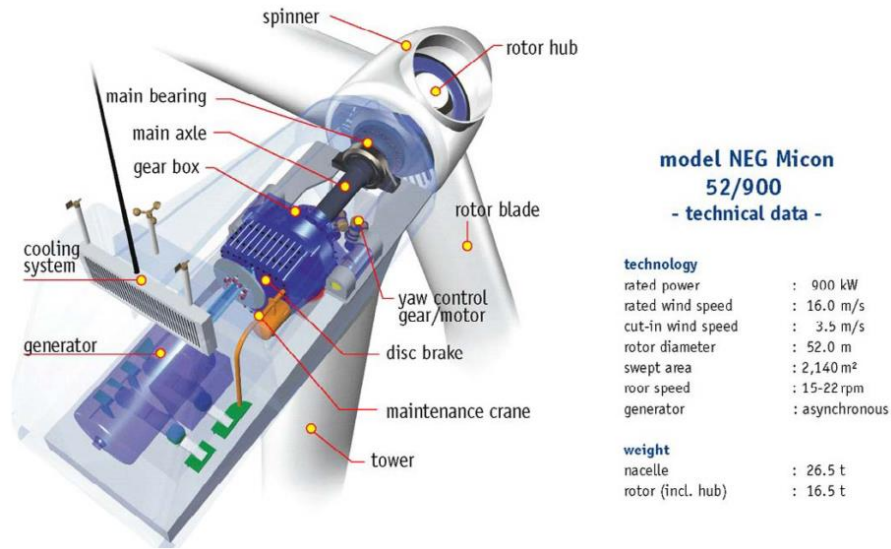


Fig. 2-3. NEG Micon wind turbine with gearbox [30]

As the name refers, in direct drive generators gearbox and all bearing structures are eliminated. Therefore, turbine blades and generator are connected on the same shaft rotating at low speed. With this eliminated gearbox and other mechanical structures, direct drive systems offer lower maintenance cost, increased efficiency and reliability. The main purposes of the direct-drive concept for wind turbines are;

- to increase the efficiency thus energy yield
- to decrease the gearbox failures
- to reduce the maintenance cost

In electrical generator design, one of the main criterion is torque. Due to tip speed limitation and natural result of gearless topology, direct drive wind turbine generators rotates at low speed. Relationship between power and torque according formula which defines the output power of generator:

$$P = T \cdot \omega_m \quad (2-7)$$

where, P is the output power, T is the torque and ω_m is the mechanical speed of the shaft. Torque must be increase inversely proportional to decrease of angular speed in direct drive generators in order to produce same amount of power as in the geared drive case. In some designs ratio of axial length to air gap diameter, k is optimized

[33]. According to [34], electromagnetic torque of an axial flux permanent magnet machine is proportional to outer diameter as shown in Eq. (2-8).

$$T \sim D_{out}^3 \quad (2-8)$$

To do that when scaling up the turbine sizes, amount of material should be increased in order to maintain the air-gap against magnetic attraction forces between stator and rotor parts. This means direct drive machines are heavier and larger in diameter rather than other types of machines in order to produce the same amount of power. More material also means extra cost, which is a disadvantage for this type of generators. Torque per volume and torque per mass parameters are important during the design of the generator systems. EESG and PMSG are two main direct drive solutions exist in the market. One of the commercial direct drive EESG of Enercon is shown on Fig. 2-4. Radial flux orientation is mostly preferred among direct drive generators [31]. However RFPM can be disadvantageous when allocated space for generator is limited for specific applications such as nacelle or electric vehicle wheel motor. Transverse flux PM generators can produce higher torques with lower copper losses. However complicated construction is an important penalty for transverse flux option, especially when maintenance problems are taken into account. Direct drive axial flux type permanent magnet machines are advantageous in torque to volume ratio among other machine topologies while torque per mass values are not much attractive. Torque per volume advantage is due to shorter axial length and compact structure rather than radial flux counterpart. Torque per mass disadvantage is related to large diameter which is a penalty of this type of generators. Because of reasons aforementioned above, trend is going through the high torque direct drive generators as it eliminates gearbox losses and minimizes maintenance and repair cost. Therefore, overall efficiency and reliability of the system can be increased.

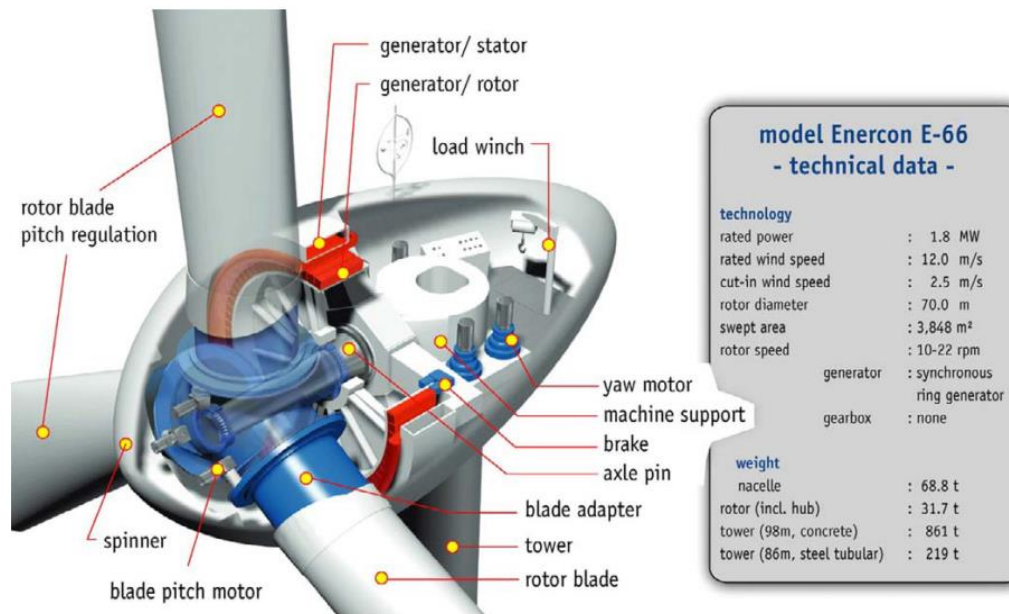


Fig. 2-4. Enercon E-66 wind turbine without gearbox [30]

Modularity on the other hand, is related to availability of maximum portion of mechanical or electrical structure of generator during the failure periods. With the rapidly increased power levels of 5 MW and above for per turbine, nowadays trend is going through the modular multi-level power electronic converters and modular machine structures for large wind turbine generators [1]–[3]. Mechanical modularity can be considered as operating parallel machines instead of one bulky generator. Contrary to conventional generators, modular generators have the ability of continue to operate with its healthy modules under fault conditions of defective modules. Therefore, reliability and overall efficiency is increased. Challenges for increasing efficiency of wind turbines from the control point of view can be considered as fault monitoring and diagnostic, forecasting error and predictive controls [35].

2.3. Current Wind Turbine Generator Technologies

In this section, generators are categorized according to their mechanical and electrical properties. In mechanical categorization, drivetrain approach is considered ie. whether drivetrain includes gearbox or not. In electrical categorization, most used generator types in WECs namely induction and synchronous generators are

considered in terms of wind turbine point of view. Thus, main approach in this part when describing their properties is based on whether they are induction or synchronous generators. Wind turbines are mainly categorized in the literature according to their rotational speeds. These speed categories are fixed speed, limited variable speed or variable speed. Variable speed configuration is the most used one among other speed options because it's more grid-supportive by means of power electronic converter it provides [11]. These type of turbines are capable of operating at different wind speeds and more flexible in terms of torque and reactive power control [12].

2.3.1. Induction Generators

a) Squirrel Cage Induction Generators (SCIG)

This type of generator can be used with both fixed (also known as Danish Concept) and variable speed. However, SCIGs are commonly used for constant speed operation. The most common configuration of this generator consists of three stage gearbox connected to SCIG and compensating capacitors [30]. Generator speed is determined according to grid electrical frequency. Sometimes soft-starter can be used after the generator for smoother grid connection [36]. This type of SCIG is given in Fig. 2-5.

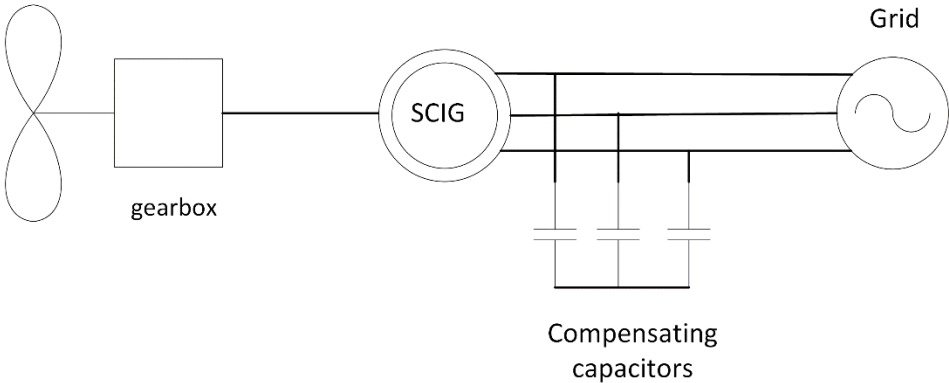


Fig. 2-5. SCIG Danish concept wind turbine schematic [36]

Robustness, off-the-shelf parts, lower investment costs, stable operation and lower maintenance makes SCIG preferable in WECs. But in order to get more efficient

operation SCIG should be constructed with low number of poles because high number of poles construction becomes a mechanical drawback for SCIG. Besides, high number of poles leads to higher leakage flux losses in practical. Therefore gear-boxes are generally used with SCIGs. Due to fixed speed operation above rated wind speeds, limited output power is another drawback of this system. Lack of power electronic unit results in poor capability of reactive power control and voltage level problems. Need for magnetizing current in order to create magnetic field for stator, makes induction generator reactive power-dependent. Capacitor banks or Static Synchronous Compensators (STATCOM) are commonly used for reactive power compensation with SCIGs. Wind speed fluctuations and tower-shadow effect directly converted in torque dips and fatigue loads on turbine sub-mechanical systems [11], [37].

In variable speed applications of SCIG back-to-back voltage source converters (VSCs) are employed in order to meet the grid codes [38]. Schematic diagram of this type WEC is given in Fig. 2-6. Generator given in Fig. 2-3 was also a constant speed SCIG namely, Danish Concept.

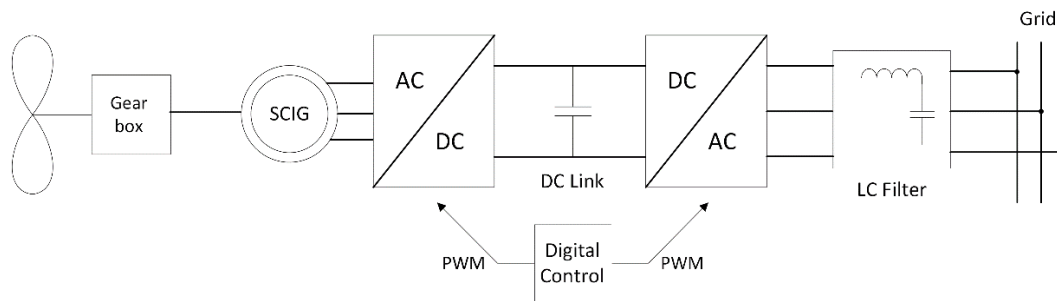


Fig. 2-6. SCIG with back-to-back VSC converter [38]

b) Wound Rotor Induction Generators (WRIG)

Wound rotor induction generators are also known in the market as Optislip concept and have been produced by Vestas since 1990s [36]. These type of generators are used for limited variable speed applications, thus there will be dynamic slip control [38]. This control is applied by connecting electronically controlled resistor blocks to rotor of the generator. Mechanical loads are reduced in this type of configuration

because of controllable speed. Slip denotes the relation between the rotor speed and synchronous speed. It is given by the formula as follows,

$$s = \frac{N_s - N_r}{N_s} \quad (2-9)$$

where, s is the slip, N_s is synchronous speed, N_r is rotor speed. Higher slip magnitudes indicate higher power losses on rotor connected resistors hence lower efficiency. Gearboxes in this system can have multiple stages just as the SCIG case. Also there exist shunt capacitors connected to line for compensation purposes.

Typical WRIG schematic diagram with these capacitors is shown in Fig. 2-7. It can be concluded that main advantage of this concept is limited variable speed operation ability due to resistors connected series with power electronic converter. The main disadvantage of WRIG is lower efficiency due to heat losses on resistors while increasing variable speed range.

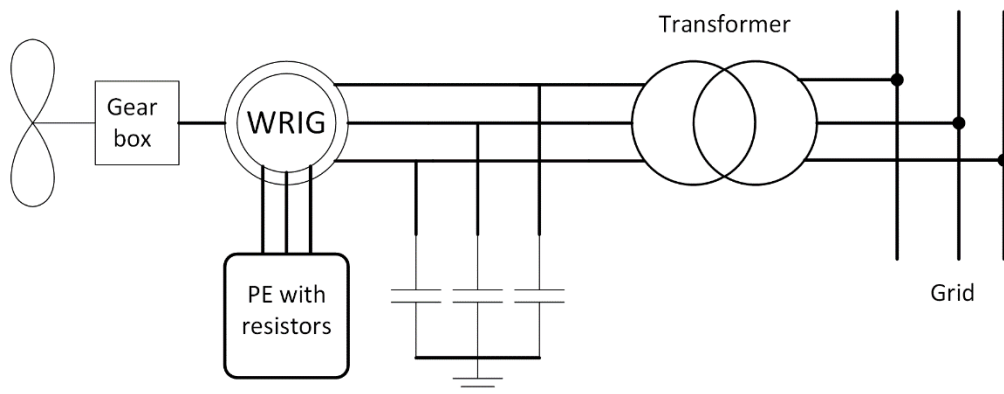


Fig. 2-7. WRIG schematic diagram [38]

c) Doubly-fed Induction Generators (DFIG)

Among wind turbine generator types, doubly-fed induction generator system with 3 stage gearbox (DFIG-3G) is the most utilized formation at present [39]. Although it consists more complicated power electronic control, it can control active and reactive power flow within supply side or rotor side. Stator is coupled to grid via transformer while rotor part is coupled to grid by using power electronic converter stages. This power electronic converter is rated at fraction (usually between 20-30%) of generator power [40], therefore these converters are called as partial scale

converters. The main objective of this power electronic block is to adjust speed range and grid reactive power support. Sometimes second PGSC (parallel grid side converter) is used parallel with dc-link in order to control unbalanced conditions better. Configuration of DFIG is shown in Fig. 2-8. Multistage or single stage gearbox can be used with DFIGs.

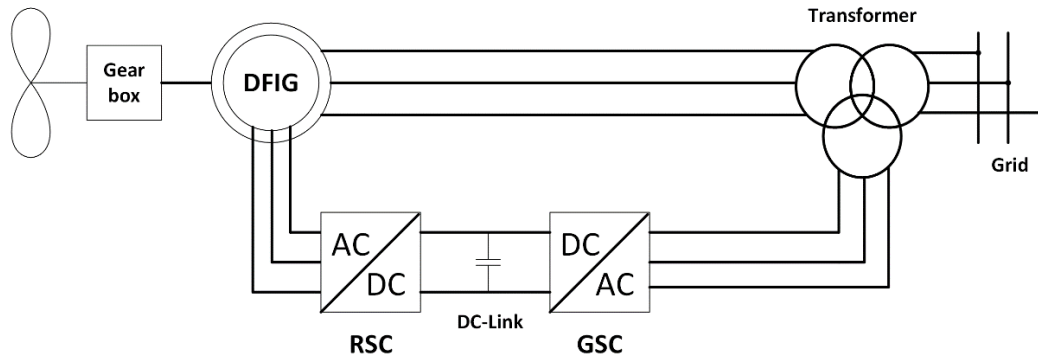


Fig. 2-8. Conventional grid connected DFIG, RSC: Rotor side converter, GSC: Grid side converter [36]

Slip rings and gearboxes are the main disadvantages of this generator. DFIGs are not suitable for direct drive because of efficiency problems. As mentioned before, as machine rotational speed decreases, torque must increase in order to produce same amount of power. Therefore generator size should be increased. However, as the diameter of DFIG increases airgap also increases and magnetizing current increases. Higher magnetizing current means lower efficiency. Besides, generators with larger diameters have large number of poles hence leakage flux problems can occur just as in the SCIG case. Stator part of the DFIG is directly coupled to the grid, thus possible active and reactive power support can be realized via partial scale converter of rotor. Back-to-back converter seen in Fig. 2-8 can be used with crowbar in order to limit the current and provide fault handling capacity [40].

Variable speed operation and efficient converter with active/reactive power control rather than WRIG, low price, easy off-the-shelf availability are the main advantages of DFIG. Dependency on gearbox, complex power electronic and fractional scale adjustable reactive power control, slip rings, high stator peak torques during fault

conditions, weak LVRT capability than synchronous generators with full-scale converters are the main disadvantages of this type of wind turbine generators. Especially with the increasing importance of grid integration, it's expected that DFIGs will become less preferable [30], [41]. In Fig. 2-9, market share of different wind turbine generator technologies for Europe can be seen. As it can be seen on figure, market share of DFIG has a decreasing trend due to the aforementioned disadvantages above.

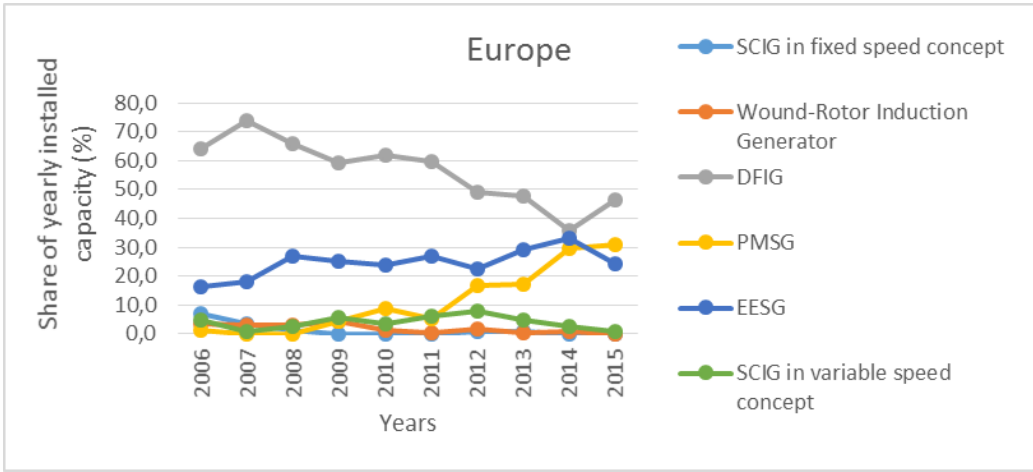


Fig. 2-9. Market share of different wind turbine generators for Europe between 2006 and 2015 [42]

2.3.2. Synchronous Generators

a) Electrically Excited Synchronous Generators (EESG)

Synchronous generators for wind turbines connected to grid via full scale back-to-back power electronic converters. In wound rotor synchronous generators (WRSG), additional partial scale converter is used for rotor DC excitation for required field [40]. Therefore WRSGs are also called as electrically excited synchronous generators (EESG). Rotor of synchronous generator can be excited permanent magnets (PM) also, but this type of generator will be described in the next subsection. One of the most prominent manufacturer of EESG is Enercon. In Fig. 2-10, one of the gearless Enercon wind turbine can be seen. EESG of this commercial wind turbine has 4.2 MW of output power and rotor diameter of 127 meters. One of

the main advantages of this concept is that EESG can be operated with variable speed applications with suitable grid connected power electronic blocks. Additionally, this machine type has cost advantage compared to the direct-drive PM machine due to eliminated PM cost. Power converter losses and high cost of the full scale converter are the main disadvantages of this power take off system. But, it can provide wide control ability of wind turbine generator [43]. It can be either geared or direct-driven. However, direct-driven concept is more popular due to elimination of gearbox losses and increased efficiency. It is manufactured in large size and number of poles, therefore EESG can be heavy and expensive solution. Schematic diagram of EESG is given in Fig. 2-11 with gearbox depicted with dashed lines in order to show it's optional for EESG.



Fig. 2-10. Enercon E-126 EP4, 4.2 MW wind turbine during the installation [44]

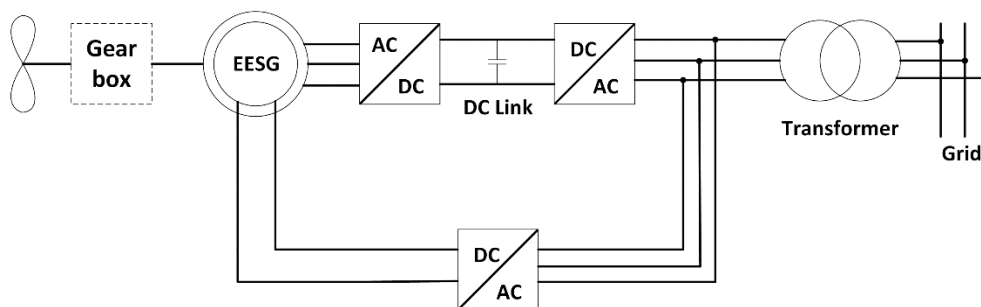


Fig. 2-11. EESG-Electrically Excited Synchronous Generator grid connection [38]

b) Permanent Magnet Synchronous Generators (PMSG)

In this generator type field excitation is realized via permanent magnets rather than the DC excited field winding. Permanent magnet synchronous generators are available in both direct-driven and multi-stage geared versions. In geared version, gearbox compensate the space and volume disadvantage caused by direct drive concept. Direct drive PMSGs are preferred because of their higher energy yield and higher power-to-weight ratios than electrically excited generators. Therefore, overall efficiency is increased in direct drive PMSGs due to its robust structure [45]. Due to its full scale converter, fault-ride-through capabilities and reactive power support ability are important advantages of PMSG. Full-scale converter also allows generator to operate at different frequencies [30]. However, high prices of permanent magnets and fluctuations in these prices, as occurred in 2010 due to China's precautionary actions [30], can be considered as a disadvantage of this concept. Demagnetization risk of PMs is another disadvantage of PMSG. As a good alternative for PM excited synchronous generator, popularity of EESG depends on the PM prices. It can be said that reduction in magnet prices and disadvantages discussed in EESG section cause EESG less preferable against permanent magnet synchronous generators. Recently, capacity of PMSG wind turbines has increased up to nearly 10 MW [8], [46]. Schematic of PMSG with multiple stage gearbox is given in Fig. 2-12 below.

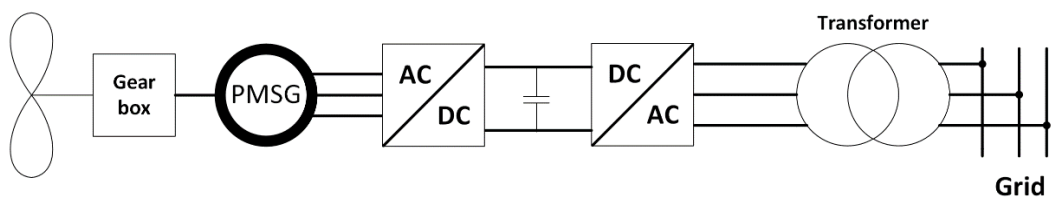


Fig. 2-12. Permanent magnet synchronous generator with gear-box and full scale power electronic converter [36]

As mentioned before in direct drive section, gear box structure causes mechanical loss and requires periodical maintenance. Once gearbox fails, wind turbine can't able to produce energy. Hence this results in downtime losses. Maintenance and

repair losses makes wind turbine inefficient and expensive investment. Therefore, the trend is using direct-driven or single stage gearbox with PMSGs [32], [45]. Single stage gearbox still have mechanical losses rather than gearless system. However, it reduces the rotor diameter and total mass of the direct-driven version.

In direct-drive generators, with the low rotational speeds, diameters are increased in order to obtain higher torque values, hence power levels stay same or goes up. However, increase in diameter and total generator volumes are not feasible for reliability, modularity and transportation. A Germany originated company named Multibrid, designed and commissioned a PMSG with one stage gearbox, Multibrid M5000. Main focus is to reduce the large size of multi MW large direct drive PMSGs. However, this design has the disadvantage of gearbox but cheaper than direct-drive generator. In Fig. 2-13, a picture of 5 MW Multibrid M5000 wind turbine is given.



Fig. 2-13. Multibrid M5000 5MW wind turbine generator(Courtesy of Multibrid and Areva) [47]

It can be concluded that direct-drive technology among PMSGs is gaining attention in last decade due to increased efficiency and reliability issues especially for

offshore wind turbines [48]–[50]. In Fig. 2-14, schematic of direct drive PMSG is given.

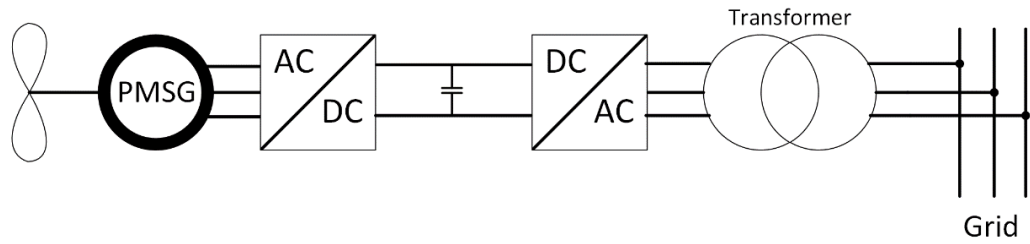


Fig. 2-14. Schematic of direct-driven PMSG [36]

Permanent magnets in PMSGs are arranged in different configuration related to their flux path. These are called as radial flux (RF), axial flux (AF) and transverse flux (TF). In radial flux concept, route of the magnetic flux is perpendicular to the direction of the rotor shaft. In axial flux concept, path of the magnetic flux is parallel to the direction of the rotor shaft. Finally in transverse flux concept, path of the magnetic flux is perpendicular to the rotation direction of the shaft. Additionally, PM machines can be classified according to their mechanical structures such as slot type and stator/rotor position [31]. The sections of a PMSG parts can be classified as active and inactive parts. Active part consists of electromagnetic elements in machine such as PMs, iron core and copper. Inactive part consists of mechanical parts such as steel, shaft and other mechanical frame structures.

In this thesis work, direct drive PMSG is chosen for the design because of its higher energy yield, improved reliability, higher overall efficiency, relatively long maintenance periods and better fault ride-through capability rather than the other electrically excited and multistage geared generator counterparts. Reliability and availability can be increased by developing modular and fault tolerant PMSG. Modularity will be discussed and explained in the following subsections.

2.4. Flux Orientations in PMSG Based Systems

As mentioned before, in PMSG based systems the main electromagnetic flux on rotor side is provided by rare-earth permanent magnets. Therefore, the flux paths for

these permanent magnets and active parts of the generator are important in terms of evaluating magnetic equivalent circuit of the system. In this subsection, different flux orientations and considerations of PM based synchronous generators will be given. To do this, subsection is divided into three parts, namely radial flux, axial flux and transverse flux sections.

2.4.1. Radial Flux (RFPM)

In the radial flux configuration, permanent magnets are arranged so that magnetic flux passes the airgap in radial direction. Radial flux configuration is the most common concept in permanent magnets based large direct drive synchronous generators, due to their high torque density and simple structure [12]. If PMs are mounted on the rotor surface, this type is called as surface mounted permanent magnet machine. Otherwise PMs are placed in slots (buried) of rotor part, aiming to concentrate the flux especially when low remanent flux density magnets are used and still high airgap flux density is needed. RFPM generators can be sometimes constructed with outer rotor inner stator configuration in order to utilize high number of poles with increased cooling capability of outer rotor surface [43]. Iron cored and air-cored are two core types used with inner rotor and outer rotor configuration, respectively. Diameter of RFPM can be adjusted with longer axial length. A typical radial flux surface mounted PM generator arrangement is given in Fig. 2-15. Buried PM version of RFPM is given in Fig. 2-16. As seen on figures, flux crosses the airgap in radial path in both configurations.

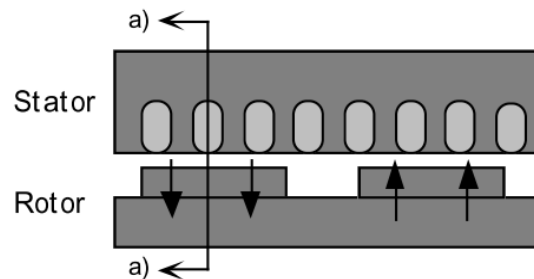


Fig. 2-15. RFPM with surface mounted permanent magnets [10]

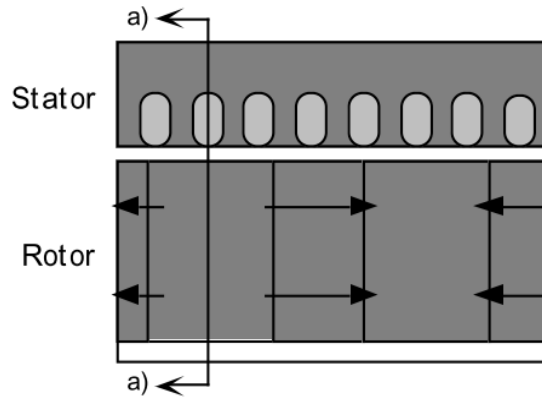


Fig. 2-16. RFPM with buried permanent magnets for flux concentration [10]

RFPM generator can be manufactured in small diameters due to adjustable axial length as aforementioned above. However, long axial length is disadvantage for nacelle and space of wind turbine generator. Additionally, thermal expansion of rotor and stator parts may be problematic in determining air gap clearance [10]. Internal rotor type is the most used RFPM in industry applications. Complete view of conventional inner rotor surface mounted PM type radial flux machine is given in Fig. 2-17.

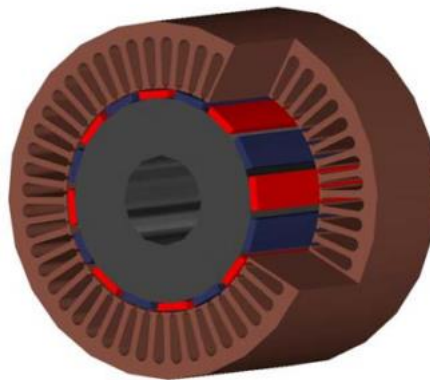


Fig. 2-17. Conventional internal rotor RFPM complete view [51]

2.4.2. Axial Flux (AFPM)

Starting from early 90s, AFPM has been extensively used as an alternative for radial flux counterpart [52]–[55]. In axial flux permanent magnet generators (AFPM),

magnetic flux crosses the air gap in the axial direction. The main advantage of AFPM is that it has relatively short axial length. Therefore, higher torque per volume ratios are achieved [12]. In multistage variations of this machine, outer diameter can be limited without decreasing the torque density significantly. Ratio of inner diameter to outer diameter should be chosen carefully in order to achieve higher output power [56]. This property is preferred when working with limited nacelle space. Adjustable planar air gap is another advantage over the radial flux machines [57]. There are different types of stator/rotor configurations of AFPMs. AFPMs can be classified as slotted and slotless machines, considering the stator winding position. A table showing the various types of AFPM generators according to different criteria is given in Fig. 2-18.

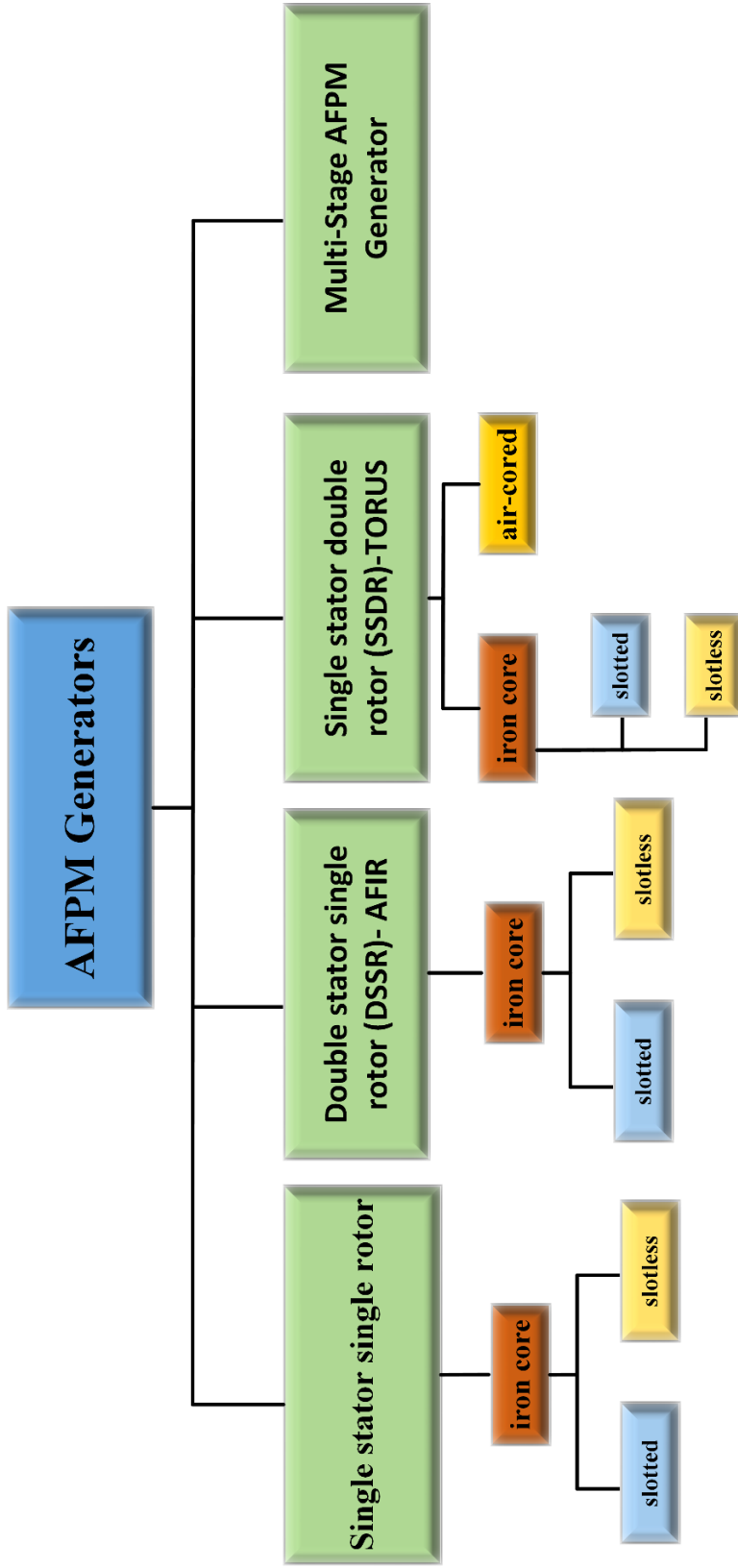


Fig. 2-18. Classification of AFPM generators

The most basic structure of AFPM is the single stator single rotor structure as given in Fig. 2-19. However, strong magnetic attraction force between stator and rotor compelled designers to design the axial structure of the generator with multiple stators/rotors and slotless variations in order to balance the magnetic attraction forces mentioned above [56]. Attraction and thrust forces are equalized thanks to balanced rotor discs and non-slotted stator. Non-slotted special type AFPM generator, which is called TORUS is given in Fig. 2-20. Rotor of this type of generator consist of two discs with PMs mounted on them and stator consisted of iron core and wound coils. In some of the literature, this type of machine is referred as single stator double rotor (SSDR) [55], [56]. Disadvantage of that version is stator iron core losses.

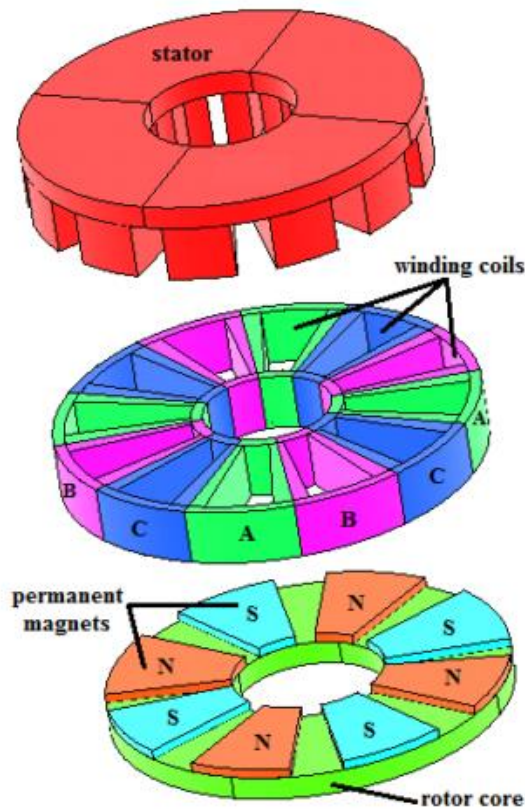


Fig. 2-19. Single sided configuration of AFPM (single stator and single rotor) [55]

Due to its short axial length, AFPMs can be organized with multiple generators on the same shaft axis in order to improve fault tolerance and reliability. AFPMs are

relatively advantageous rather than RFPM when aspect ratio of the generator (diameter/length) is high, ie. large diameter of disc-shaped generators are used [57].

Cogging torque is eliminated due to slotless structure of AFPM generator. In our study slotless air-cored stator is used with axial flux permanent magnet arrangement. Also in the proposed generator modular design is used. Therefore, parallel generators can be added axially.

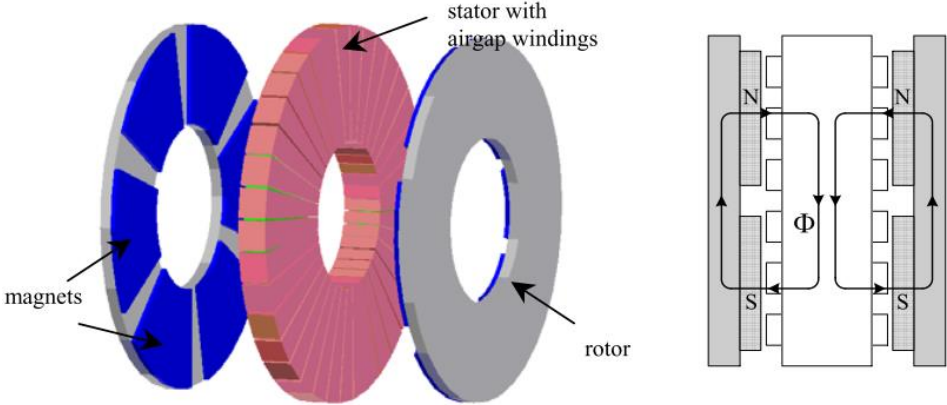


Fig. 2-20. Non slotted TORUS axial flux permanent magnet overview (left) and path of generated flux by permanent magnets (right) [57]

There are two types of slotted TORUS concept: TORUS-NN and TORUS-NS. NN and NS letters used for define magnet placements on rotor discs. Machine overviews and flux paths of both concepts are given in Fig. 2-21 and Fig. 2-22. Main differences between them are flux paths and stator core axial thickness. In our study, main aim is to eliminate iron core because of its core losses and weight. In coreless AFPMs iron losses and torque pulsations are less than other types of AFPMs. General view of coreless TORUS type AFPM generator is given in Fig. 2-23. Detailed schematics of proposed coreless, outer rotor AFPM and related flux organizations will be given in Chapter 3.

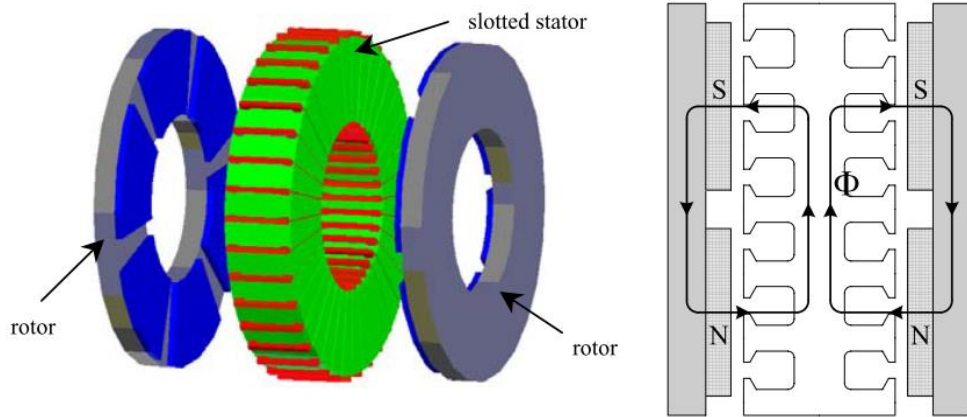


Fig. 2-21. NN-type slotted TORUS axial flux permanent magnet overview (left) and path of generated flux by permanent magnets (right) [57]

As mentioned before in RFPM part, AFPM generator can also have different stator and rotor configurations. In TORUS configuration, we mentioned about two rotor discs which are positioned at the outer region of generator. However, axial flux inner rotor (AFIR) type axial flux generators have two stator blocks at the outer region and one rotor block at the inner region. In some of the literature, this type of machine is referred as double stator single rotor (DSSR) [55], [56]. AFIRs can have slotless and slotted versions, just as in the TORUS configurations.

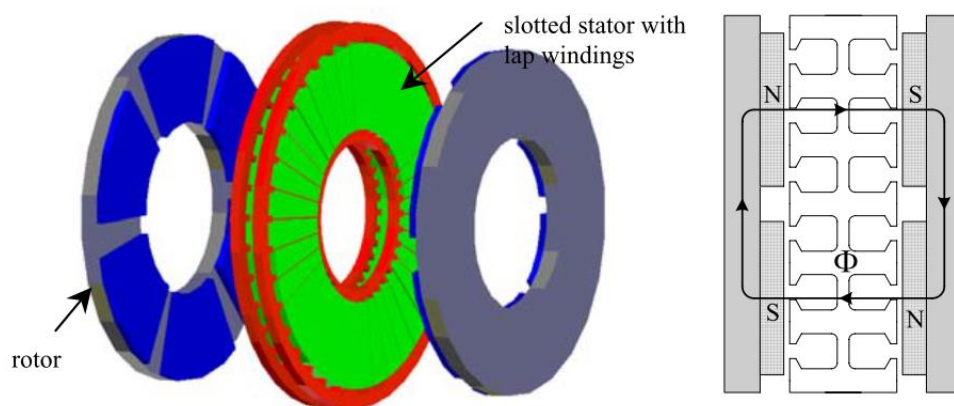


Fig. 2-22. NS-type slotted TORUS axial flux permanent magnet overview (left) and path of generated flux by permanent magnets (right) [57]

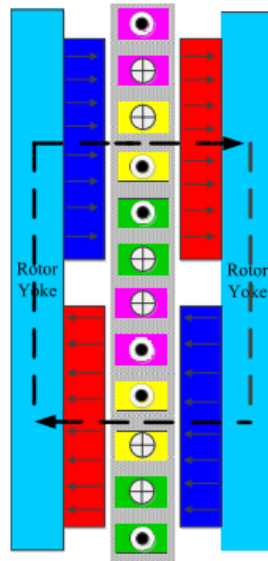


Fig. 2-23. NS-type coreless TORUS axial flux permanent magnet overview [56]

Stator configuration is similar to as it was in TORUS concept. But, in rotor part magnets are not mounted on rotor disc. Instead, permanent magnets formed an interior type structure. Overview and flux paths of slotless AFIR and slotted AFIR are given in Fig.2-24 and Fig. 2-25, respectively.

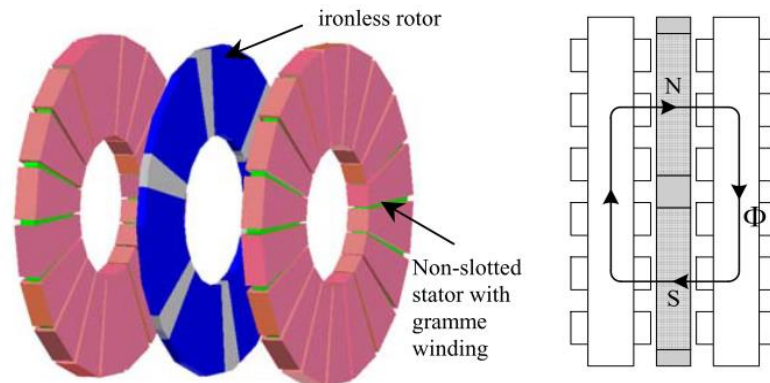


Fig. 2-24. Slotless AFIR overview (left) and path of generated flux by permanent magnets (right) [57]

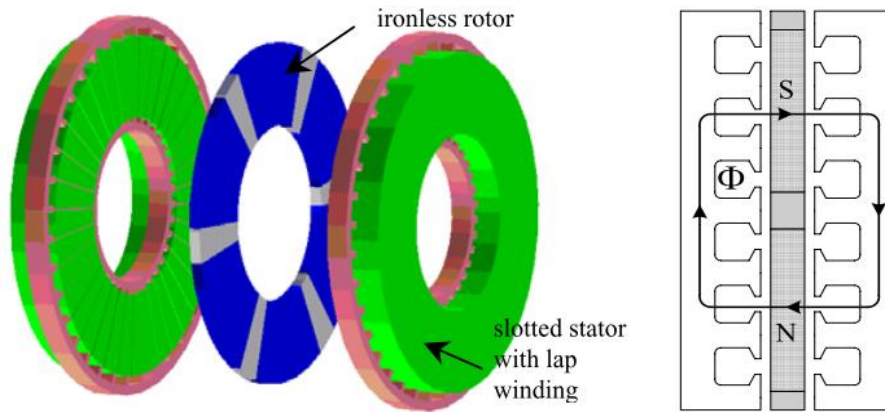


Fig. 2-25. Slotted AFIR overview (left) and path of generated flux by permanent magnets (right) [57]

AFPMs generally used with multi-stage configurations in order to increase torque and output power. In this configuration stages of generators stacked axially on the same shaft with (m) stator discs and (m+1) rotor discs, where “m” represents the number of axial stages. Multi-stage configurations of AFPMs can again be classified as slotless and slotted structures. Properties of these structures are same as that of single stage TORUS and single stage AFIR type slotless and slotted configurations. An example of 2-stage AFPM generator with slotted stator configuration is given in Fig. 2-26. Multi-stage AFPM configurations can be used in ship propulsion and high speed generators. Similar to TORUS, multistage AFPM can be also constructed in ironless fashion. Flux path of the coreless multistage AFPM generator is given in Fig. 2-27. Detailed information about multistage slotted and slotless configurations of multistage AFPMs can be found in literature [10], [31], [51], [56], [57].

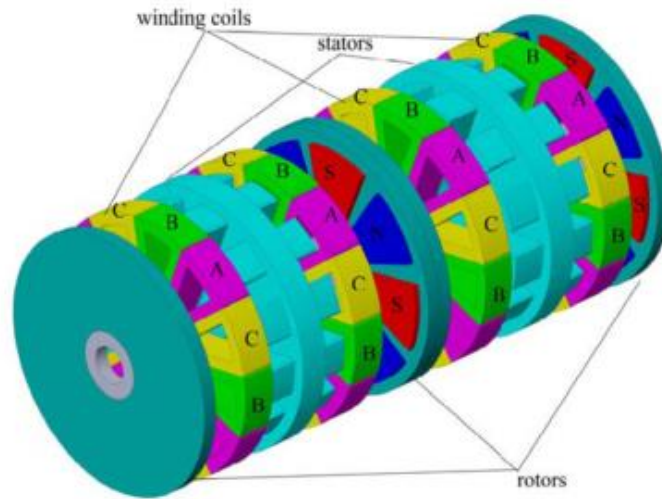


Fig. 2-26. Multistage AFPM generator [56]

Apart from the AFPM topologies discussed above, there are some other novel topologies which uses field control techniques. Another novel topology is double sided hybrid AFPM generators. These variations are not in the scope of this study but they can be found in literature [55], [57]–[60].

To summarize, the advantages of AFPM are: shorter axial length, reduction in cogging torque and torque quality problems, high torque per volume ratio, simplicity in adjusting airgap due to axially stacked stage/stages. Besides, lower torque per weight, large outer diameter as mentioned above, problematic core manufacturing process and higher cost than conventional RFPM are the main disadvantages of AFPM for suitable wind turbine generator [31].

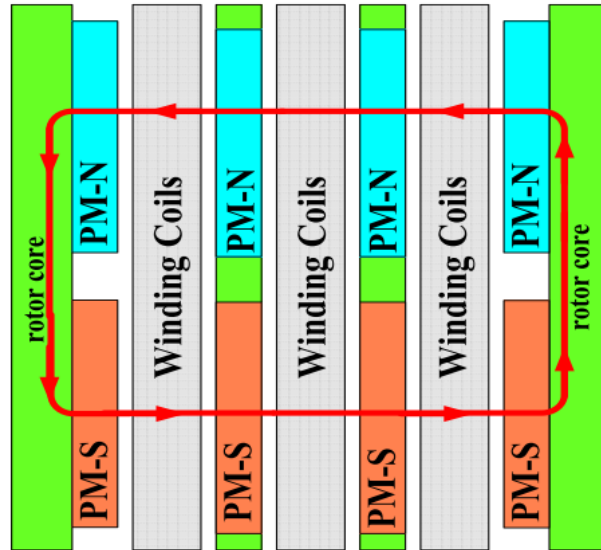


Fig. 2-27. Coreless multistage AFPM generator flux path [55]

In this thesis, coreless version of axial flux permanent magnet machine is studied because of its advantages of axial length and high torque per volume. In this type of machine, generator blocks are added axially to form the whole system. Magnets are placed on the surfaces of C-shaped rotor cores, facing the air-gap stator windings. Stator part consists of air cored concentrated windings. Detailed information about proposed generator and flux patterns will be given in following chapters.

2.4.3. Transverse Flux (TFPM)

In transverse flux machines, the main route of magnetic flux is perpendicular to the rotation of the rotor part. It's suitable for direct drive wind turbine application, considering its high torque density. Although high torque density provides efficient utilization of active materials in TFPM, when air gap increases cost advantage of this concept decreases due to reduced force density. Sample view of TFPM is given in Fig. 2-28. Three dimensional flux path in this type of machine is given in Fig. 2-29. This kind of flux path becomes problematic during analysis and construction.

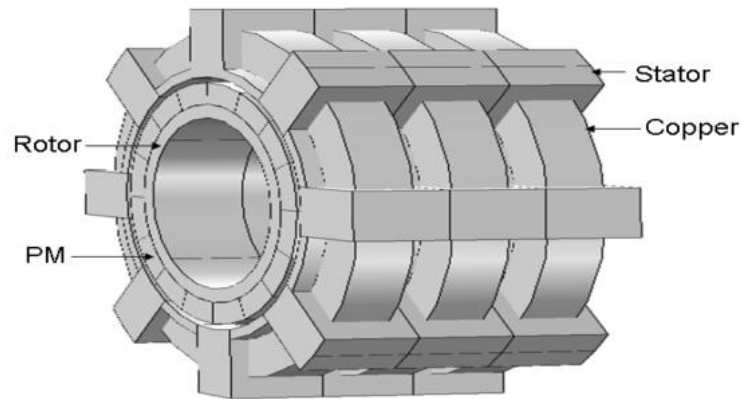


Fig. 2-28. Transverse flux machine view [61]

The main advantages of this concept are higher torque per mass ratio, simple winding construction among other PMSGs and available space for more windings than RFPM and AFPM. However, manufacturing issues due to the complex structure and low power factor eliminates TFPMs from the wind turbine generator configurations [12], [56]. Design improvements must be done in order to use TFPMs in wind turbine generators efficiently.

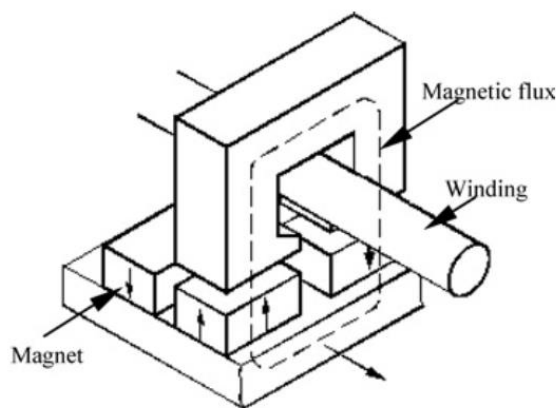


Fig. 2-29. Transverse flux machine three dimensional flux path [43]

2.5. Importance of Modularity in WEC Systems and AFPM

Modular construction of electrical machines aims to get easier assemble and disassemble operations during maintenance and repair conditions. This concept also

allows each module to work individually thus better fault-tolerance. In our study, modularity term has two meanings: axially stacked generators and C-shaped modular cores. First one is related to length advantage of selected generator type. By this modular structure technique, identical machines can be stacked in order to increase torque and power output under limited outer diameter conditions. These stacked generator sets can be grouped in parallel fashion, thus overall reliability of the system increases. Additionally, these axially stacked generators gives fault-tolerance to whole system. For instance, if one or more generators become defective during operation, not all but healthy stacks will continue to operate until the fault is cleared. Therefore, frequency of downtimes will reduce and efficiency of the wind turbine will increase. The latter is related to modular structure of the machine. For example, under fault conditions, defective cores can be changed and/or maintained easily. As mentioned in earlier parts, modularity is related to reliability. In other words, wind turbine generator system which constructed in modular fashion, provides better efficiency. Reliability is related not only with modularity of machine but properties of sub-module parts such as thermal issues about power electronics. Nowadays with the increased importance of grid connection safety and stability, efficiency and reliability become a critical properties of wind turbines. For instance, in offshore wind turbines it's very important to operate the system continuously and to utilize the sub-module parts efficiently. Because, maintenance difficulty related to location is a big disadvantage for offshore wind turbines.

Modularity is not only related to technical problems but also related to economic issues. When large diameters and single bulky structure is considered, modular solutions for permanent magnet direct drive generator topologies become preferable. For example, using multistage generators at relatively low output power ratings is a better solution than using a single huge generator in terms of production, transportation and installation costs. Additionally, crane costs for installation and maintenance will reduce due to low mass of single stack of generator. Another important advantage of modularity is the downtime costs, which is the cost of missing electricity generation income during the downtime of the turbine due to an unexpected failure, can be reduced. As aforementioned in previous parts, a modular

configuration of AFPM generator is proposed for wind turbine generator systems. Modularity and reliability are the key parameters for our proposed generator.

2.6. Conclusion

In this chapter, fundamental equations and issues of wind energy harvesting technology are summarized. After this introduction part, the main challenges and critical issues of wind turbine systems are given. According to literature [1]–[3], generator technology gaining more attention than its past by reaching megawatts of power capability per turbine. Therefore, its design is the main focus point of both this study and current research activities on this area. In the following sections, general overview of the most common wind turbine generator systems are given in detail in order to find suitable generator for MW-level wind turbines. Gearboxes are the main source of losses and faults in wind turbines. Induction generators and especially the DFIG with gearbox is the most common generator type because of its price and experience in both field and production. However, direct drive permanent magnet synchronous generators (PMSG-DD) are found more reliable and feasible solution in terms of efficiency, reliability and fault-ride-through capability. Thus, direct drive PMSG is chosen for the proposed design in this study. Then, flux orientations in PMSGs are discussed in this chapter and axial flux version is preferred among other types of PMSG because of its higher torque over volume ratio and axial length advantages. In this study, axially stacked modular generator with direct drive concept is preferred because of this reliability view. Additionally, using axially stacked generators in AFPM generator configuration can increase the total output power and torque under limited outer diameter conditions. Advantages and disadvantages of every concept and generator types are given in related sub-sections.

After detailed review of generator types and flux orientations in PMSGs, modularity concept is discussed. It's concluded that utilizing the generator in a modular fashion will increase the efficiency and reliability. There are also economic aspects of using modular technologies in wind turbine design. Installation costs, crane costs for maintenance and installation, transportation costs and downtime costs can be reduced with modular design concept. Detailed design calculations of proposed direct-drive modular AFPM synchronous generator will be given in the next chapter.

CHAPTER 3

DESIGN OF THE PROPOSED AXIAL FLUX GENERATOR

In the previous chapters, background information about wind energy conversion systems and detailed overview of the most used generator types are presented. Then, challenges of modern wind turbine systems and fundamental equations are discussed. Direct drive axial flux permanent magnet generator is chosen for the design in this thesis study because of its lower mechanical losses due to eliminated gearbox, high torque per volume and axial length advantages [12], [45]. In this chapter, electrical and mechanical design parameters of axial flux permanent magnet generators will be described. In order to do this, analytical design equations of the proposed generator are presented in the following subsections. Finally, a result comparison of electromagnetic FEA and analytical calculation for a sample 50 kW generator will be presented to confirm the accuracy of the FEA simulations. Analytic design equations described in this chapter are coded in MATLAB and then used in genetic algorithm optimization, which will be discussed in the next chapter.

3.1. Mechanical and Electrical Parameters

In this section, main electrical and mechanical parameter calculations of the proposed AFPM generator will be presented. In order to achieve an integrated understanding, dimensions and related drawings of the generator will be shown first. Then, magnetic circuit parameters including the airgap flux density and induced emf of the design will be explained. Finally, structural and thermal design notes will be presented. In addition, calculation of the losses will be stated at the end of this section.

3.1.1. Dimensions of the Proposed AFPM Generator

In axial flux permanent magnet synchronous generator, inner air-cored stator and outer rotor surface mounted permanent magnets will be used. General overview of the proposed generator is given in Fig. 3-1. In this figure, six axially stacked generator blocks are presented. However, this figure includes only 4 poles section of the proposed system, for the sake of simplicity.

There is a $(4/3)$ ratio between the coil pitch and the pole pitch in order to achieve maximum flux linkage. Since flux linked by the coil is related to induced voltage [31], [62], choosing optimum value of the pitch ratio has a high importance in electrical machine design. Induced voltage variation of a coil according to different coil pitch/pole pitch ratios, is shown in Fig.3-2. As it can be seen from this figure, $4/3$ ratio has the highest induced voltage rating. This type of configuration is also used for modularity in our design.

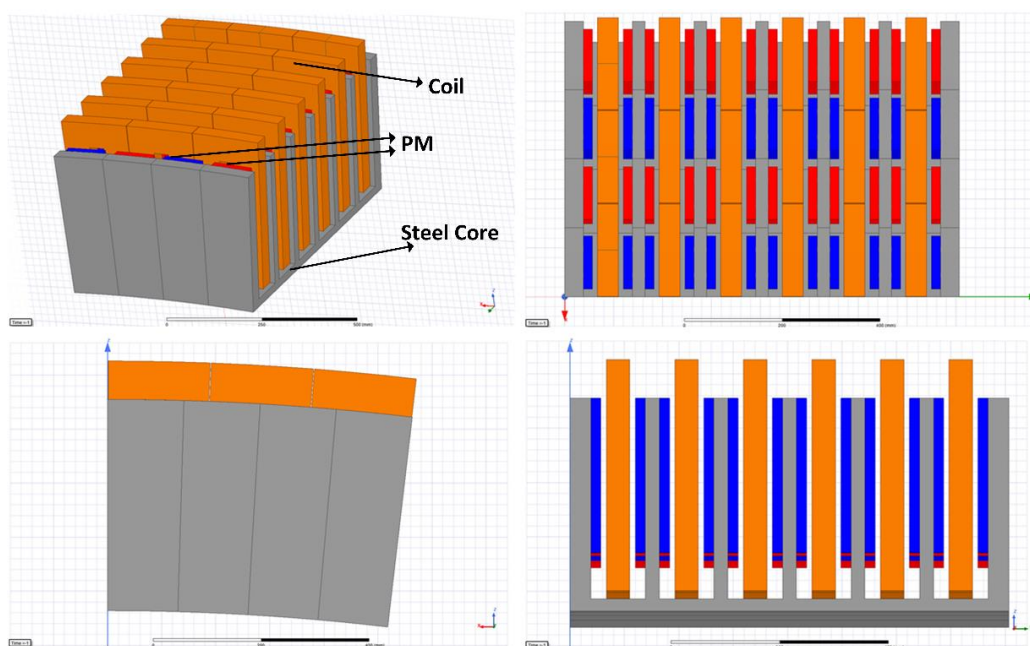


Fig. 3-1. 4-pole section of the proposed axial flux PM generator

Main dimensions of the proposed AFPM generator are presented with their descriptions in Table 3-1, Table 3-2 and Table 3-3. These dimensions are shown on

the machine drawing from different view angles in Fig.3-3, Fig.3-4 and Fig.3-5, respectively.

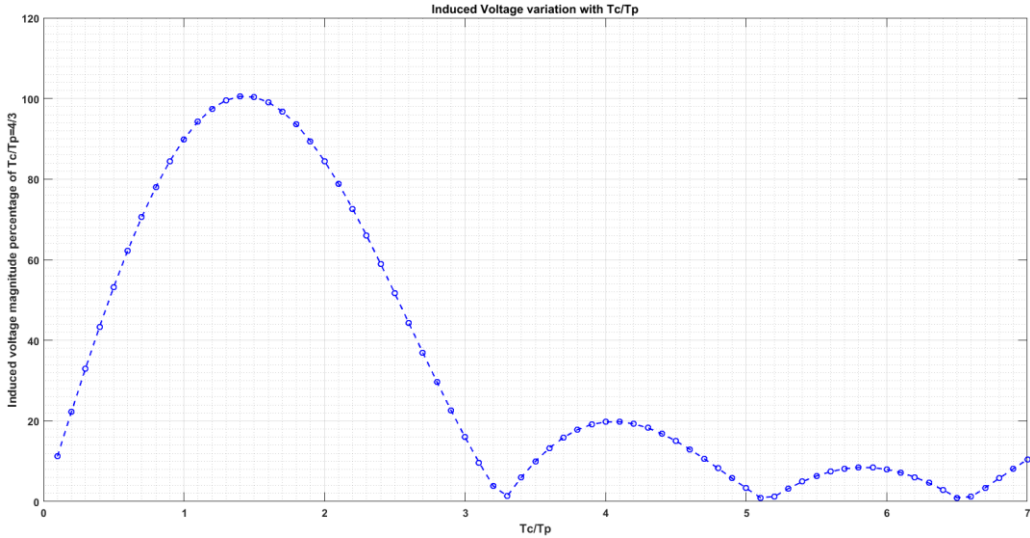


Fig. 3-2. Induced voltage variation with respect to different τ_c/τ_p ratios

In Fig.3-3, dimensions for the side view of the proposed AFPM are shown. These parameter definitions are presented in Table 3-1.

Table 3-1. Dimensions of the proposed AFPM generator at side view

Dimension	Description
g	Airgap clearance
c_{w2sw}	Coil to steel-web clearance
l_{cl}	Magnet to steel-web clearance
h_w	Height of the winding
h_m	Height of the magnet
l_{mm}	Magnet-to-magnet distance
l_{ss}	Steel-to-steel distance
l_c	Steel web thickness
l_m	Length of the magnet
t_w	Thickness of winding
τ_c	Coil pitch
α_{pitch}	Coil thickness/coil pitch ratio

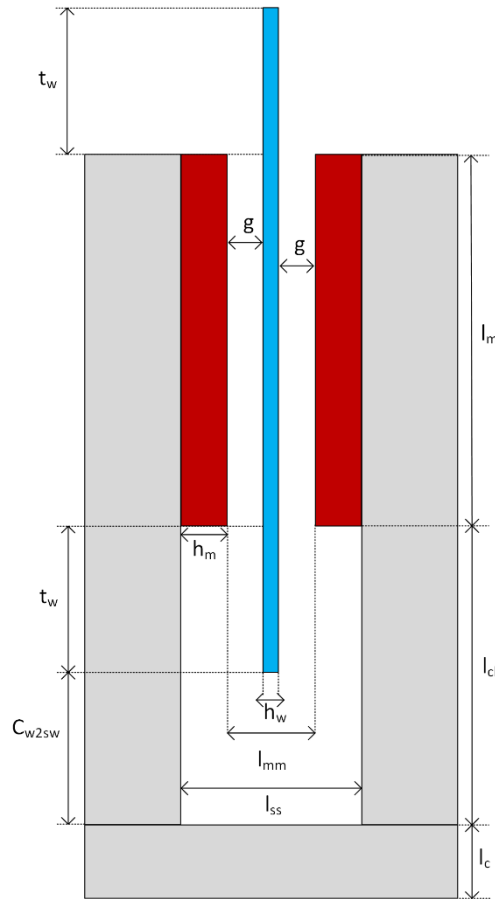


Fig 3-3. C-shaped core from side view with defined dimensions in Table 3-1

Width(thickness) of the winding value t_w is calculated by the help of the coil pitch ratio α_{pitch} as follows,

$$t_w = \alpha_{pitch} \tau_c \quad (3-1)$$

c_{w2sw} is the distance between coil and steel web. This value is used in the optimization algorithm as a constant. However, selection of proper distance is important for design considerations. Value of the coil thickness/pitch ratio α_{pitch} is determined by using optimization. In Fig.3-4, dimensions for the counter view of the one pole of the proposed generator are shown. These parameter definitions are presented in Table 3-2.

Table 3-2. Dimensions of the proposed AFPM generator pole at counter view

Dimension	Description
τ_p	Pole pitch
r_o	Outer radius
r_i	Inner radius
r_{mean}	Mean radius
r_{web}	Web radius
w_m	Width of the magnet
N_p	Number of poles
τ_{web}	Web pole pitch

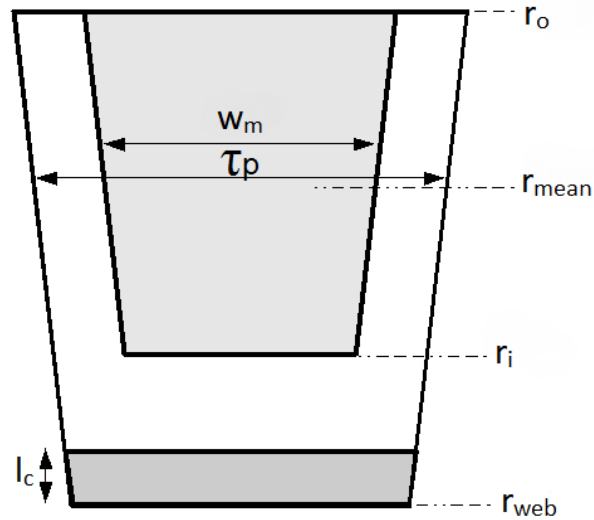


Fig. 3-4. Counter view of one pole of the generator core limb [63]

Pole pitch τ_p distance can be calculated as follows [64],

$$\tau_p = \frac{2\pi r_{mean}}{N_p} \quad (3-2)$$

Mean radius r_{mean} and magnet length l_m are determined by the optimization in our study. Outer radius r_o and inner radius r_i lengths are calculated by using magnet length and generator mean radius values as follows,

$$r_o = r_{mean} + \frac{l_m}{2} \quad (3-3)$$

$$r_i = r_{mean} - \frac{l_m}{2} \quad (3-4)$$

In this study, groove distance is taken as zero and it is assumed that magnets are smoothly surface mounted on the C-cores without any gap. Circumferential distance between the two successive C-cores, namely spacer gap is also assumed as zero. Web pole pitch τ_{web} is calculated as follows,

$$\tau_{web} = 2\pi \frac{r_{web}}{N_p} \quad (3-5)$$

Magnet width distance (magnet pitch) w_m can be calculated by using magnet pitch-to-pole pitch ratio α_i as follows,

$$w_m = \alpha_i \tau_p \quad (3-6)$$

Magnet pitch-to-pole pitch ratio α_i is also referred as pole shoe arc-to-pole pitch ratio in [65] and can be described for our design as follows,

$$\alpha_i = \frac{w_m}{\tau_p} \quad (3-7)$$

Lower values of this variable leads to lower utilization of permanent magnets, hence higher values are preferred. However, much higher values of α_i result in increased leakage flux between permanent magnets thus decreasing the airgap flux density and machine electromagnetic performance [64], [66]. Therefore, value of this ratio is determined by using optimization. Leakage flux phenomenon is depicted in Fig. 3-5 in order to show the effect of higher α_i . Stator outer diameter is important during the design because it should be limited for specific application and determines the main properties of a generator together with the parameter of axial length. Stator outer diameter is calculated as follows,

$$d_{out} = 2(r_o + 2t_w) \quad (3-8)$$

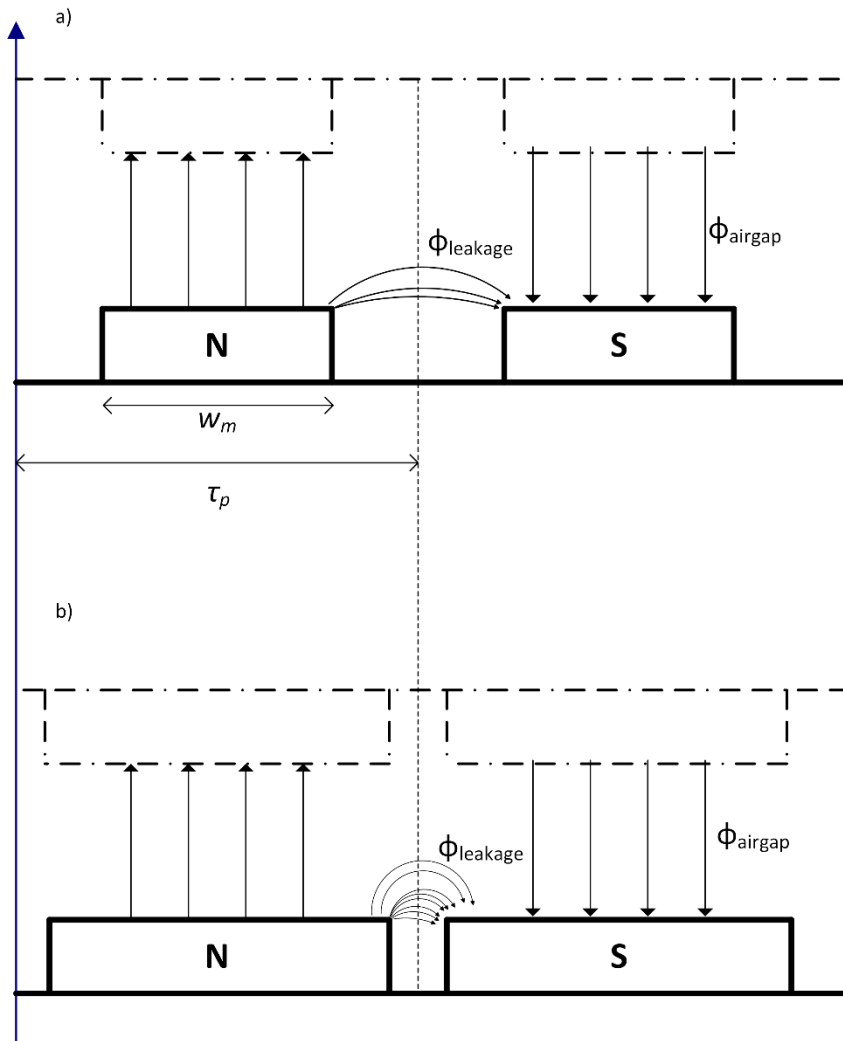


Fig. 3-5. Effect of higher α_i in terms of leakage flux from the top view of the generator.

a) shows lower ratios of α_i with lower leakage flux. b) Ratio of α_i is increased thus leakage flux increases and lowering the effective airgap flux density

In Fig.3-6, dimensions for the C-core coil of the proposed generator are shown at counter view. These parameter definitions are presented in Table 3-3.

Table 3-3. Dimension of the proposed AFPM generator coil at counter view

Dimension	Description
θ_i	Inner length ratio
θ_o	Outer length ratio
θ_{dif}	Length ratio difference which corresponds to thickness of the winding

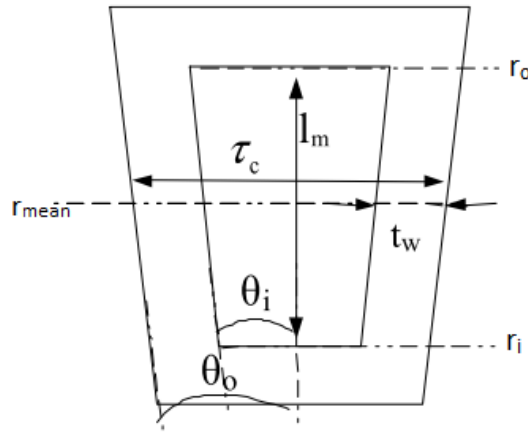


Fig. 3-6. C-core coil with inner and outer length ratios at counter view [63]

Length ratios θ_o and θ_i shown in the Fig. 3-6 above, are calculated as follows,

$$\theta_o = \frac{\tau_c}{2r_{mean}} \quad (3-9)$$

$$\theta_{dif} = \frac{t_w}{r_{mean}} \quad (3-10)$$

$$\theta_i = \theta_o - \theta_{dif} \quad (3-11)$$

where θ_{dif} is the difference between two ratios. These length ratios are utilized to define the coil segments in radian and used in the flux linkage calculation. These calculations will be presented in the following subsections.

3.1.2. Electromagnetic Design

In this subsection, electromagnetic design stages of the proposed AFPM generator will be described. In order to do this, first magnetic reluctance network of the machine will be presented. Then induced emf and related flux density calculations will be summarized.

- **Magnetic Circuit**

In order to find essential fluxes and flux densities of the proposed generator, flux paths and reluctance network should be defined first [67]. It's assumed that leakage fluxes are exist in the generator in order to calculate the parameters and analyze the generator more accurately. Therefore, flux paths and equations will be defined accordingly. Reluctances and flux paths are shown in side and top view of the c-cores in Fig. 3-7 and Fig. 3-9, respectively.

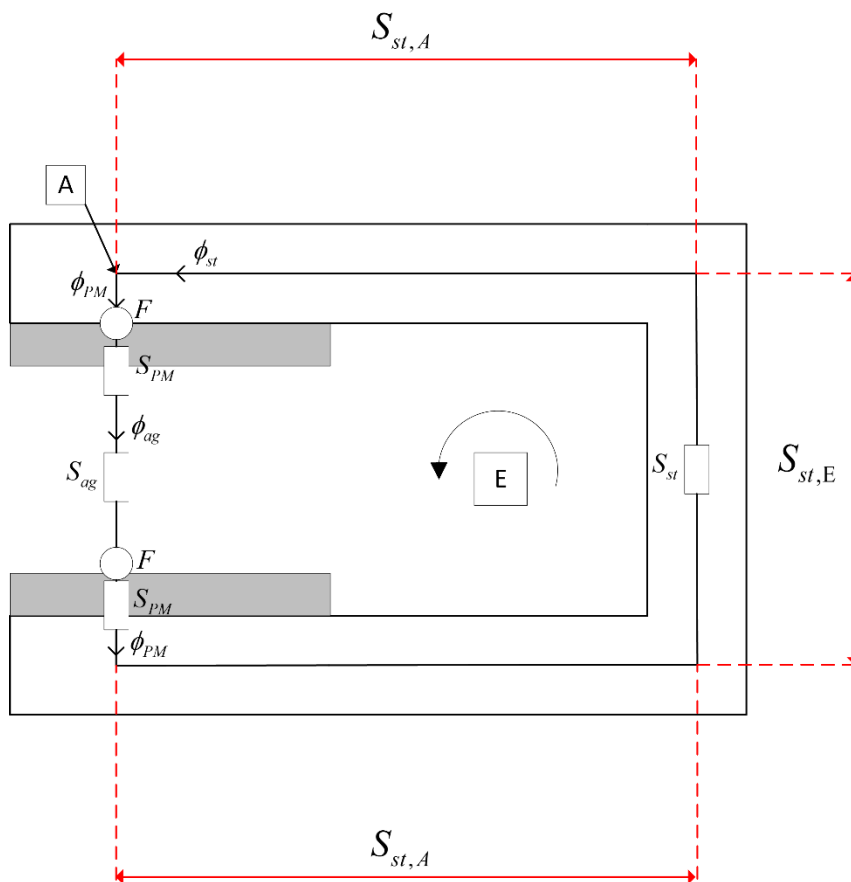


Fig. 3-7. Side view of the C-core for reluctances and flux paths [68]

Airgap reluctance S_{ag} of the machine is calculated as follows[67],

$$S_{ag} = \frac{(h_w + 2g)}{(\mu_0 l_m w_m)} \quad (3-12)$$

where μ_0 is the permeability of air. Steel reluctance S_{st} can be evaluated as two parts, namely Part A and Part E, depicted in Fig. 3-7. These specific reluctances and resulting total steel reluctance are calculated as follows [67],

$$S_{st,A} = \frac{0.5l_m + l_{cl} + 0.5l_c}{\mu_0 \mu_{st} 0.5 t_o (\tau_p + \tau_{web})} \quad (3-13)$$

$$S_{st,E} = \frac{2(h_m + g) + h_w + t_o}{\mu_0 \mu_{st} l_c \tau_{web}} \quad (3-14)$$

$$S_{st} = 2S_{st,A} + S_{st,E} \quad (3-15)$$

where t_o and μ_{st} are thickness of outer limb and relative permeability of steel, respectively. Outer (t_o) and inner (t_i) limb thickness values are determined according to optimization process, which will be described in the next chapter. Reluctance of spacer is calculated as follows,

$$S_{sp} = \frac{\tau_p}{\mu_0 \mu_{st} t_o l_m} \quad (3-16)$$

Defined spacer reluctance above corresponds to inter-module steel part of core [67]. Reluctance value of the inter-module gap is omitted because gap distance is assumed as zero, as mentioned before. PM reluctance consists of two parts: magnet's self reluctance and reluctance of the steel region. These two parts are shown in Fig. 3-8.

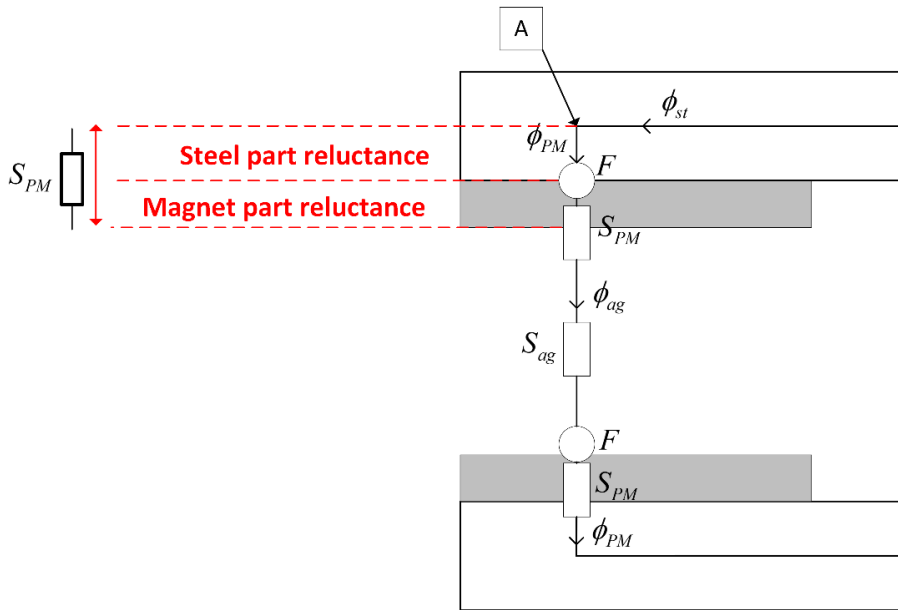


Fig. 3-8. Permanent magnet reluctance components

PM reluctance S_{PM} is calculated as follows [67],

$$S_{PM} = \frac{h_m}{\mu_0 \mu_r w_m l_m} + \frac{0.5 t_o}{\mu_0 \mu_{st} w_m l_m} \quad (3-17)$$

where μ_r is the permeability value of the PM material. Leakage fluxes in this study are assumed for magnet-magnet leakage direction. Top view of the C-cores showing the fluxes and flux paths including the mentioned leakage reluctances, is given in Fig. 3-9.

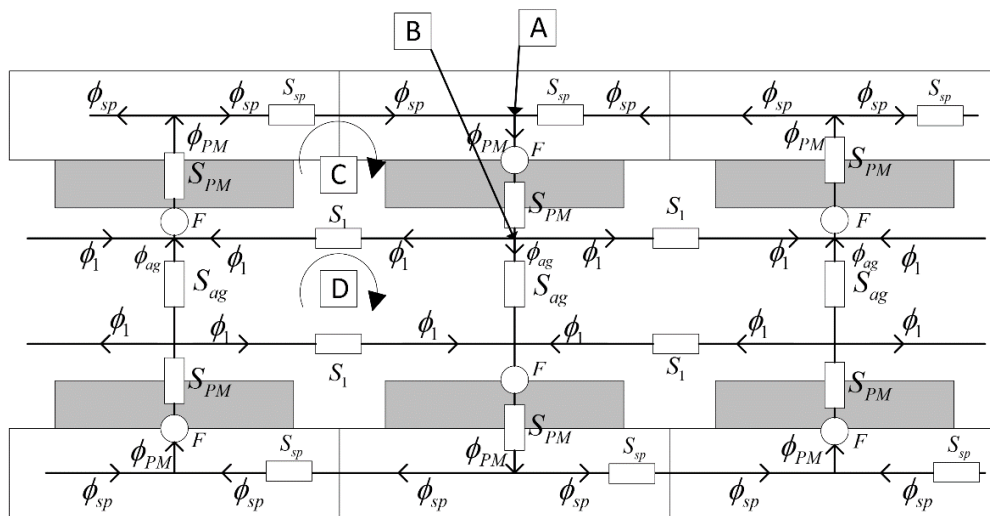


Fig. 3-9. Top view of the C-cores for reluctances and flux paths included leakage effect

[67]

As it can be seen on Fig. 3-8 and Fig. 3-9, permanent magnets are the main MMF source for the magnetic equivalent circuit. This MMF value provided by the permanent magnets, can be calculated as follows [67],

$$F = \frac{B_r h_m}{\mu_0 \mu_r} \quad (3-18)$$

where B_r is the remanent flux density value of the PM. Remanent flux density value is taken as 1.4 T for the selected grade N50 rare-earth magnet [69]. Leakage path reluctance S_l has two components. These components are shown in Fig. 3-10. According to this figure, leakage reluctance component $S_{1,2}$ corresponds to gap regions facing the magnets in axial direction while reluctance component $S_{1,1}$ corresponds to gap region between magnets in circumferential direction. It is assumed that flux generated by the magnets entering and leaving the magnets in axial direction. Therefore, leakage flux calculations on the side faces of magnets are unnecessary.

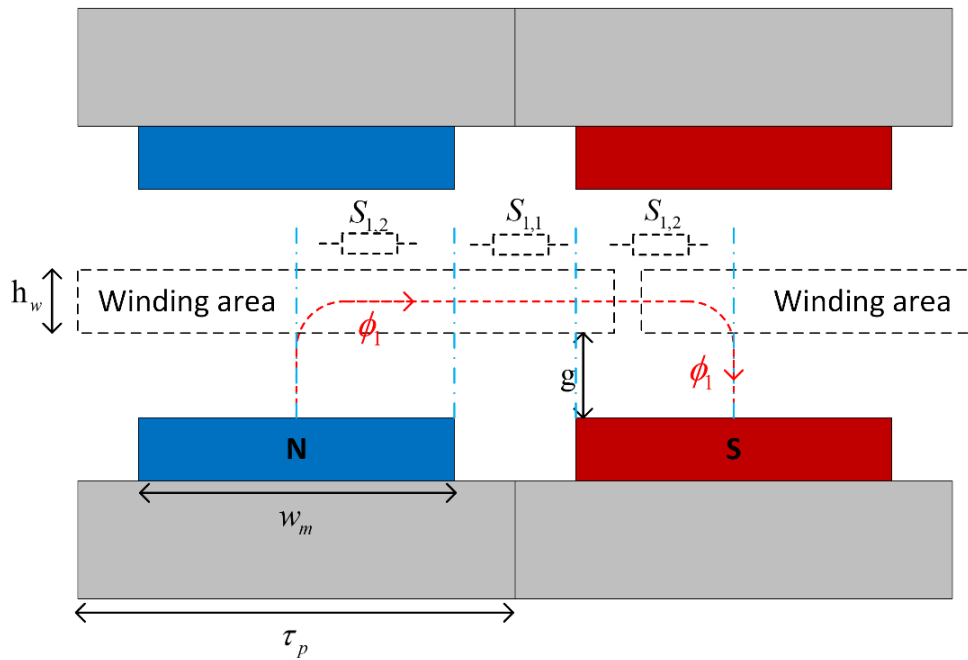


Fig. 3-10. Leakage reluctance network

These reluctance components and resulting reluctance S_l are calculated as follows,

$$S_l = S_{1,1} + S_{1,2} \quad (3-19)$$

$$S_{1,1} = \frac{\tau_p - w_m}{\mu_0 l_m (0.5h_w + g)} \quad (3-20)$$

$$S_{1,2} = \frac{w_m}{\mu_0 l_m (0.5h_w + g)} \quad (3-21)$$

In order to define fluxes and flux densities, magnetic circuit should be analysed in terms of reluctance network. Node equations at point A in Fig. 3-7 and Fig. 3-9 can be written as follows,

$$\phi_{PM} = 2\phi_{sp} + \phi_{st} \quad (3-22)$$

Equation at node B in Fig. 3-9,

$$\phi_{ag} = \phi_{PM} - 2\phi_1 \quad (3-23)$$

For the loop C in Fig. 3-9,

$$2F = 2\phi_{PM} S_{PM} + \phi_{sp} S_{sp} + \phi_1 S_1 \quad (3-24)$$

For the loop D in Fig. 3-9,

$$\begin{aligned} 0 &= 2\phi_{ag} S_{ag} - 2\phi_1 S_1 \\ \phi_1 &= \frac{\phi_{ag} S_{ag}}{S_1} \end{aligned} \quad (3-25)$$

For the loop E in Fig. 3-7,

$$2F = \phi_{ag} S_{ag} + 2\phi_{PM} S_{PM} + \phi_{st} S_{st} \quad (3-26)$$

from Eq. (3-23) and Eq. (3-25) ,

$$\phi_{ag} = \phi_{PM} - 2 \frac{\phi_{ag} S_{ag}}{S_1} \quad (3-27)$$

$$\phi_{PM} = \phi_{ag} \left(1 + 2 \frac{S_{ag}}{S_1} \right) \quad (3-28)$$

From Eq. (3-22) ,

$$\phi_{st} = \phi_{PM} - 2\phi_{sp} \quad (3-29)$$

$$\phi_{st} = \phi_{ag} \left(1 + 2 \frac{S_{ag}}{S_1} \right) - 2\phi_{sp} \quad (3-30)$$

From Eq. (3-24) ,

$$2F = 2\phi_{ag} \left(1 + 2 \frac{S_{ag}}{S_1} \right) S_{PM} + \phi_{sp} S_{sp} + \phi_{ag} S_{ag} \quad (3-31)$$

From Eq. (3-26) ,

$$2F = \phi_{ag} S_{ag} + 2\phi_{ag} \left(1 + 2\frac{S_{ag}}{S_1}\right) S_{PM} + \left(\phi_{ag} \left(1 + 2\frac{S_{ag}}{S_1}\right) - 2\phi_{sp}\right) S_{st} \quad (3-32)$$

where, ϕ_{sp} , ϕ_{st} , ϕ_{PM} and ϕ_{ag} are spacer flux, steel flux, permanent magnet flux and airgap flux, respectively. Left and right hand sides of the Eq. (3-31) and Eq. (3-32) can be defined as MMF matrix, reluctance matrix and flux matrix. Reluctance matrix according to combined form of loop equations given in Eq. (3-31) and Eq. (3-32) can be expressed as follows,

$$R = \begin{bmatrix} 2\left(1 + 2\frac{S_{ag}}{S_1}\right) S_{PM} + S_{ag} & S_{sp} \\ 2\left(1 + 2\frac{S_{ag}}{S_1}\right) S_{PM} + S_{ag} + \left(1 + 2\frac{S_{ag}}{S_1}\right) S_{st} & -2S_{st} \end{bmatrix}_{2 \times 2} \quad (3-33)$$

Flux and MMF matrixes are defined according to combined form of reluctance matrix given in Eq. (3-33) as follows,

$$\begin{bmatrix} 2F \\ 2F \end{bmatrix} = R \begin{bmatrix} \phi_{ag} \\ \phi_{sp} \end{bmatrix} \quad (3-34)$$

To obtain the required flux values, inverse of the reluctance matrix should be multiplied with the MMF matrix. Therefore, resulting flux values are calculated as follows,

$$\begin{bmatrix} \phi_{ag} \\ \phi_{sp} \end{bmatrix} = R^{-1} \begin{bmatrix} 2F \\ 2F \end{bmatrix} \quad (3-35)$$

Steel flux ϕ_{st} is calculated according to Eq. (3-30). Airgap and spacer flux densities are calculated based on above flux equations as follows [67],

For air-gap flux density,

$$B_{ag} = \frac{\phi_{ag}}{l_m w_m} \quad (3-36)$$

For spacer flux density,

$$B_{sp} = \frac{\phi_{sp}}{l_m t_o} \quad (3-37)$$

For steel flux density,

$$B_{st} = \frac{\phi_{st}}{l_c \tau_{web}} \quad (3-38)$$

- **Electrical Parameters**

Since the proposed machine is a synchronous generator, electrical frequency of the machine is defined as follows [70],

$$f = \frac{n N_p}{120} \quad (3-39)$$

where n is the rotational speed in rpm. Mechanical speed w_{mech} (rad/s) is calculated as follows,

$$w_{mech} = \frac{2\pi n}{60} \quad (3-40)$$

Airgap linear speed v (m/s) can be calculated as follows,

$$v = r_{mean} w_{mech} \quad (3-41)$$

In analytical design calculations, it is assumed that flux density in the airgap has a square waveform nature. Therefore, calculated analytical airgap flux density B_{ag} in previous sections, is the flat-top value of mentioned square wave. However, in reality this flux density waveforms are sinusoidal rather than square wave due to magnet shapes and leakage fluxes. Thus, peak value of the fundamental frequency component of the square waveform is utilized in calculations of flux linkage and induced emf [62]. In the following sections, peak values of the fundamental component of airgap flux density in analytical calculation and finite element analysis results will be compared. In Fig. 3-11, mentioned square waveform of analytical calculation and sinusoidal fundamental component of airgap flux density are shown. As it can be seen from this figure, width of the square wave is related to magnet pitch-to-pole pitch ratio α_i .

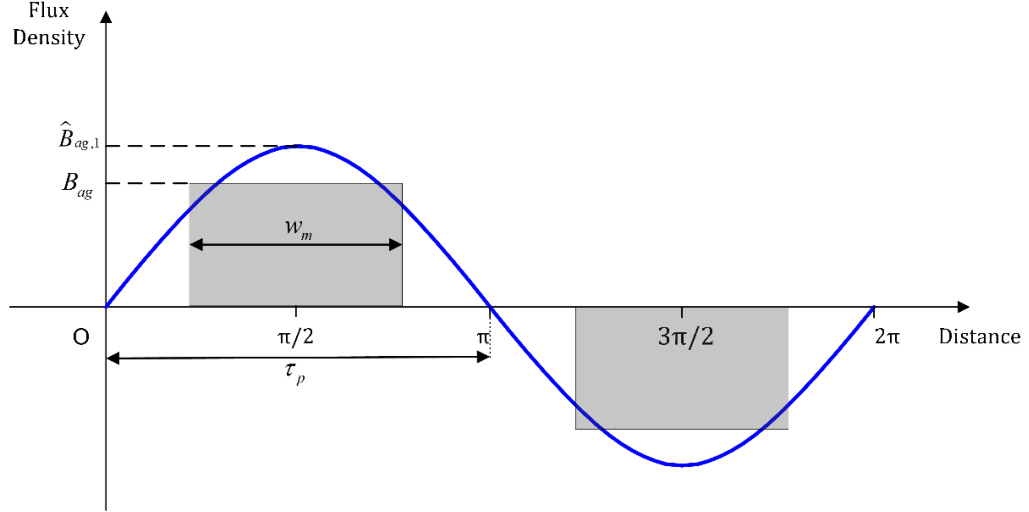


Fig. 3-11. Calculated airgap flux density square waveform (grey) and its sinusoidal fundamental frequency component (blue)

Peak value of the fundamental harmonic value of the air-gap flux density B_{ag} is given as follows [62],

$$B_{ag,1} = \frac{4}{\pi} B_{ag} \sin(\alpha_i \frac{\pi}{2}) \quad (3-42)$$

Peak flux linkage is calculated for the proposed generator as follows [63], [71],

$$\lambda_{pk} = \frac{k_{leak} \hat{B}_{ag,1} (r_o^2 - r_i^2) (\cos(N_p \frac{\theta_i}{2}) - \cos(N_p \frac{\theta_o}{2}))}{(\theta_o - \theta_i) (\frac{N_p}{2})^2} \quad (3-43)$$

Leakage coefficient k_{leak} is selected as constant of 0.95. This value is determined according to comparison of induced emf results between analytical calculations and FEA. Induced emf e in one turn of coil is calculated according to Faraday's Law by using linked peak flux as follows [63], [71],

$$e = \frac{v \lambda_{pk} \pi}{\tau_p} \quad (3-44)$$

Approximate per-phase equivalent circuit and phasor representation of synchronous machine are given Fig. 3-12 and Fig. 3-13, respectively. Output rms phase voltage (terminal voltage) of a typical synchronous machine is calculated as follows [70],

$$\vec{V}_{ph} = \vec{E}_{ph} - j\vec{I}_{ph}X_s \quad (3-45)$$

where, E_{ph} is the induced emf rms value, X_s is the per phase synchronous reactance under steady state temperature and I_{ph} is the rms phase current.

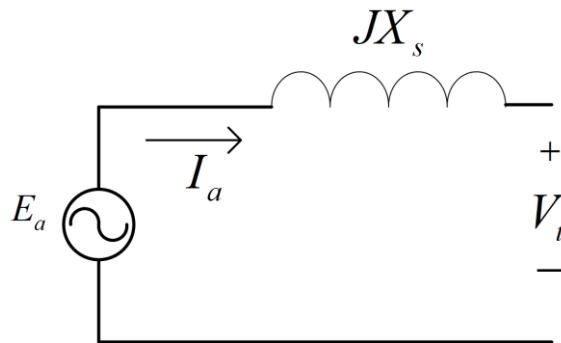


Fig. 3-12. Equivalent circuit of the synchronous machine where E_a is the induced emf, I_a is the phase current, X_s is the synchronous reactance and V_t is the phase terminal voltage [70]

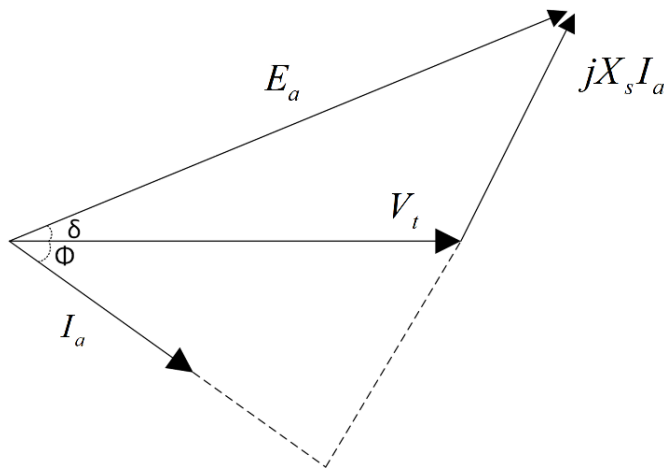


Fig. 3-13. Phasor diagram of synchronous machine with load angle (δ) and power factor angle (Φ)

E_{ph} can be calculated as follows,

$$E_{ph} = \frac{eN_t N_s}{\sqrt{2}} \quad (3-46)$$

where N_s is the number of coils in series. Phase voltage rms value according phasor diagram given in Fig. 3-13, is calculated as follows,

$$V_{ph} = E_{ph} \cos(\delta) - I_{ph} (R_{phase_th} \cos(\varphi) + X_{ph} \sin(\varphi)) \quad (3-47)$$

where R_{phase_th} and X_{ph} are phase resistance (which is relatively small than reactance) and phase reactance, respectively. Power factor is assumed as unity in our design. Therefore, power factor angle φ is equal to zero. Because, a vector controlled power electronic stage is considered for the converter part. However, power electronic converter design is out of the scope of this thesis. Load angle δ is calculated at every rotation speed in the design optimization code according to trigonometric equation given below,

$$\delta = \sin^{-1} \left(\frac{I_{ph} (R_{phase_th} \sin(\varphi) + X_{ph} \cos(\varphi))}{E_{ph}} \right) \quad (3-48)$$

Effective window area of the conductors A_{eff} is related with the conductor dimensions and fill factor of the design. This area value is utilized in current and resistance calculations. In Fig. 3-14, schematic representation the of the conductors in cross-sectional window of the winding is given. Effective window area can be expressed as follows,

$$A_{eff} = h_w t_w k_{fill} \quad (3-49)$$

where k_{fill} is the fill factor for the winding coils. Fill factor can be taken as constant between 0.6 and 0.7 during optimization process due to concentrated air cored windings in our design.

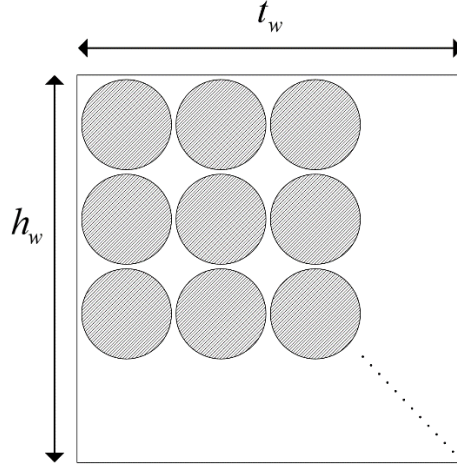


Fig. 3-14. Positions of the conductors in the winding from top view. Shaded regions represent the effective window area

Current in one coil branch I_{coil} value can be expressed as follows,

$$I_{coil} = J A_{conductor} \quad (3-50)$$

where J is the current density in A/mm^2 and $A_{conductor}$ is the cross-sectional area of a conductor. Current density value can be selected before the design process as a constant. However, this value is optimized in our design according to operating conditions. More detailed information about this process can be found in the next chapter. Rms value of the total current per phase (I_{ph}) can be calculated as follows,

$$I_{ph} = I_{coil} N_{branch} \quad (3-51)$$

Mean turn length for a coil l_t is calculated as given in Eq. (3-52).

$$l_t = l_{coil_end} + 2l_{coil_middle} + l_{coil_structure} - 2t_w \quad (3-52)$$

where l_{coil_end} , l_{coil_middle} and $l_{coil_structure}$ are lengths defined for end part, middle part and structural part of the coil, respectively. These lengths are calculated as follows,

$$l_{coil_end} = \frac{(r_{mean} - 0.5(l_m + t_w))2\pi}{N_c} \quad (3-53)$$

$$l_{coil_middle} = l_m + t_w \quad (3-54)$$

$$l_{coil_structure} = \frac{(r_{mean} + 0.5(l_m + t_w))2\pi}{N_c} \quad (3-55)$$

Resistance of one coil is calculated as follows,

$$R_{coil} = \frac{\rho_{copper} l_t N_t}{A_{conductor}} \quad (3-56)$$

where ρ_{copper} is resistivity coefficient of copper conductor. Resistance per phase value is based on resistance per coil branch and calculated as follows,

$$R_{phase} = \frac{R_{coil} N_s}{N_{branch}} \quad (3-57)$$

Resistance value given in Eq. (3-57) was calculated without thermal effects. Resistance value including thermal effects can be calculated as follows.

$$R_{phase_th} = R_{phase} (1 + \alpha_{cu} \Delta T) \quad (3-58)$$

where α_{cu} is the temperature coefficient of copper and ΔT is the temperature difference between ambient and expected operating temperature. Angular frequency and inductance of a coil are calculated as follows,

$$\omega = 2\pi f \quad (3-59)$$

$$L_{coil} = \frac{\lambda_{ind}}{I_{coil}} \quad (3-60)$$

where λ_{ind} is the flux linked by coil. Inductance value of the coil can be calculated as follows [70], [71],

$$L_{coil} = (2 \frac{\mu_0 N_t^2}{l_{ss}} ((0.5(r_o^2 - r_i^2) \tan(\theta_o)) - (t_w l_m))) + (2 \frac{\mu_0 N_t^2 t_w l_m}{l_{ss} 3}) \quad (3-61)$$

Phase reactance X_{ph} value is calculated as follows,

$$X_{ph} = \omega L_{coil} \left(\frac{N_s}{N_{branch}} \right) \quad (3-62)$$

Phase impedance Z_{ph} can be calculated using phase resistance and reactance values as follows,

$$Z_{ph} = \sqrt{R_{phase_th}^2 + X_{ph}^2} \quad (3-63)$$

3.1.3. Structural Deflection

Structural deflection is related to mechanical stability. Since proposed design has air-cored stator, there will be no attraction force between stator and rotor [68]. However, C cores try to close the airgap against each other and result in deflection in the air gap clearance. Main reason of this deflection is strong magnetic attraction forces between magnets in the air gap clearance. Ratio of this deflection with respect to airgap clearance is significant parameter in terms of structural modelling of the generator [72]. This type of deflection is shown in Fig. 3-15. In literature, air gap deflection is generally allowed between 10-20% [72]–[74]. It is desired to keep this ratio below reasonable ratio of 10% in our design.

To model the structural deflection at 2D, beam model is employed [75]. Normally C cores are exist on the web module. Therefore, length of the beam l_{beam} is limited as sum of the magnet length l_m and magnet to steel web clearance l_{cl} . Right hand side of the beam is modelled as stationary wall to show the steel web part. Beam model is given in Fig. 3-16. Normal stress q due to airgap flux density is calculated with Maxwell stress tensor as follows [63],

$$q = \frac{B_{ag}^2}{2\mu_0} \quad (3-64)$$

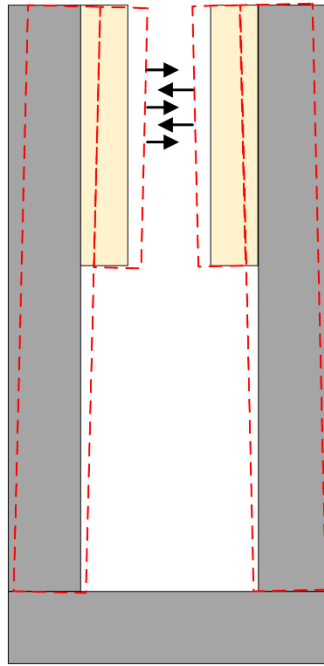


Fig. 3-15. C-core deflection due to attraction forces, deflected cores are shown with red dashed lines

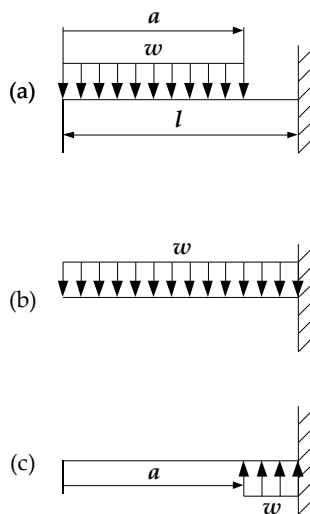


Fig. 3-16. a) Beam model for the C core deflection. b) Model for uniformly distributed load (w_{udl}) is applied at $a=0$ c) Model for uniformly distributed load (w_{udl}) is applied at limited a units along the beam [72]

Uniformly distributed load w_{udl} is calculated as follows,

$$w_{udl} = q\tau_p \quad (3-65)$$

Total deflection y is calculated by summing the two sub-models as shown in Fig. 3-16. First sub-model demonstrates the deflection y_1 when $a=0$ and the second one demonstrates the deflection y_2 when $a=l_m$. As mentioned before, beam length is calculated as follows,

$$l_{beam} = l_m + l_{cl} \quad (3-66)$$

Two beam deflections (y_1 and y_2) and resulting total deflection y are calculated as follows [76],

$$y_1 = \frac{-w_{udl}(l_{beam} - a_1)^3(3l_{beam} + a_1)}{24EI} \quad \text{for } a_1 = 0 \quad (3-67)$$

$$y_2 = \frac{w_{udl}(l_{beam} - a_2)^3(3l_{beam} + a_2)}{24EI} \quad \text{for } a_2 = l_m \quad (3-68)$$

$$y = y_1 + y_2 \quad (3-69)$$

where E and I are the Young's Modulus of steel and the second moment of inertia of steel cross-section, respectively. Young's Modulus is taken as constant as 200×10^9 Pa for structural steel. Second moment of inertia is calculated as follows,

$$I = \frac{\tau_p t_o^3}{12} \quad (3-70)$$

3.1.4. Thermal Considerations

Main heat resources in the proposed generator are copper losses of the windings and eddy losses. However, eddy losses are relatively very low with respect to copper losses because of low speed and low electrical frequency operation [63]. Therefore, current density control is the main focus of this design. When insulation class of windings (F class-155°C [77]) and operational thermal limits of permanent magnets (N50-type magnet-80°C [78]) are taken into account, forced cooling methods are more reasonable rather than natural cooling methods for such a MW-level generator. Cooling of the machine is chosen as forced air cooling in order to improve electrical

loading performance. Additionally, forced air cooling improves the magnet thermal performance and prevents them from demagnetization at extreme conditions such as short circuit faults [79]. In this study, thermal network of the machine is neglected. However, this disadvantage is compensated by forcing the optimization algorithm to converge for higher efficiency ratings. Therefore, we can determine a reference current density (A/mm²) value at 100° C operating temperature according to chosen cooling technique. Then, calculation of the temperature rise for windings ΔT can be found by using a rational relationship between “I²R” losses and current density given as follows,

$$\Delta T = \frac{(100 - T_{ambient})}{J_{ref}^2} J^2 \quad (3-71)$$

where reference current density J_{ref} is selected as 7A/mm² [51], [80], [81]. Resulting operating temperature can be found by summing the temperature rise value given above and ambient temperature $T_{ambient}$, which can be assumed as 20° C. In the optimization process, operating temperature value is calculated at every different operating speed with respect to related current density values. Other constants and reference values will be explained in the next chapter.

3.1.5. Volume and Mass Equations

Total mass of the generator consists of two main categories: active mass and structural mass. Active mass includes the materials which affect the electromagnetic performance of the machine directly while structural mass components generally provided mechanical stability to generator via non-magnetic materials. However, as the machine diameters and power ratings increase, structural mass contribution in total mass become dominant [67], [82], [83]. Since large diameter direct-driven generator concept is chosen in our design, similar structural mass dominance exists. Main duty of the structural mass parts of the machine can be summarized as transmission of the torque between shaft and air gap and maintain air gap by providing structural support against magnetic forces [72], [82]–[85]. Total mass contribution to proposed generator is included in designed system by cost

optimization. Mass components of the proposed AFPM generator can be listed as follows,

- ✓ Active mass: Steel mass, Copper mass, Permanent magnet mass.
- ✓ Structural mass: Shaft, Stator cylinder structure, Rotor torque structure, Steel band, Epoxy.

a) Active Mass Calculation

Total steel mass m_{steel} consists of three main parts: outer limb mass, inner limb mass and web mass. These mass values are calculated as follows,

$$m_{steel} = m_{out_limb} n_{out_limb} + m_{in_limb} n_{in_limb} + m_{web} n_{web} \quad (3-72)$$

Total magnet mass m_{PM} is calculated as follows,

$$m_{PM} = \pi d_{PM} h_m (r_o^2 - r_i^2) \alpha_i n_{PM} \quad (3-73)$$

Total copper mass is calculated as follows,

$$m_{copper} = h_w t_w l_k fill_{fill} d_{copper} N_c n_{stack} \quad (3-74)$$

In order to include number of parallel machines into calculation, number of layers of each component should be multiplied with related single layer mass of component as given in Eq. (3-72). A sample view of 3-stage (number of parallel machine is three) axially stacked generator is given in Fig. 3-17. As it can be seen on this figure, number of outer limbs is always two (2), regardless of the stack number of generators. Number of inner limb is always one less than that of the stack number ($n_{stack} - 1$). Number of PMs n_{PM} is always double that of the stack number ($2 n_{stack}$). Number of steel web is same as number of stacks (n_{stack}). In addition, thickness of the outer limbs are always more than that of the inner limbs due to the single-sided magnetic forces. These unbalanced forces are shown in Fig. 3-18.

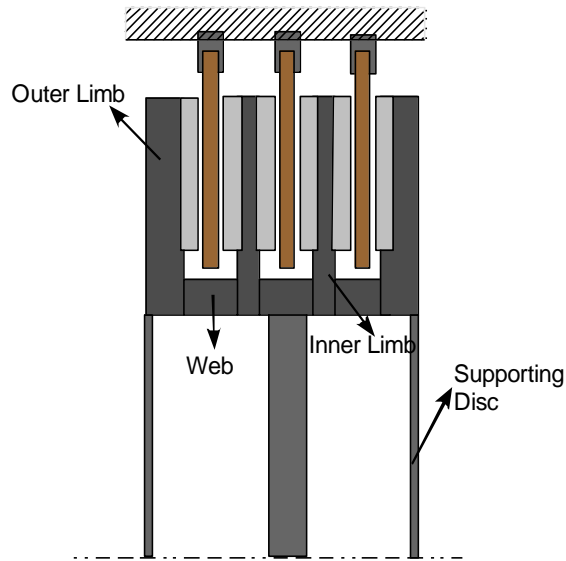


Fig. 3-17. Proposed axial flux PM generator side view with three axial stacks [63]

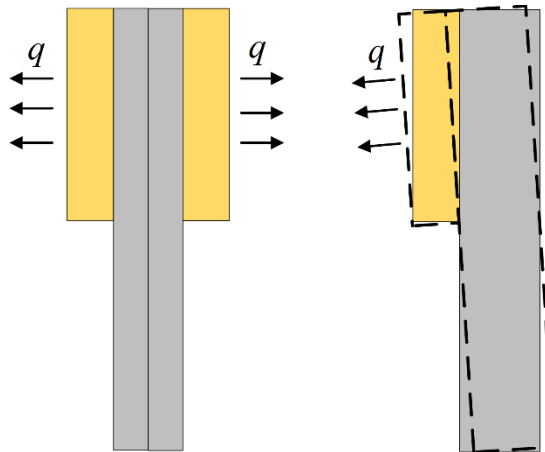


Fig. 3-18. Balanced and unbalanced forces of c-core limbs, left: inner limb case, right: outer limb case

b) Structural Mass Calculation

Total structural mass of the generator can be defined as the sum of the shaft mass, stator torque structure mass, rotor torque structure mass, steel band mass and epoxy resin mass [12], [63].

Shaft can be modelled as a hollow cylinder. Therefore total shaft mass can be calculated as follows,

$$m_{shaft} = \pi(r_{cyl,o}^2 - r_{cyl,i}^2)l_{shaft}d_{steel} \quad (3-75)$$

where $r_{cyl,o}$, $r_{cyl,i}$ and l_{shaft} are shaft outer radius, shaft inner radius and shaft length, respectively. Shaft radius values can be selected as a ratio of outer radius of machine [67]. However, these values are used as constant in the design process since mean radius hence outer radius is allowed to change in a limited range in the optimization stage. For the convenience, shaft length is selected as the 5/4 times that of the machine total axial length. Total stator mass m_{stator} consist of a stator cylinder mass $m_{cylinder}$ and two times of the stator torque arm structure mass m_{stat_torque} . Formula of this mass is given as follows,

$$m_{stator} = m_{cylinder} + 2m_{stat_torque} \quad (3-76)$$

Stator cylinder provides stiff supportive mechanism to the stator windings and mass of this structure $m_{cylinder}$ can be calculated as follows [63],

$$m_{cylinder} = \pi d_{steel} l_{shaft} ((r_o + t_w)^2 - r_o^2) \quad (3-77)$$

Stator torque structure holds the stator cylinder mechanism stable and consists of torque arms [67]. These arms are formed of rectangle steel hollow bars as can be seen on Fig. 3-19. Top view of steel hollow bars with dimensions are also shown in same figure. Stator torque arm structure mass is calculated as follows,

$$m_{stat_torque} = n_{bar,stat} (bd - b_i d_i) l_{bar,stat} d_{steel} \quad (3-78)$$

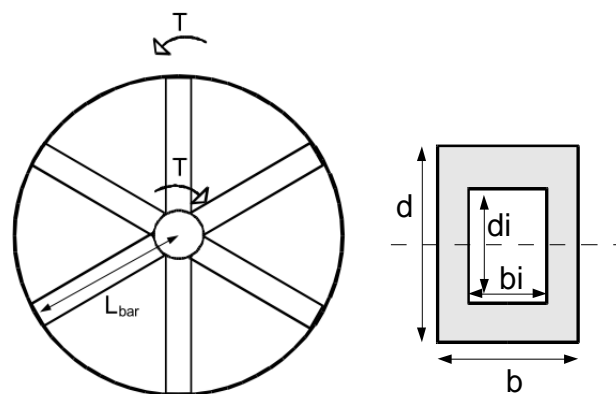


Fig. 3-19. Torque arm structure with 6 arms and Top view of steel hollow bar dimensions [63]

where $n_{bar,stat}$ and $l_{bar,stat}$ are the number of stator torque arms in a single structure and length of stator torque arms, respectively. Length of a torque arm is generally half of the stator outer diameter. b , d , b_i , and d_i are the cross-sectional distances of steel hollow bars. Dimensions used in the calculations of these values should be suitable in terms of hollow bar view. In [67], author arbitrarily selected hollow torque arm dimension for radial-flux variant, considering arm deflection cases. Torque arm dimensions can be expressed in a similar approach as follows,

$$d = 0.075l_{bar,stat} \quad (3-79)$$

$$b = 0.025l_{bar,stat} \quad (3-80)$$

$$d_i = d - 0.02l_{bar,stat} \quad (3-81)$$

$$b_i = 0.005l_{bar,stat} \quad (3-82)$$

In this thesis, arm deflections are not included in calculations. Because primary aim of the structural components is to maintain air gap clearance stable. For this purpose, core limb deflections are already calculated and kept under limited ranges with optimization. Duty of rotor torque arms is to maintain stability to C-shaped cores of rotor. Total mass of rotor torque arms (m_{rot_torque}) is calculated in a very similar way that of stator torque arm calculation:

$$m_{rot_torque} = 2n_{bar,rot} (b_{rot} d_{rot} - b_{i,rot} d_{i,rot}) l_{bar,rot} d_{steel} \quad (3-83)$$

where $n_{bar,rot}$ and $l_{bar,rot}$ are number of rotor torque arms and length of the rotor torque arm, respectively. Calculations and definitions for steel hollow torque arms for rotor are same as stator torque arm calculations. Therefore, Fig. 3-19 is valid for rotor torque arm structure. Length of rotor torque arm bar is equal to web radius r_{web} . It can be optional to use supporting steel discs instead of rotor torque arms as shown in Fig. 3-17. However, torque arm is selected for rotor support in our design due to its simple design equations. In our proposed design, 8 rotor bars and 6 stator bars are used [67]. Function of the steel band is to give mechanical support to coils and

fix them to the stator structure. A sample steel band used in proposed generator is given in Fig. 3-20. Total steel band mass is calculated as follows,

$$m_{band} = n_{stack} 2\pi(r_0 + 0.5t_w) h_{band} w_{band} d_{steel} \quad (3-84)$$

where h_{band} and w_{band} are the height and width of the steel band, respectively. These sizing values of the steel band can be determined as constant during optimization.

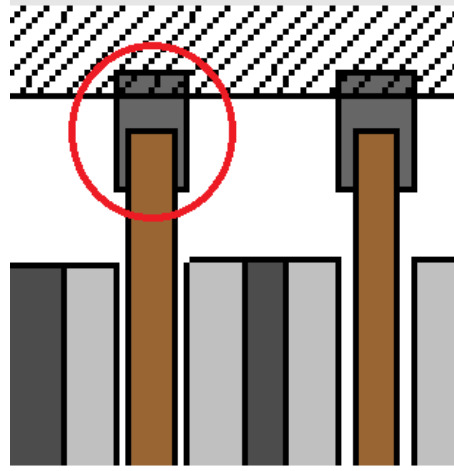


Fig. 3-20. Steel band [63]

Epoxy resin is used to fill the free space around coils and to give mechanical support and insulation for winding [34]. Its total mass m_{epoxy} in our proposed design is calculated as follows,

$$m_{epoxy} = N_c d_{epoxy} h_w (l_t t_w (1 - k_{fill}) + \tau_{former} l_m) \quad (3-85)$$

where d_{epoxy} and τ_{former} are the mass density of epoxy resin and pitch of the coil former. Main duty of the coil former is to give mechanical support to the coils from the inner side [34]. Representation of sample trapezoidal winding with distances including the pitch of the coil former is given in Fig. 3-21. A commercial coil former which has an open slots structure, is given in [86]. Mean pitch of the coil former τ_{former} can be calculated as follows,

$$\tau_{former} = \tau_c - 2t_w \quad (3-86)$$

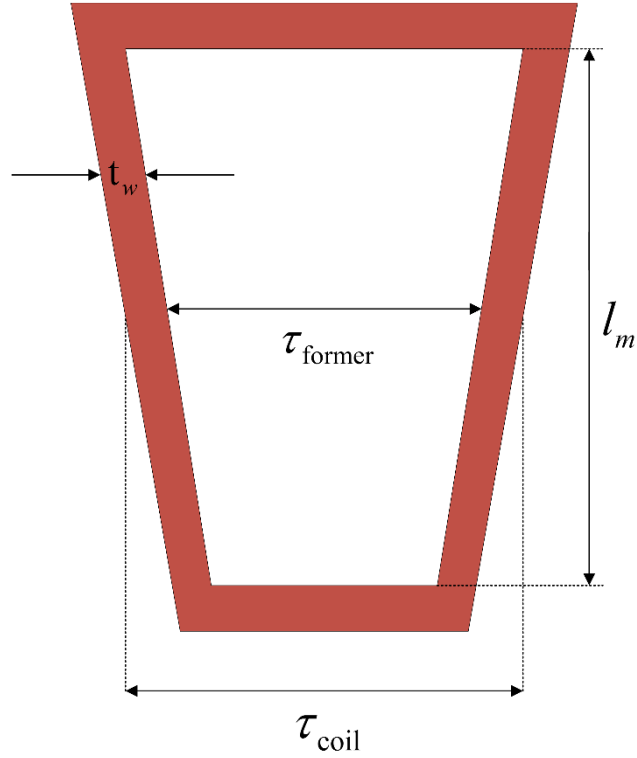


Fig. 3-21. Trapezoidal winding distances

3.1.6. Losses

Total energy loss in the generator is sum of the core losses and the copper losses.

$$P_{loss} = P_{copper} + P_{core} \quad (3-87)$$

Copper losses P_{copper} are calculated as follows,

$$P_{copper} = 3I_{ph}^2 R_{phase_th} \quad (3-88)$$

Core losses P_{core} consists of eddy losses both on coils and magnet surface. These losses are calculated as given below [70], [87], [88],

$$P_{core} = P_{eddy/coil} N_c + P_{eddy/magnet} \quad (3-89)$$

$$P_{eddy/coil} = \frac{2l_m N_t (t_{copper}/2)^3 B_{ag}^2 \omega^2 (h_{copper})}{(3\rho_{copper} (1 + \alpha_{cu} \Delta T))} \quad (3-90)$$

$$P_{eddy/magnet} = k_{eddy} l_m w_m h_m N_p^2 \quad (3-91)$$

where $P_{eddy/coil}$, $P_{eddy/magnet}$ are coil and magnet components of eddy current losses, respectively. t_{copper} and h_{copper} are thickness and height of the copper conductor, respectively. B_{ag} is the airgap flux density, k_{eddy} is the eddy loss coefficient used in calculating magnet eddy loss, N_c is the number of coils. Eddy loss coefficient is taken as constant of 18 kW/m³ for rated speed (12 rpm) from FEA eddy loss simulations and it will be changed during the optimization according to operating frequency of generator. Number of coils can be calculated as follows,

$$N_c = \left(\frac{3}{4}\right)N_p \quad (3-92)$$

Number of coils per phase ($N_{c,ph}$) is calculated by dividing N_c value by 3. Height and thickness of the coil can be expressed as follows,

$$h_{coil} = \frac{h_w - 2t_{epoxy}}{n_{turn/strand}} \quad (3-93)$$

$$t_{coil} = \frac{t_w - 2t_{epoxy}}{n_{turn/strand}} \quad (3-94)$$

where t_{epoxy} and $n_{turn/strand}$ are thickness of epoxy and number of turns per strand, respectively. Epoxy thickness value can be taken as constant (1 mm) during the design process. Number of turns per strand value is calculated as follows,

$$n_{turn/strand} = \frac{N_t}{n_{strand}} \quad (3-95)$$

where n_{strand} is the number of strand and taken as 1 in our design. Coil area including the insulation part is calculated as follows,

$$A_{coil} = \frac{(t_w - 2t_{epoxy})(h_w - 2t_{epoxy})}{N_t} \quad (3-96)$$

3.2. Electromagnetic FEA vs Analytical Evaluation for Sample Dimensions

In electrical machine design, airgap magnetic flux density is a key parameter to estimate. Because the airgap magnetic flux density affects the induced emf on stator windings via airgap flux calculations. Besides, airgap flux affects the core magnetic saturation characteristics. Hence core dimensions should be determined properly for normal flux distributions among the machine structure. Due to the reasons aforementioned above, it's important to calculate the airgap flux density parameter correctly before machine production. Finite element modelling and analysis techniques are preferred especially when the machine geometry is hard to model and calculate analytically. In this subsection, some of the machine analytic equations described earlier in this chapter and the finite element modelling results will be compared in order to confirm the design equations and techniques used in this thesis. Finite element modelling results are obtained from ANSYS Maxwell[®] 3D FEA analysis software.

To verify the design equations and techniques used in this study, airgap flux density and induced emf per phase values are chosen for the comparison. For this purpose, a 50 kW/60 rpm sample generator design is considered and evaluated in the optimization problem. Detailed information about optimization parameters and optimization process will be given in the next chapter. However, essential design parameters of the 50kW sample generator, which are achieved by the genetic algorithm optimization, are given in the Table 3-4.

Table 3-4. Optimized design parameters of the sample 50 kW generator

Parameter	Value
Rotational speed (n)	60 rpm
Mean radius (r_{mean})	0.7 m
Phase current ($I_{ph,rms}$)	5.3 A
Airgap clearance (g)	2 mm
Voltage per phase ($V_{ph,rms}$)	977 V
Induced emf per phase rms ($E_{ph,rms}$)	1058 V
Induced emf per phase peak ($E_{ph,peak}$)	1496 V
Number of turns (N_t)	146
Number of poles (N_p)	96
Output power (P_o -per stack)	15,396 W
Phase resistance (R_{phase_th})	14.92 Ω
Current density (J)	4 A/mm ²
Steel web clearance (l_c)	16 mm
Fundamental airgap flux density peak value ($B_{ag,1}$)	0.67 T
Airgap Flux Density (flat-top)	0.57 T
Height of the winding (h_w)	13 mm
Winding thickness/Coil pitch ratio (α_{pitch})	0.369
Fill factor (k_{fill})	0.65
Height of the magnet (h_m)	10 mm
Length of the magnet (l_m)	87 mm
Magnet pitch-to-pole pitch ratio (α_i)	0.76
Number of parallel branches (N_{branch})	1
Number of parallel machines (n_{stack})	3
Efficiency (η)	92.38 %
Total mass (active + structural)	1024 kg

The peak value of the fundamental harmonic of the airgap flux density $B_{ag,1}$ is calculated according to Eq. (3-42). As it can be seen on the Table (3-4), this value is calculated as 0.67 T in our optimization process by using genetic algorithms. In the finite element analysis side, this peak flux density value is found as 0.65 T. For simplicity of the analysis 4 pole symmetric model is used in the analysis. Airgap flux density vector variation is recorded along the line which is shown in Fig. 3-22. This sinusoidal variation is shown in Fig. 3-23. Also in this figure, analytically calculated airgap flux densities are shown. As can be seen from the figures, the peak value of the flux density is 0.65 T. Therefore it can be said that analytic equation results and finite element analysis results show good agreement in terms of airgap flux density.

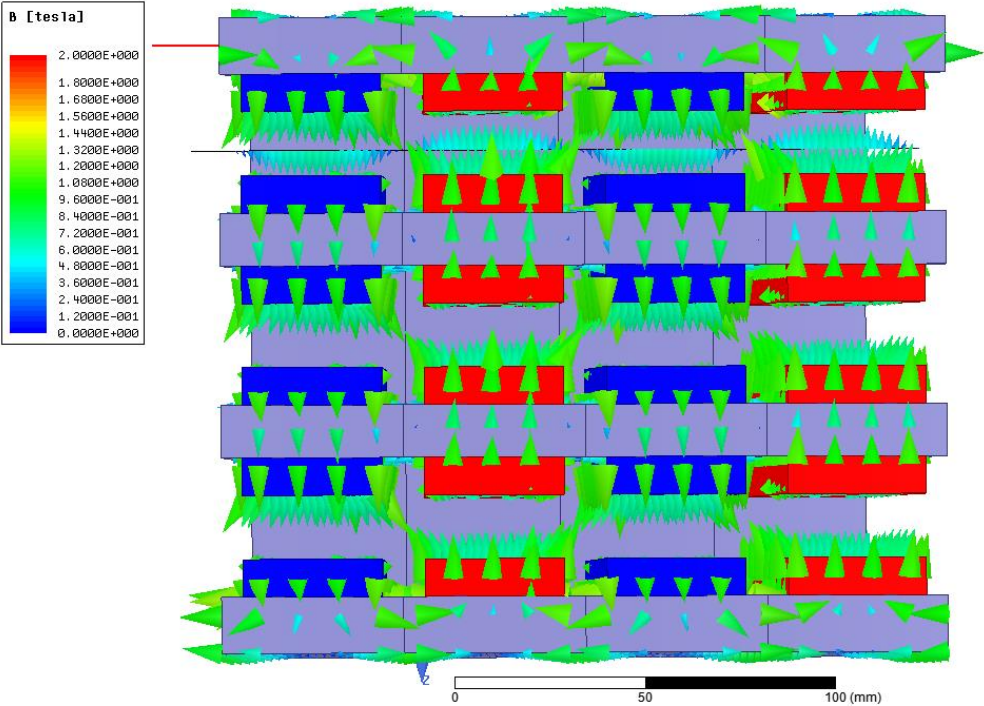


Fig. 3-22. Airgap flux density vectors for the sample 50 kW design

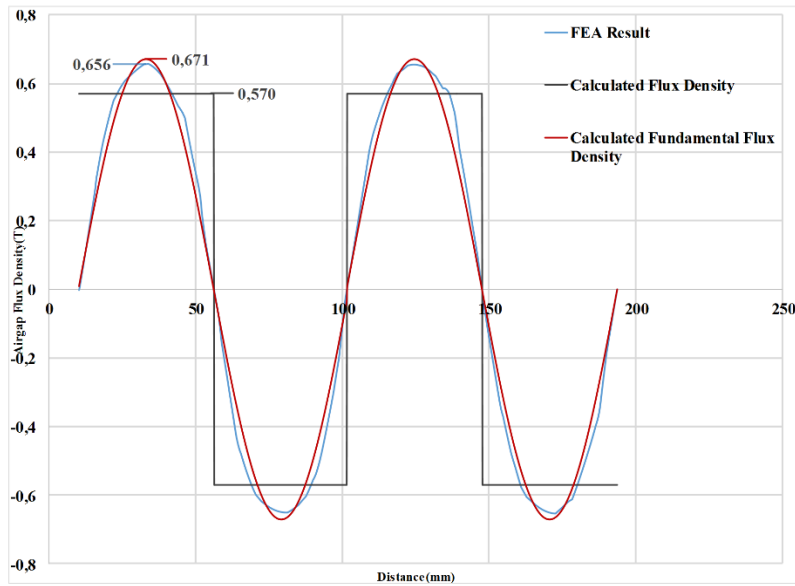


Fig. 3-23. Airgap flux density graph with analytical results for the sample 50 kW design

Sinusoidal flux density variation induces sinusoidal voltages on windings. In our analytical design equations, induced emf (peak) per phase is calculated via Eq. (3-46). As it can be seen on Table 3-4, this value is calculated as 1496 V. Induced emf per phase peak value of the finite element analysis is given in Fig. 3-24. This graph is obtained for three phase at rated speed of 60 rpm. All three phases are balanced (120° phase difference) in time domain and they all have peak magnitude of nearly 1600 V. Therefore, it can be inferred that analytic equation results and finite element analysis results show good agreement in terms of induced emf. In Table 3-5, comparison of flux densities and induced emf values of both analytical calculations and FEA results are given with related error rates.

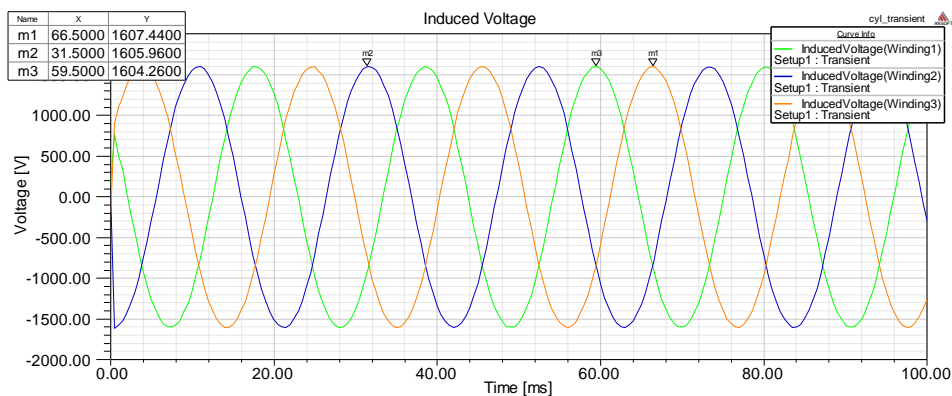


Fig. 3-24. Induced emf per phase graph for the sample 50 kW design

Table 3-5. Comparison of the critical parameters of analytical and FEA results for the sample AFPM design.

	Analytical	FEA	Error
Peak airgap flux density ($B_{ag,1}$)	0.67 T	0.65 T	3%
Peak induced emf ($E_{ph,peak}$)	1496 V	1600 V	6.5%

3.3. Conclusion

In this chapter, analytical design equations of the proposed AFPM generator are described. In the first section, mechanical and electrical parameters of the proposed generator are covered with related graphics and mathematical expressions. These design equations are mainly consist of; fundamental generator equations, geometrical and structural equations, phase turns, resistance and flux density equations, thermal equations, reluctance network and related equations, volume and mass equations and finally power and efficiency calculations. During the design of the proposed generator leakage fluxes are taken into consideration. Unity power factor is assumed for the phasor equations due to selection of vector control in the power electronic stage. These design equations are very important as their results will be used in the optimization process and finite element design. In the second section of the chapter, comparison of the results of the analytical calculations and the finite element analysis is given for a sample 50 kW AFPM generator in order to verify the design method followed in this thesis study. For this purpose, airgap flux density and induced emf per phase parameters are chosen since they've been used widely in the design of electrical machines as key parameters [70]. It is concluded that the results of the analytical equations and the results of the FEA are in good agreement. Therefore, these analytical equations can be used in the optimization for the proposed AFPM generator design.

CHAPTER 4

OPTIMIZATION AND DESIGN

4.1. Introduction

In the previous chapter, electrical and mechanical design parameters, mathematical design equations and related drawings of the selected axial flux permanent magnet generator are presented. These equations are important for this thesis work, as they are used in the main design algorithm. Also in the previous chapter, verification of the analytical equations of the some important design parameters is given by means of finite element analysis of a sample design. For this purpose, comparison of the design equations and the finite element analysis is made in terms of air gap flux density and induced emf. It's concluded that the results show good agreement. Therefore, these equations can be used in the optimization algorithm. In this chapter, optimization process of the given design will be summarized and the optimum design parameters of the proposed 5 MW AFPM generator will be determined. Firstly, evolutionary algorithms (EA) will be reviewed, including the chosen genetic algorithm (GA). Then, process of the genetic algorithm based optimization method, which is used in this thesis study, will be explained in detail. Optimization of the proposed generator is realized in MATLAB optimization toolbox. Also in this chapter, a brief information of this toolbox and used parameters in the optimization algorithm will be covered. Finally, optimum design parameters of the proposed 5 MW 12 rpm AFPM generator will be presented. These design parameters will be used in the finite element modelling and analysis in the next chapter.

4.2. Evolutionary Algorithms (EA) and Genetic Algorithm (GA)

There exist different mathematical search algorithms and conventional methods for modern world engineering problems. However, multi-variable nonlinear problems require new methods to avoid from getting stuck into local minimums during the

optimization process [89]. The main motivation of the Evolutionary Algorithms (EA) is to mimic the nature to find the optimum solutions to these problems. EA can be evaluated as a direct, stochastic and population-based search algorithm. There are three main rules of biological processes which inspire the EA based search algorithms. These processes can be summarized as follows;

- **Continuous evolution process** which occurs at the most basic level of “source-code” of living beings, i.e. chromosomes
- **Natural Selection mechanism** in which the fittest individuals in a society can have more chance to survive and have more robust offspring than those who are not fit at all.
- **Evolutionary process at reproduction** which is done by the reproduction operators such as cross-over and mutation.

EA mimics the natural selection of living beings. Fittest one in the group has more chance to survive and to breed. Individuals correspond to encoded solutions of the given problem. Every individual has a fitness value which is calculated by the objective function of the problem. Algorithm itself evaluates the “adaptive skills” of every individual according to its fitness value. Least “fit” individuals are eliminated from the population, hence more adapted and robust individuals replace the old generations. Fitness value is the only required quantitative information about the individual in EAs, contrary to other search techniques such as gradient based optimization methods, in which derivative information is needed [63], [90]. Another advantage of evolutionary search algorithm is the population based evaluation, which is a big computational advantage over the conventional search algorithms which sample one individual at a time. This population leveled optimization is more advantageous especially when working with large search spaces [91], [92]. In Fig. 4-1, a classification table of the search techniques is given.

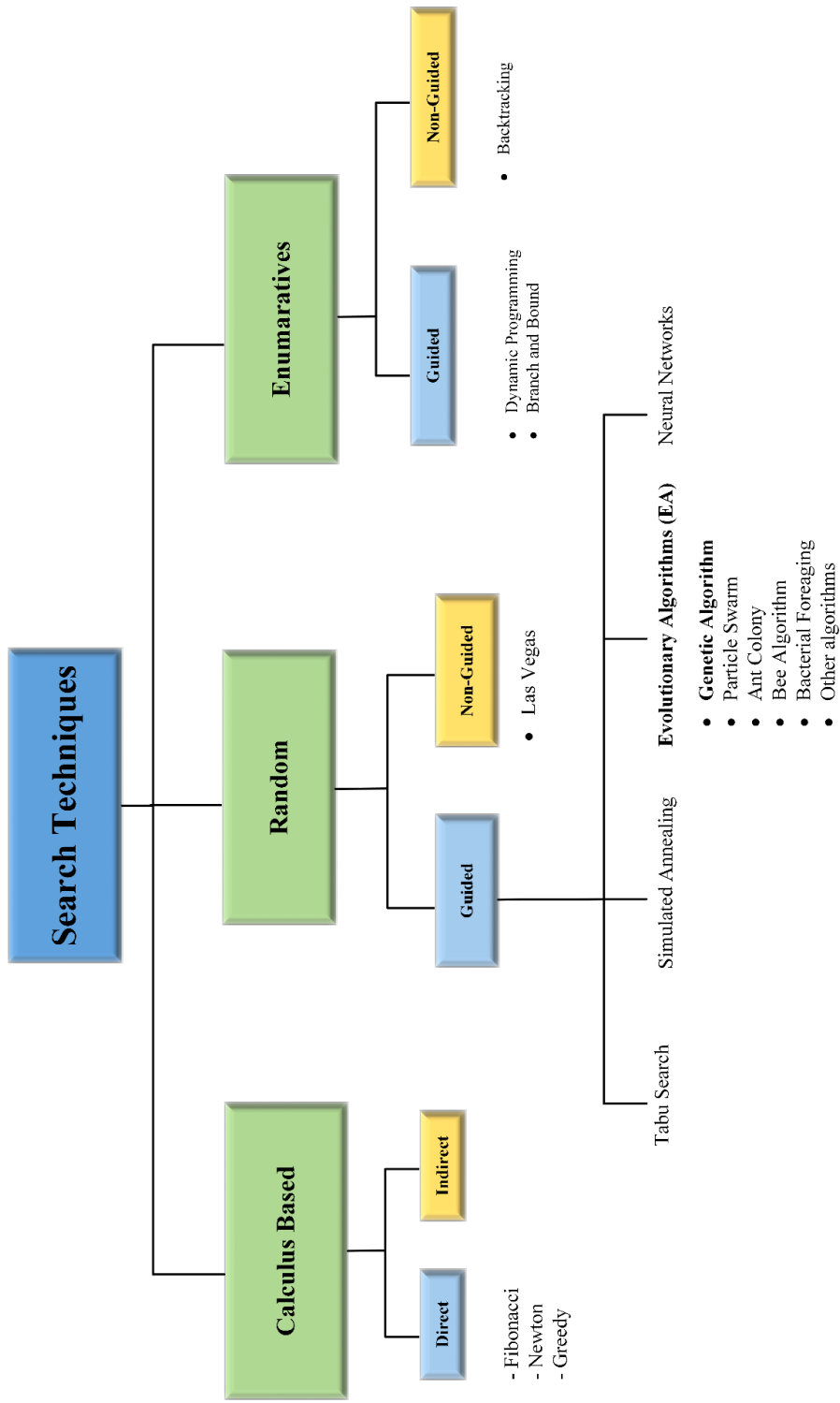


Fig. 4-1. Classification of the search techniques [89], [92], [114]

The most popular search technique among other techniques in the EA family is the genetic algorithm (GA). In this algorithm, individuals are generally represented as fixed-length bit strings as shown in Fig. 4-2 and Fig. 4-3. Different cell positions in these strings contains information which corresponds to different properties of the individual they represent [92]. Two frequently used operators during the reproduction stage of GA are cross-over and mutation operators. Various “individuals” or various “solutions” can be obtained during the optimization process by using these two operators. Working principles of cross-over and mutation operators are depicted in Fig. 4-2 and Fig. 4-3, respectively. In cross-over, data interchanges between parents around the crossover point which determined in the reproduction stage. However, in mutation, random new data is written to randomly selected locus on the selected “chromosome” or “individual”.

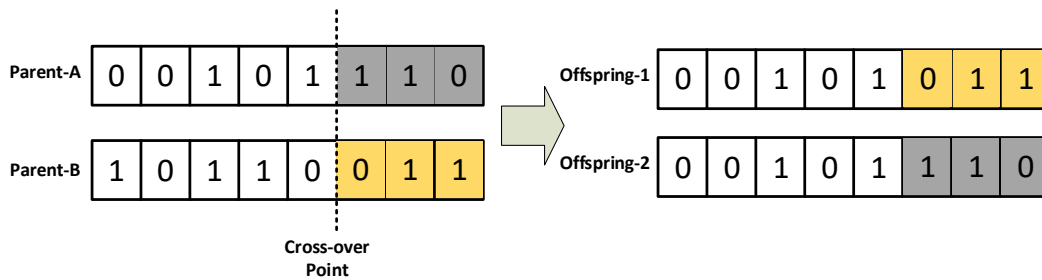


Fig. 4-2. Bit string cross-over operation between parent individuals [92]

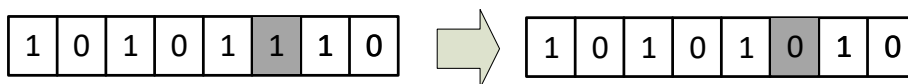


Fig. 4-3. Bit string mutation operation [92]

Evolutionary algorithms start with the initial population where values of the initial variables are selected randomly by selection operators based on stochastic methods. Successive generations are created based on the selection and the reproduction principles. Population size is preserved throughout the generations. Optimization algorithm stops when termination criteria are satisfied [91], [92]. These criteria can be different conditions such as predetermined fitness value, predetermined number of successive generation or limited time.

Every problem can be solved by using EA as long as it is expressed with a proper fitness function. User should define a fitness function such that generations could converge to optimal solution. Therefore, every constraint parameter and penalty coefficient corresponding to it should exist in the fitness function maybe not equally but in a weighted form [63]. Penalty coefficients and related definitions will be covered in the following sections. Another advantage of EAs is that it can be combined with other conventional search techniques. EAs can be utilized in a parallel fashion in order to evaluate the fitness among the candidate solutions, as mentioned before. Possibility of converging local minimum is decreased due to this parallel process. Because of the high computational burden related to larger search spaces and hybridization processes, optimization techniques by using distributed computing gaining attention [92]. Also, evolutionary algorithms can easily adapt to changing environmental conditions. Therefore, it's not necessary to restart the algorithm in case of sudden changes, contrary to as it was in the conventional search methods [89].

To sum up, evolutionary algorithms gaining popularity especially in the last two decades due to advantages aforementioned above although first attempts to use evolutionary techniques in optimization problems were made in nearly 60 years ago [91], [92]. There are two biggest key aspects of this search technique. One of is that the similarity between the nature during selection and variation stages. The other one is that it is not necessary to provide mathematical information except fitness function in order to evaluate generations of individuals [93]. Additionally, there exist a large application area of this algorithm from medical treatments to advanced engineering problems [94]. This application area seems to enlarge due to new explorations of evolutionary genetics science in biology and increased computer capacities.

4.3. Genetic Algorithms Based Optimization

Genetic algorithms (GA) are stochastic search techniques and exist on the subgroup of evolutionary algorithms. GA was first proposed by John Holland in 1975 with the aim of investigating the usage of natural evolutions for optimization principles

[91]. The most salient feature of the GA among the other search techniques is that it doesn't need derivative information of the related search space. This feature helps GA to avoid trapping at local minimums [12], [94]. Algorithm itself based on the three operators namely selection, crossover and mutation [91], [95]. As it was in the evolutionary algorithm case, GAs can also explore the search space in a parallel fashion. Another advantage of GA is that optimization procedure can converge to global minimum solution regardless of the starting point. Crossover and mutation definitions are same for the GA, as it was mentioned in the previous section. For an effective optimization, options of the GA such as population size, cross-over and mutation possibilities and termination criteria, should be suitably configured [96].

General flowchart of a GA is given in Fig. 4-4. However, it is useful to describe some of the technical terms about GA before continue with the flowchart.

- *Gene* is a parameter which defines the specific trait of the considered solution such as stator outer diameter, axial length or air gap flux density. This parameter is encoded in the related locus of fixed-length chromosome.
- *Chromosome* is the combined form of genes, thus representing a complete “individual”.
- *Locus* is the specific position of encoded data exist in each string of individual or solution.
- *Fitness* is the measure of suitability of a generated solution for the given optimization problem. This numeric value is used by the GA when evaluating and selecting the best individual from the candidate solutions. Because of this reason GA optimizations are usually mentioned with the term “survival of the fittest”. Fitness function of the optimization problem should be constructed carefully in order to obtain the optimum design parameters of the selected AFPM topology.
- *Selection* used in GA is mainly based on stochastic processes and natural similarities. However, there are different selection methods for application such as roulette wheel selection and tournament selection [90], [92].

- *Population* can be considered as a group of individuals in one generation. Larger sizes of population leads to longer solution times but larger search spaces.
- *Generation* is the set of individuals employed in one cycle of optimization. As the evaluated number of generations are increased, more fit solution candidates will be created by the GA.
- *Elitism* is related to best individuals which are preserved and directly pass to next generation without any gene manipulation. If number of elite is too much generations don't change much and diversity decreases. If number of elites is low then optimization lasts longer to converge to global minimum because of large diversity.
- *Independent variable* is an optimization parameter which is changed by the GA at every iteration. For example in this thesis work, there are 15 different independent variables in the optimization process of the proposed AFPM.
- *Penalty function* is a concept that is used to convert a constrained optimization to an unconstrained optimization problem. Main idea in this concept is that to “penalize” the individuals with additional higher fitness values, whose solution parameters violate the limits of predetermined constraints.

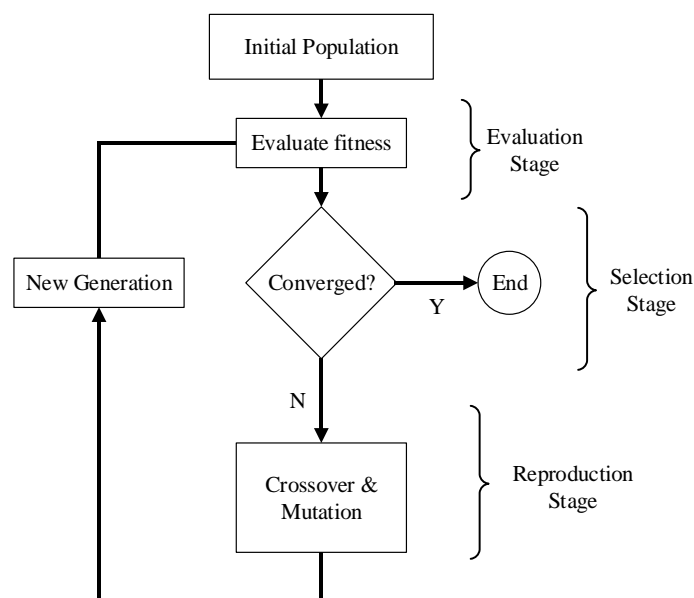


Fig. 4-4. General flowchart of a GA optimization [96]

4.4. Optimization Implementation

4.4.1. MATLAB Toolbox and Configurations

In this thesis, optimization procedure is implemented by MATLAB optimization toolbox. For this purpose, three different codes, which include the necessary design equations described in the previous chapter, are written and tested in the MATLAB environment. These codes are mainly performs following actions;

- Optimization main handling and saving performance parameters
- Iterative loop for required multi-speed operation calculation
- Main design calculation of the generator for a given set of variables

In our design, objective function is constructed based on the cost of the proposed generator. Therefore, GA tries to minimize the total cost of the generator by using different mass combinations of different materials used in the generator. Details of the objective function and constants will be given in the following subsections. In this subsection, details and the configurations of optimization procedure will be described. Configuration parameters used in the optimization process are given in Table 4-1.

Table 4-1. Configuration parameters of the MATLAB optimization toolbox

Solver	Genetic Algorithm
Number of variables	15
Population Size	100
Fitness Scaling	Rank
Selection Function	Stochastic Uniform
Elite Count	1
Crossover Fraction	0.9
Mutation	Gaussian with Scale/Shrink
Crossover Function	Scattered
Number of Generation	200
Stall Generations	50
Stall tolerance	1×10^{-6}

As seen from Table 4-1, there are 15 different independent variables used in our design optimization. Selection is realized via stochastic uniform function based on the fitness value. In this function, individuals have probability to be selected by the GA inversely proportional to their rank value. Therefore, individuals with lower rank value have more chance to be selected. Cross-over fraction determines the rate of the individual in a population (except the elite ones) which are subjected to cross-over operation during the reproduction stage. Higher rates of this parameters results in higher diversity despite longer solution times. Cross-over is realized via scattered function. In this function first a random vector, which consists of random binary numbers, is created. Then this random vector is compared with the selected parent vectors in bit-wise. Variables of the offspring individual created according to this comparison. If binary number is 1 then “gene” is taken from first parent otherwise second parent gives the related gene from its corresponding locus [97].

In our optimization process two different termination criteria are defined as it can be seen on Table 4-1. Optimization process will stop either when the total number of generation is equal to 200 or when 50 successive generations occur with average difference in fitness function is lower than “Stall tolerance”. GA in MATLAB searches for the optimum set of parameters between the predetermined lower and upper boundaries. Independent variables of the optimization can be seen in Table 4-2 with their definitions and related boundaries.

Air gap clearance g is segregated from this table because it is taken as constant. As it will be mentioned in the following sections, constant value of air gap is taken as 10 mm for our proposed generator and stator outer diameter is limited to 10 meters by optimization. Main reasons of this selection are production limitations and “1/1000 air gap diameter ratio” convention [48], [83] which will be explained in the following sections. Current density optimization range is determined based on the thermal considerations which were mentioned in the previous chapter. Magnet/steel width ratio, pitch ratio and fill factor ranges are selected based on the literature and conventional practices [65], [98].

4.4.2. Flowchart and Objective Function

In this thesis work, considered AFPM design problem can be described as a non-linear optimization problem. Nonlinear constrained optimization problems are generally expressed as follows [12], [99],

$$\text{Minimize } F(x) \quad (4-1)$$

$$g_i(x) \leq b_i \quad i=1,2,3,\dots,p \quad (4-2)$$

$$h_j(x) = d_j \quad j=1,2,3,\dots,q \quad (4-3)$$

$$\text{bound}_l \leq x \leq \text{bound}_u \quad (4-4)$$

Table 4-2. Independent variables of the optimization

Variable Vector-x	Variable Definition	Lower boundary	Upper boundary	Unit
x(1)	Mean radius (r_{mean})	4	5	m
x(2)	Current Density (J)	1	7	A/mm ²
x(3)	Outer limb thickness t_o	0.03	0.045	m
x(4)	Inner limb thickness t_i	0.02	0.03	m
x(5)	Steel web thickness l_c	0.02	0.03	m
x(6)	Magnet/steel width ratio α_i	0.7	0.8	-
x(7)	Number of turns N_t	40	90	Turn
x(8)	Number of poles N_p	200	260	Pole
x(9)	Number of branches N_{branch}	4	6	Branch
x(10)	Height of the winding h_w	0.03	0.045	m
x(11)	Pitch ratio α_{pitch}	0.3	0.4	-
x(12)	Fill factor k_{fill}	0.6	0.7	-
x(13)	Height of the magnet h_m	0.01	0.02	m
x(14)	Length of the magnet l_m	0.25	0.3	m
x(15)	Number of parallel stacks n_{stack}	3	6	-

where $F(x)$ corresponds to objective function and x represents the set of the independent variables. Conditions given in the Eq. (4-2) and Eq. (4-3) are defined as inequality constraints and equality constraints to which objective function is subjected. As mentioned before, variable set is chosen between lower and upper bound intervals which are predetermined before GA optimization process. These boundaries are shown in Eq. (4-4). In this study, main objective function is constructed based on the cost of the designed generator and can be expressed as follows,

$$F(x) = 1.2(\text{cost}_{\text{steel}} + \text{cost}_{\text{copper}} + \text{cost}_{\text{magnet}} + \text{cost}_{\text{structure}}) \quad (4-5)$$

where $\text{cost}_{\text{steel}}$, $\text{cost}_{\text{copper}}$, $\text{cost}_{\text{magnet}}$ and $\text{cost}_{\text{structure}}$ are cost of steel, cost of copper, cost of permanent magnet and cost of structure, respectively. Coefficient of “1.2” is multiplied by the total material cost due to add the approximately 20% labor cost effect to the material cost. Cost components of the main objective function given in Eq. (4-5), can be calculated as follows,

$$\text{cost}_{\text{steel}} = m_{\text{steel}} \text{uc}_{\text{steel}} \quad (4-6)$$

$$\text{cost}_{\text{copper}} = m_{\text{copper}} \text{uc}_{\text{copper}} \quad (4-7)$$

$$\text{cost}_{\text{magnet}} = m_{\text{PM}} \text{uc}_{\text{magnet}} \quad (4-8)$$

$$\text{cost}_{\text{structure}} = (m_{\text{shaft}} + m_{\text{stator}} + m_{\text{rot_torque}} + m_{\text{band}}) \text{uc}_{\text{steel}} + m_{\text{epoxy}} \text{uc}_{\text{epoxy}} \quad (4-9)$$

Penalty functions are defined and used in order to convert our constrained optimization problem to an unconstrained optimization problem. Therefore, it is not necessary to define equality and inequality constraints in MATLAB optimization toolbox. Penalty functions are used such that an additional value, which is to be added to original objective function, is calculated proportional to measure of violation of a constraint [12], [92]. In this study, seven different constraints are added in a form of penalty functions to the main objective function. Details of the constraints will be given in the following subsections. Resulting objective function in which the penalty functions added form is given as follows,

$$F(x) = 1.2(\text{cost}_{\text{steel}} + \text{cost}_{\text{copper}} + \text{cost}_{\text{magnet}} + \text{cost}_{\text{structure}}) - f_{\text{income}}(x) + \sum_{i=1}^7 p_i(k_i) \quad (4-10)$$

where $p_i(k_i)$ and k_i are the penalty function for i^{th} constraint and penalty coefficient for i^{th} penalty function, respectively. Details of the penalty functions will be given in the following sections. Income function $f_{\text{income}}(x)$ is utilized in order to include the effects of energy ratio and time probability of the wind in the total energy production for a proposed generator. This function is calculated as follows,

$$f_{\text{income}}(x) = P_o \text{price}_{\text{elec}} f_{\text{avail}} f_{\text{time}} (365 * 24) \quad (4-11)$$

where P_o is the net output power from the generator, $\text{price}_{\text{elec}}$ is the electricity price per kWh sold by the WPP and taken as 7.3 ¢ (USD dollar cent) in this study [100], f_{avail} is the availability factor for proposed wind turbine and taken as 0.9 and finally f_{time} is the time probability of the related wind speed.

Flowchart of the used optimization algorithm in this study is given in Fig.4-5. First, an initial population is created by the MATLAB optimization tool based on the configurations given in Table 4-1. Then, the reference wind speed data is taken from wind-speed data table. Current density is initially assigned as the half of the upper limit of the current density, namely $J_{\text{max}}/2$. Then this current density value, rpm value and demanded power are used together with the created random independent variables in order to calculate the design parameters of the generator. After the first design calculation, current density value is adjusted according to efficiency of the design and reference current density values calculated for steady state and short circuit fault conditions. Then a final design calculation is made for the current rpm interval. This calculations are repeated for all 9 operating conditions for the same design to evaluate performance of the generator at different wind speeds. Cost function is calculated according to objective function defined in Eq. (4-10) by considering the energy ratios of the different wind speed intervals given in the reference wind-speed data table. Then, termination criteria are checked in order to stop the optimization process. This procedures are repeated until termination criteria

are satisfied and the optimal design is achieved. Details of the aforementioned variable speed conditions will be covered in the next section.

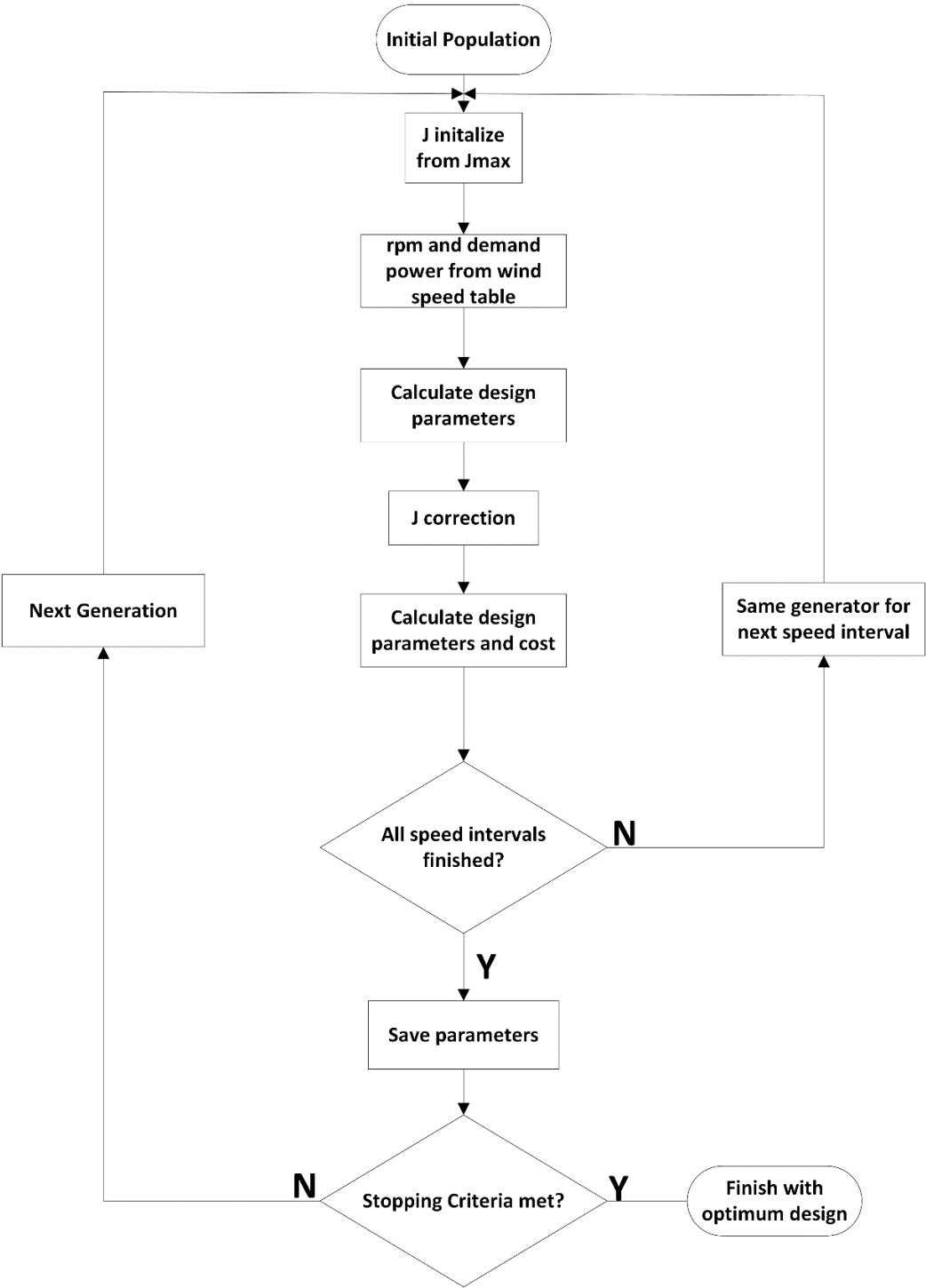


Fig. 4-5. Optimization flowchart

4.4.3. Operating Conditions of the Generator

If design calculations of a wind turbine generator are only based on the rated speed and power output conditions, probably manufactured design will not be efficient as much as it was in the design stage. This is due to irregular nature of the wind. Therefore, variable speed operation must be taken into account and different speed distributions of the turbine must be evaluated during the optimization. In this study, design optimization of the proposed AFPM generator is carried under 9 different wind speed conditions with respect to given time probabilistic densities. For this purpose, wind speed measurements data of a sample WPP, located in Çanakkale/Turkey, is used. In Fig. 4-6, time probabilities of the wind speed intervals are calculated based on the one year period of measurement data. As it can be seen from this figure, wind speed density plot shows a typical Weibull distribution.

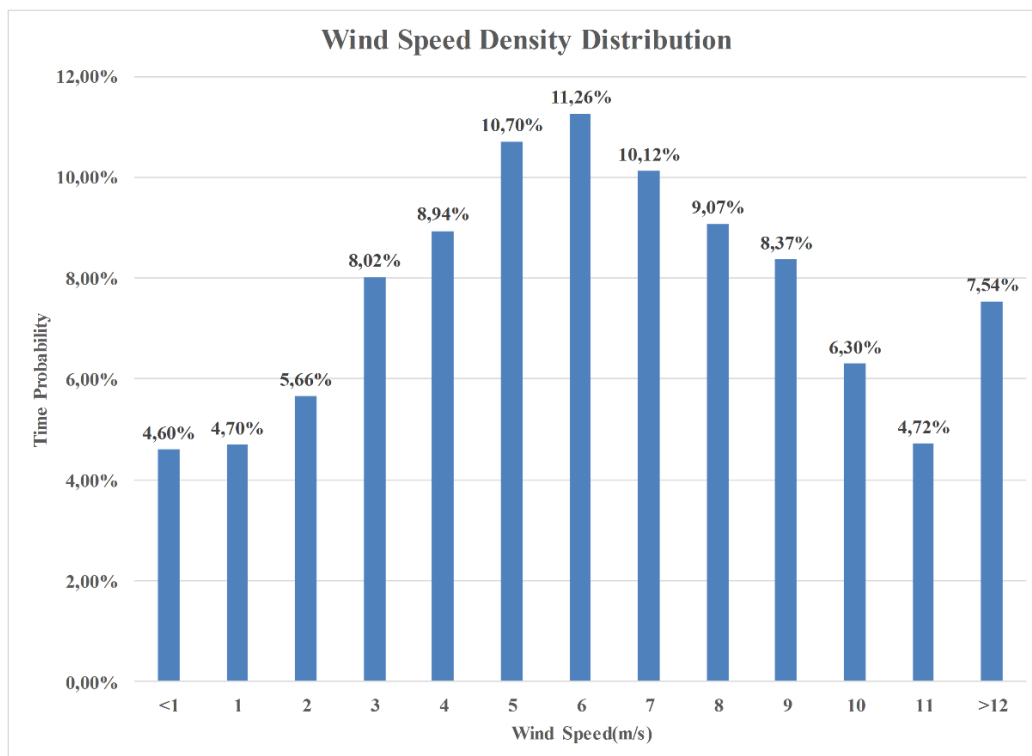


Fig. 4-6. Wind speed density distribution from measurement data

Different properties of the wind speed distribution and a 5MW “reference” wind turbine [101] characteristics under these wind conditions, which are desired to be reached by the optimized AFPM generator of this study, are tabulated in Table 4-3.

Table 4-3. Wind speed distributions and reference generator ratings

Wind Speed	Average Speed (rpm)	Average Torque (kNm)	Output Power (kW)	Time Probability	Energy Ratio
4 m/s	1	187.5	195	31,92%	4,09%
5 m/s	1	4038,5	420	10,70%	2,95%
6 m/s	2.9	2606,1	786	11,26%	5,81%
7 m/s	4.8	2596,2	1296	10,12%	8,61%
8 m/s	6.7	2788,5	1943	9,07%	11,57%
9 m/s	8.6	3017,7	2699	8,37%	14,84%
10 m/s	10.5	3193,2	3487	6,30%	14,43%
11 m/s	12	3344,6	4174	4,72%	12,94%
>12 m/s (Rated)	12	4006,4	5000	7,54%	24,76%
Weighted Average (time)	4.7	2154,9	1522,6	100,00%	100,00%

4.4.4. Constants and Constraints

a) Constants

Although there are 15 independent variables in our optimization, some other variables and parameters can be taken as constant based on the assumptions and experiences in order to simplify the optimization handling and to avoid large and complex search spaces. Conceptual constants aforementioned above are given in Table 4-4 for our proposed AFPM.

Air gap clearance value is determined based on the cost comparison of designs with different air gap values. Besides, selected 10 mm of air gap clearance value is consistent with the assumption of “air gap clearance could be nearly 1/1000 of the

air gap diameter” principle of electrical machine design [48], [83]. In addition to this principle, 10 mm air gap is also selected for comply the production limitations. Current density is optimized during the optimization process with other independent variables. However, final value of this variable is determined by the iterative design loops in the multi-speed code, instead of a random number assigned by the GA.

Table 4-4. Conceptual optimization constants of the proposed AFPM generator

Constant	Value
Air gap clearance	10 mm
Number of phases	3
Ambient temperature	20° C
Current Density	Forced air cooling with 7 A/mm ² @100°C
Power factor angle	0° (cosφ=1)
Coil pitch/Pole pitch	4/3

In order to do this, predetermined current density value (7 A/mm² for this design) is assumed for reference operational temperature at 100°C [51], [80], [81]. Operating temperature and final value of the current density are calculated according to this current density reference-based iterative loops in the design code. Thermal considerations about the design were expressed in the previous chapter. Although thermal network is neglected, high efficiency is preferred by the optimization algorithm. Power factor is assumed as unity in our design. This assumption is based on a vector controlled power electronic converter which connects the proposed AFPM generator to grid [102]. Ratio of “4/3” between the coil pitch and the pole pitch is selected as it is advantageous rather than other ratios in terms of induced emf magnitude. This magnitude variation was mentioned and depicted in Fig.3-2 in Chapter-3.

In addition to conceptual constants described above, there are number of constants related to material characteristics such as mass density and remanence flux density. These constants used in the optimization are given in Table 4-5.

Table 4-5. Material constants of the proposed AFPM generator

Constant	Definition	Value
α_{cu}	Temperature coefficient of copper	$3.9 \times 10^{-3} \text{ } ^\circ\text{C}^{-1}$
ρ_{copper}	Resistivity coefficient	$1.7 \times 10^{-8} \text{ ohm.m}$
h_{band}	Height of the band	0.01 m
w_{band}	Width of the band	0.04 m
B_r	N50 grade PM remanent flux density [69]	1.4 T
μ_r	PM relative permeability	1.05
μ_{st}	Steel relative permeability	750
c_{w2sw}	Winding-steel web distance	0.015 m
k_{leak}	Leakage coefficient	0.95
t_{epoxy}	Epoxy thickness	1 mm
d_{steel}	Mass density of steel	7850 kg/m^3
d_{copper}	Mass density of copper	8960 kg/m^3
d_{PM}	Mass density of PM	7500 kg/m^3
d_{epoxy}	Mass density of epoxy	1150 kg/m^3
$r_{cyl,o}$	Shaft outer radius	0.3 m
$r_{cyl,i}$	Shaft inner radius	0.1 m
uc_{steel}	Unit cost of steel[103]	\$ 3 /kg
uc_{magnet}	Unit cost of PM[103]	\$ 80 /kg
uc_{copper}	Unit cost of copper[103]	\$ 10 /kg
uc_{epoxy}	Unit cost of epoxy[93]	\$ 0.4 /kg

b) Constraints

Constraint in an optimization problem can be due to physical properties of the materials or due to designer's priorities. In this study, independent variables are allowed to vary between lower and upper bounds of the predetermined search space. However, sometimes selection of these variables by GA can result in improper consequences. Therefore this kind of faulty selections must be corrected by the optimization programming at each generation [12]. This type of corrections in this study can be listed as follows,

- ❖ Number of turns (N_t), number of poles (N_p), number of parallel branches (N_{branch}) and number of stacks (n_{stack}) are selected as integer variables.
- ❖ In addition to that, number of poles are rounded nearest integer which is multiple of four, in order to get a suitable number of series connected coils. This relationship can be expressed as follows;

$$N_s = \frac{N_{c,ph}}{N_{branch}} \quad (4-12)$$

where $N_{c,ph}$ represents the number of coils per phase and calculated as follows for 3-phase system,

$$N_{c,ph} = \frac{N_c}{3} \quad (4-13)$$

We know that, there is a (4/3) ratio between number of poles and number of coils:

$$N_c = \left(\frac{3}{4}\right)N_p \quad (4-14)$$

Therefore, number of series connected coils can be calculated as follows,

$$N_s = \left(\frac{3}{4}\right)N_p \frac{1}{3N_{branch}} = \frac{N_p}{4N_{branch}} \quad (4-15)$$

In the design code, number of parallel branches N_{branch} selected so that N_p / N_{branch} division can be calculated as an integer value.

- ❖ Winding thickness/coil pitch ratio is also controlled in case any improper former dimensions such as negative former pitch. Pitch of the coil former is calculated by using Eq. (3-85) in the previous chapter.
- ❖ Outer core limbs must be always thicker than inner core limbs in order to withstand single-sided magnetic forces. Considerations about deflection were mentioned in the previous chapter.
- ❖ Magnet/steel width ratio should be selected in proper limits in order utilize the magnets efficiently. In our design this parameter is allowed to vary between 0.7 and 0.8. In the previous chapter, effects of having large ratios of this parameter were mentioned.

Controls described until here were generally related to geometrical design parameters of the proposed generator and can be corrected via adjusting limits of the search space. Hence these can be categorized as search space manipulations. Other than these corrections, there are some other parameters which should be checked if any resulting parameter value of the designed generator violates the safety/necessity margins or not. These kind of parameters are generally named as “constraint” in a optimization process. User/designer can keep this kind of parameters under control by using penalty functions. As described before, penalty functions are used to convert constrained functions to unconstrained functions by assigning additional penalty values, which are relatively large with respect to normal fitness values, to related objective function in the optimization. Hence individuals which are penalized with these penalty functions have large fitness values and then are finally eliminated from successive generations. By this way, optimization changes the search direction to where individuals satisfy all the constraints [12], [96], [99]. Details of the penalty functions and penalty coefficients will be given in the following subsection.

In our design optimization, seven different constraints are included in the objective function via proper penalty functions. Order of these seven penalty functions and related penalty coefficients are given in Table 4-6. These penalty functions are used in the main objective function which was given by Eq. (4-10).

Table 4-6. Objective function penalty table

Penalty Function	Constraint	Penalty Coefficient	Coefficient Value
p_1	Efficiency	$k_{1-1,1-2}$	$k_{1-1}=5 \times 10^4$ $k_{1-2}=3 \times 10^7$
p_2	Deflection	k_2	10^5
p_3	Axial length	k_3	10^5
p_4	Outer diameter	k_4	10^8
p_5	Temperature	k_5	10^5
p_6	Power	$k_{6-1,6-2}$	$k_{6-1}=0.1$ $k_{6-2}=1$
p_7	Voltage	k_7	10^6

These penalty functions are calculated as follows,

- ❖ Efficiency (η) is controlled at every design loops and individuals with efficiency values lower than 95% , are penalized. Efficiency constraint is controlled by the Eq. (4-16) given below.

$$p_1 = \begin{cases} |0.95 - \eta| k_{1-1} & \text{for } \eta < 0.95 \\ 0 & \text{for } 0.95 \leq \eta \leq 0.999 \\ |\eta - 0.999|^2 k_{1-2} & \text{for } \eta > 0.999 \end{cases} \quad (4-16)$$

- ❖ Another constraint is related to C-core deflection ($ratio_{def}$). Due to magnetic attraction forces between magnets, C shaped cores are inclined to be deflected and close the air gap. If this deflection rate with respect to air gap clearance excess 10%, individual which has this much deflected core, is penalized. Ratio of deflection constraint is controlled by the Eq. (4-17) given below.

$$P_2 = \begin{cases} 0 & \text{for } ratio_{def} < 0.10 \\ \left| ratio_{def} - 0.10 \right|^2 k_2 & \text{for } ratio_{def} \geq 0.10 \end{cases} \quad (4-17)$$

- ❖ Another constraint is related to axial length (l_{shaft}) and it's very important. Because one of the salient advantages of proposed AFPM is shorter axial length [31]. For this purpose, individuals who has axial length higher than 5 meters, are penalized. Axial length constraint is controlled by the Eq. (4-18) given below.

$$P_3 = \begin{cases} 0 & \text{for } l_{shaft} < 5 \\ \left| l_{shaft} - 5 \right|^2 k_3 & \text{for } l_{shaft} \geq 5 \end{cases} \quad (4-18)$$

- ❖ Stator outer diameter (d_{out}) is another important parameter of the generator, especially when the nacelle volume is limited. Therefore, individuals with stator outer diameters above 10 meter, are also penalized. Outer diameter constraint is controlled by the Eq. (4-19) given below.

$$P_4 = \begin{cases} 0 & \text{for } d_{out} < 10 \\ \left| d_{out} - 10 \right| k_4 & \text{for } d_{out} \geq 10 \end{cases} \quad (4-19)$$

- ❖ Operating temperature ($\Delta T + T_{ambient}$) is another important design parameter related to efficiency. In this design optimization, individuals which has operating temperature higher than 100° C, are penalized. In addition to temperature constraint, efficiency constraint also guarantees the thermal limits by assigning high efficiency penalties to candidate individuals with high copper losses. Temperature constraint is controlled by the Eq. (4-20) given below.

$$P_5 = \begin{cases} 0 & \text{for } (\Delta T + T_{ambient}) < 100 \\ \left| (\Delta T + T_{ambient}) - 100 \right|^2 k_5 & \text{for } (\Delta T + T_{ambient}) \geq 100 \end{cases} \quad (4-20)$$

- ❖ As mentioned before, in every optimization loop GA algorithm tries to determine the design parameters of the AFPM which gives output power of 5MW at 12 rpm rated speed. For this purpose, designed machine is operated

at every speed interval which defined earlier in Table 4-3 and tries to reach the output power of every specific operating speed reference. Individual which misses these power levels, is penalized with a penalty function. Power constraint is controlled by the Eq. (4-21) given below.

$$p_6 = \begin{cases} |P_{demand} - P_o|^2 k_{6-1} & \text{for } P_o \leq P_{demand} \\ 0 & \text{for } P_o = P_{demand} \\ |P_o - P_{demand}|^2 k_{6-2} & \text{for } P_o > P_{demand} \end{cases} \quad (4-21)$$

- ❖ Final constraint employed in this optimization work is related to electrical rating of the proposed generator. Rms value of the voltage per phase ($V_{ph,rms}$) is kept under controlled via suitable penalty function such that line-to-line rms voltage level can't excess the 690 V, which is a common voltage level among commercial wind turbine generators [104], [105]. Proper voltage level selection is important since the output voltage level which is too high or too low can cause higher power electronic converter costs. Voltage constraint is controlled by the Eq. (4-22) given below.

$$p_7 = \begin{cases} 0 & \text{for } V_{ph,rms} < 400 \\ |V_{ph,rms} - 400|^2 k_7 & \text{for } V_{ph,rms} \geq 400 \end{cases} \quad (4-22)$$

As it can be seen from calculations, response of the penalty functions can be adjusted via penalty coefficients at different order of magnitude and via different measure of violation such as absolute difference or square of the absolute difference. Hence optimization will converge to an area of the search space such that chosen set of independent variables do not violate the constraints. As a result, penalty coefficients are chosen very large to satisfy all the constraints strictly. Therefore, a small violence of any constraint will be penalized with a large fitness value [12].

4.5. Optimized 5MW AFPM Generator

Optimized independent variables of the proposed AFPM generator at rated conditions of 5 MW, 12 rpm, are presented in Table 4-7. Note that optimization algorithm converges to increased number of parallel stack in order to conform

penalty constraints of outer diameter and power level. By this way, amount of permanent magnet is increased. However, this type of parallel stacked configuration gives better fault handling ability to our proposed generator, as it was mentioned in previous chapters. Other design parameters of the optimized AFPM generator can be calculated by using the design equations given in Chapter-3.

Table 4-7. Optimized generator independent variables at 12 rpm/5MW

Parameter	Value
Mean radius- (r_{mean})	4.71 m
Speed	12 rpm
Number of poles- (N_p)	216
Number of parallel stacks- (n_{stack})	6
Outer limb thickness- (t_o)	38 mm
Inner limb thickness- (t_i)	25.3 mm
Steel web thickness- (l_c)	22.4 mm
Number of turns- (N_t)	42
Current density- (J)	2.47 A/mm ²
Number of branch- (N_{branch})	6
Height of the winding- (h_w)	43 mm
Winding thickness/Coil pitch ratio- (α_{pitch})	0.388
Magnet/Steel width ratio- (α_i)	0.76
Fill factor- (k_{fill})	0.69
Height of the magnet- (h_m)	18.8 mm
Length of the magnet- (l_m)	282.7 mm

Best fitness values of the optimization process through the 200 generations are plotted in the graph given in Fig. 4-7. As it can be seen from this figure, best fitness value of the optimization converged to 3.98×10^6 . In the optimization algorithm, every candidate individual is evaluated for nine wind speed conditions. Fitness function is obtained by summing all cost values for these speed conditions. Therefore, it can be said that fitness function itself not obviously shows exact cost

of the proposed generator. Instead, it shows how suitable and low cost solution it becomes throughout the generations. Optimization considers not only initial material cost but also power generation income and selects suitable parameters among the search space. Therefore, more material cost and mass can be preferred for the sake of a better energy generation income.

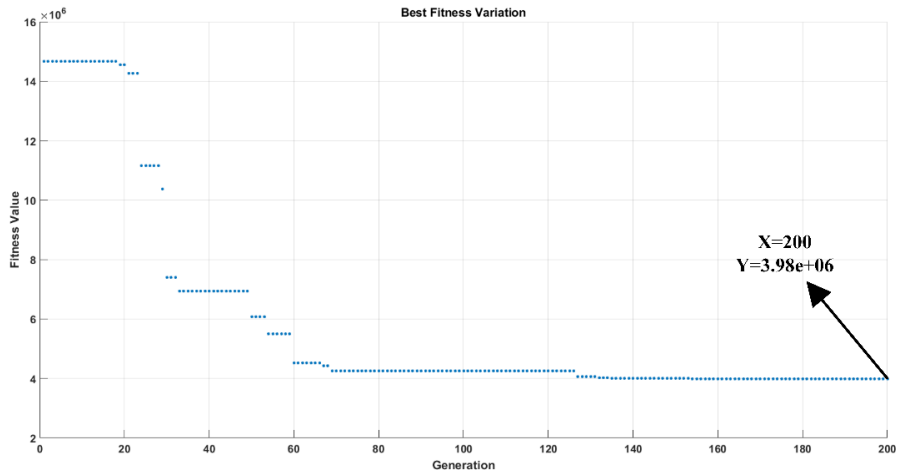


Fig. 4-7. Best fitness variation

Fitness values of all individuals regardless of mean values, are depicted in Fig. 4-8. As it can be seen from this figure, cost of the considered generator showing a decreasing trend as the optimization procedure continues. At the end of the iterations, optimization converged to best fitness value of 3.98×10^6 .

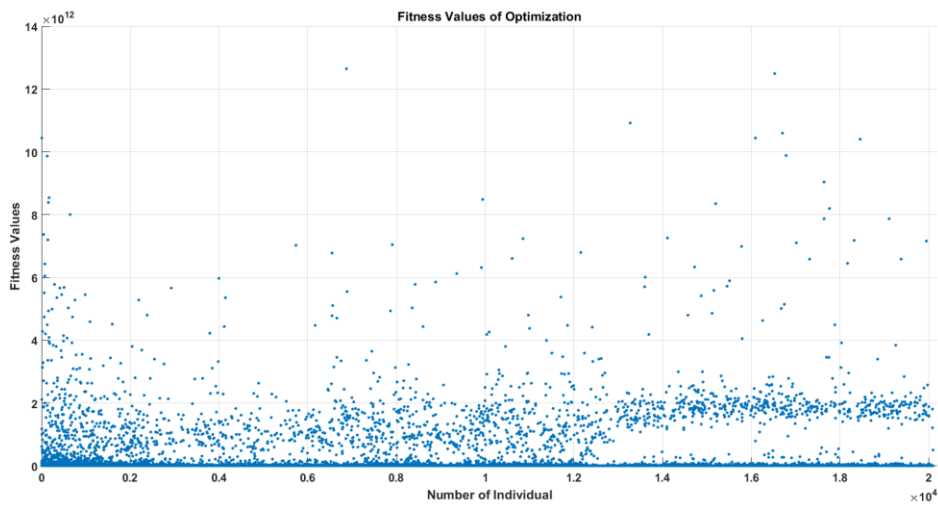


Fig. 4-8. Fitness distribution of the optimization individuals according to iterations

Performance ratings of the optimized generator at different wind speeds are given in Table 4-8.

Table 4-8. Optimized generator performance ratings

Wind Speed	Rpm	J (A/mm ²)	$V_{ph,rms}$ (V)	$I_{ph,rms}$ (A)	Desired Power (kW)	Input Power (kW)	Output Power (kW)	Efficiency (%)
4 m/s	1	1.37	24.4	414.1	195	244	182	74.5
5 m/s	1	2.10	19.5	636.4	420	372	223	60.0
6 m/s	2.9	1.69	84.3	512.0	786	874	777	88.8
7 m/s	4.8	1.62	146.9	489.1	1296	1385	1293	93.4
8 m/s	6.7	1.71	208.0	518.7	1943	2049	1942	94.7
9 m/s	8.6	1.85	268.7	558.3	2699	2829	2700	95.4
10 m/s	10.5	1.95	329.4	588.5	3487	3639	3490	95.8
11 m/s	12	2.03	377.1	615.5	4174	4346	4178	96.1
12 m/s	12	2.47	371.4	746.9	5000	5230	4992	95.4

As it can be seen from performance ratings table above, optimized generator can supply 4.99 MW of electrical output power at 12 rpm, which is only 0.01 MW below the aimed output power of 5 MW with an efficiency of 95%. This small power constraint violation can be neglected since all other constraint parameters are conformed by the optimization. According to optimization results, the most salient

features of the proposed AFPM generator in this thesis is tabulated in Table 4-9. Other details of the design parameters can be found by using mentioned MATLAB scripts which are designed for this thesis work.

Table 4-9. The most salient features of the proposed AFPM generator at 12 rpm

Feature	Value
Mean radius	4.71 m
Stator outer diameter	9.9 m
Rated speed	12 rpm
Air gap	10 mm
Number of poles	216
Number of turns	42
Axial length	1.0 m
Number of axial stack	6
Voltage per phase (rms)	371.88 V
Induced emf per-phase (rms)	395.6 V
Current per phase	746.9 A
Total copper loss	206.9 kW
Total eddy loss	30.1 kW
Net output power	4992 kW
Efficiency	95.4%
Air gap flux density (fundamental-peak)	0.51 T
Air gap flux density (flat-top)	0.46 T
Phase reactance	0.111 Ω
Phase resistance	0.020 Ω
Power factor	1
Load angle	12.17°
Temperature	30.0° C
Shaft outer radius	0.3 m
Shaft inner radius	0.1 m
Total mass	119.4 tonne
Material cost	\$ 1.30 M
Total cost (including labor)	\$ 1.56 M
Total Electricity Generation (annual)	11.73 GWh
Total Generation Income (annual)	\$ 857k

It can be inferred from the table shown above that selected airgap is suitable in terms of resultant air gap diameter and stator outer diameter. Moreover, phase voltage value is reasonable in terms of predetermined limits and practical applications. Total mass per axial stack (119.4/6 tonne) is suitable for modularity and installation, transportation and repair conditions. In Fig. 4-9, whole view of the proposed AFPM generator is given. In this figure structural support parts are not shown.

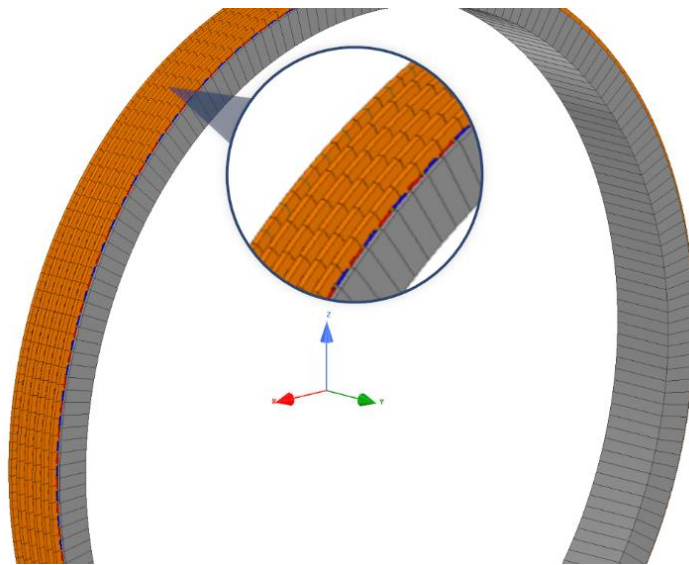


Fig. 4-9. Proposed AFPM generator whole machine view without structural parts

In Fig.4-10, mass components of the optimized 5MW 12 rpm AFPM generator is given. In Fig.4-11, material cost components of the optimized 5MW 12 rpm AFPM generator is given. As it can be seen from graphs, there is not a linear relationship between mass and cost distributions of materials used in the proposed generator. It has been concluded that structural steel mass is the dominant part of the total mass while permanent magnet cost constitutes the dominant part of the total cost of the generator.

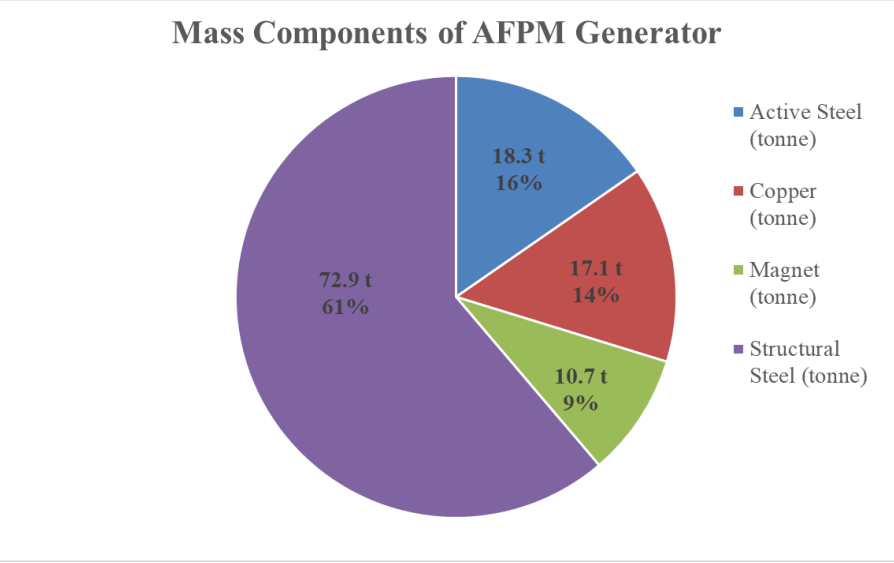


Fig. 4-10. Mass components of the optimized AFPM generator

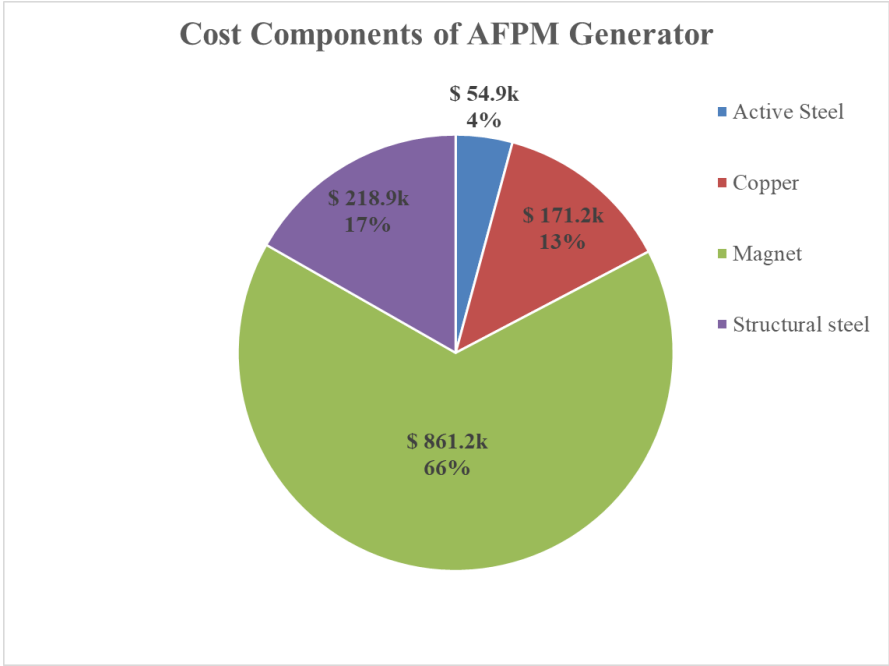


Fig. 4-11. Material cost components of the optimized AFPM generator

4.6. Results

This chapter mainly focused on the optimization procedure and optimized generator parameters. First, general overview of the EA is given including the selected GA optimization. This algorithm is chosen in this thesis work because of its derivative-free approach and application simplicity. In this study, optimization procedure is carried under 9 different wind speed conditions in order to get a more realistic design. Wind speed data is taken from a real field based measurement values of a sample WPP. Algorithm calculated the design parameters of the proposed AFPM generator based on a power generation reference of a commercial 5MW PMSG wind turbine under aforementioned wind conditions. In addition, algorithm also considers the wind speed time probabilistic and related generation incomes. Details of the MATLAB optimization toolbox configurations and used algorithm flowcharts are given in the related subsections.

Seven different penalty functions are used in order to transform our constrained optimization problem to an unconstrained problem. In this study, objective function is constructed based on the cost of the proposed AFPM generator. 15 different independent variables are used in the optimization problem. Air gap is not optimized in this study in order to avoid very large search spaces and long convergence times. Instead, air gap value is taken as constant as 10 mm as it is comply with the conventional machine design practices and production challenges. Axial stack number of the generator is allowed to change during the optimization. Therefore, algorithm converges to best solutions so that resulting generator can be heavier but more cost-effective considering the generation incomes. Details of the constants, independent variables, objective function and penalty functions are given in the related subsections. According to optimization results, most salient features of the proposed AFPM generator in this thesis is tabulated in Table 4-9. Other details of the design parameters can be found by using mentioned MATLAB scripts which are designed for this thesis work.

Details of the reference wind speed table and performance parameters of the proposed AFPM generator under these wind conditions are given in related subsection. Optimized independent variables of the proposed 5MW/12 rpm AFPM

design and fitness evolution tables are presented and discussed. Finally, mass components and material cost components of the proposed generator are investigated. According to results of these components, structural steel is the most dominant (about 61%) mass component while it is the less dominant (about 17%) in terms of material cost. Permanent magnet (PM) is the most dominant (about 66%) cost component while it is the least dominant (about 9%) mass component. Since optimization is based on the cost of the design, algorithm converged to heavier and larger design solution. However, mass of the most expensive component, namely PMs, is minimized. More detailed graphs of mass and cost distributions of the proposed design is given in the related subsections. Optimized parameters are very important because they will be used in the finite element modelling and verification of the proposed generator in the next chapter.

CHAPTER 5

FEA VERIFICATION OF ANALYTICAL DESIGN

5.1. Introduction

In the previous chapter, optimization procedure of the proposed AFPM generator was described and required design parameters were determined and presented by using the genetic algorithm optimization. In this chapter, design parameters of the optimized generator will be used in the 3D FEA modelling and analysis in order to verify the electromagnetic and electrical performance of the proposed AFPM generator. ANSYS Maxwell[®] software is employed for the 3D finite element simulations. As mentioned in Chapter-3, air gap flux density and no-load induced emf values are investigated during the analyses. In addition, full load analysis of the proposed AFPM generator is performed in order to calculate the phase voltages and coefficient of eddy losses on the permanent magnets. Related graphs and simulation results will be given in the following subsections.

5.2. Magnetostatic Analysis

In the finite element computation environment, magnetostatic analyses are done in order to estimate the electromagnetic behaviour of the electromechanical systems under static conditions. Magnetostatic analysis is applied to the proposed generator model in order to calculate the air gap flux density and to observe the flux paths in the machine.

5.2.1. Magnetostatic FEA Configurations

In the modelling stage of the generator in ANSYS Maxwell, 1/54 symmetrical model is employed to minimize the computation time. In Fig. 5-1, mesh plot of the magnetostatic model is given.

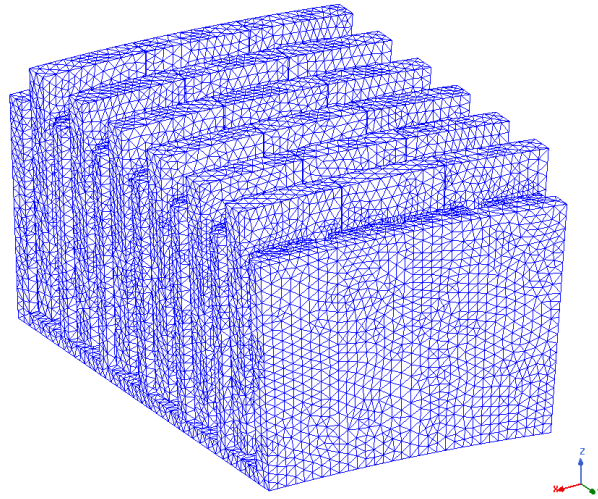


Fig. 5-1. Magnetostatic model mesh plot

Magnetostatic analysis setup configurations and mesh size configurations are given in Table 5-1.

Table 5-1. Magnetostatic FEA configurations

Property	Value
Maximum Mesh size	25 mm
Error	0.5 %
Maximum number of passes	15
Refinement Per Pass	30%

5.2.2. Air gap Flux Density Verification

In this section, air gap flux density value of the proposed generator is investigated and compared with the analytically calculated air gap flux density value in order to verify the proposed 5MW 12 rpm design. For this purpose, three different lines are drawn between the middle of the magnets exist on the C-shaped cores. Therefore, air gap flux density variation can be observed. In Fig. 5-2 and Fig. 5-3, these air gap measurement lines are shown from side and top view, respectively.

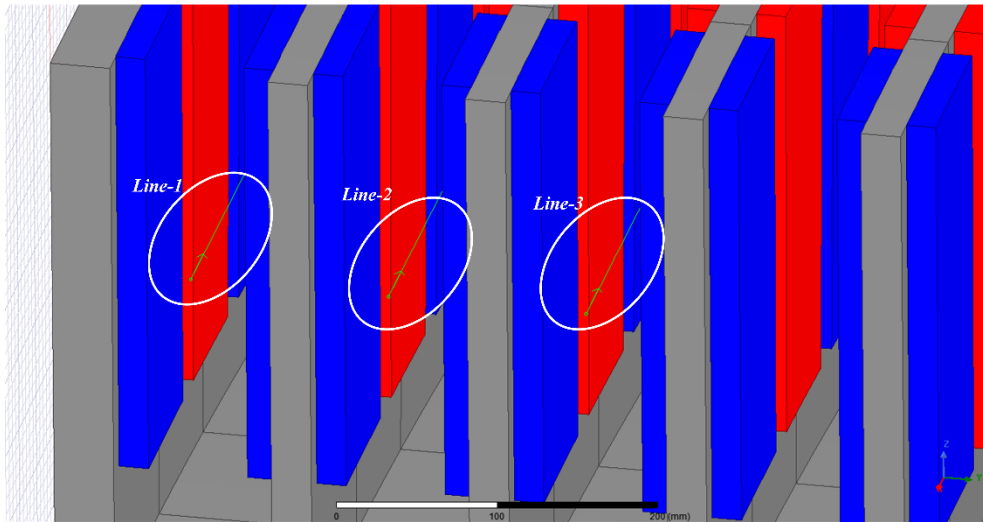


Fig. 5-2. Air gap flux density measurement lines side view

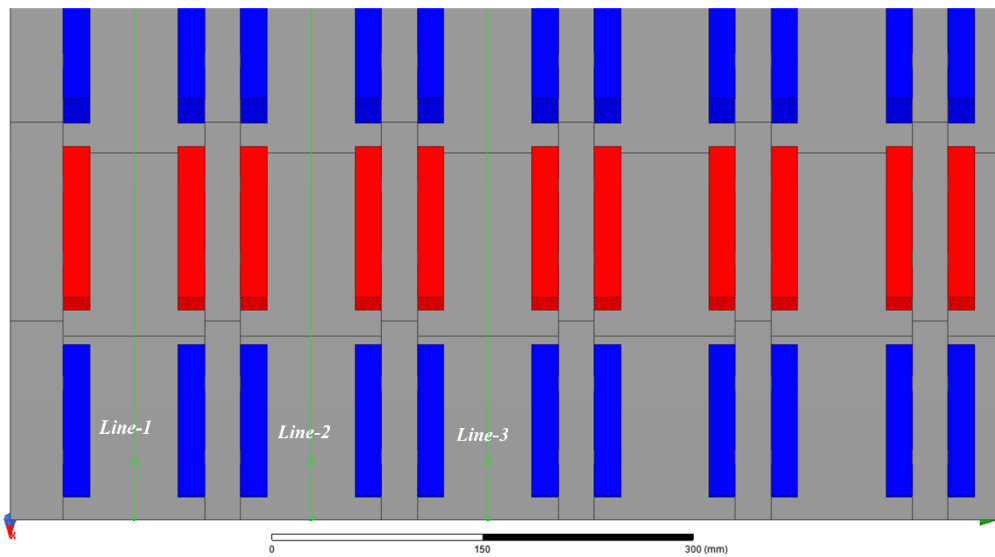


Fig. 5-3. Air gap flux density measurement lines top view

In Fig. 5-4, air gap flux density values with respect to related position in the flux density measurement line-1, line-2 and line-3 are shown, respectively. As it can be seen from the graphs, these waveforms show sinusoidal variation with peak fundamental magnitude of 0.502 T.

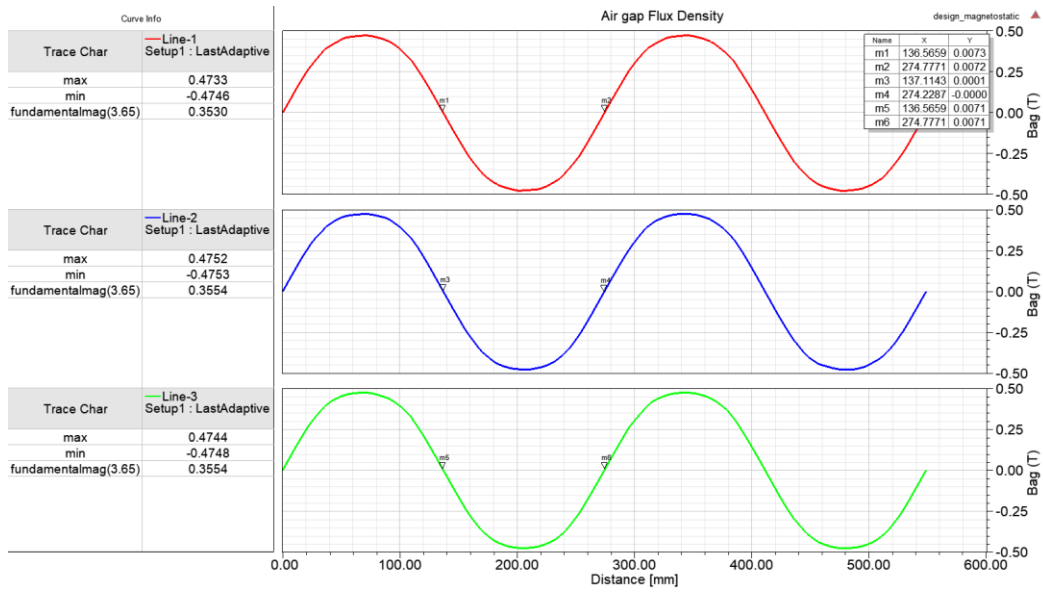


Fig. 5-4. Air gap flux density graph from FEA

In Fig. 5-5, top view of the flux density vectors is shown around the poles and air gaps. As it can be seen on this graph, there exist leakage fluxes at the edge of the magnets.

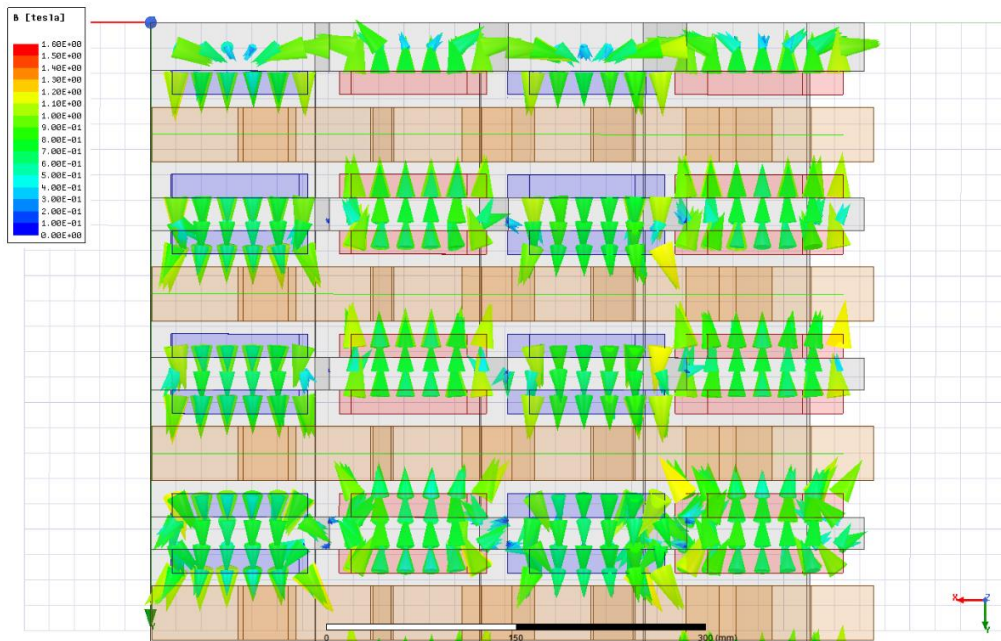


Fig. 5-5. Airgap flux density vectors for the 5 MW design

In order to observe the sinusoidal variation of the flux density plots, a virtual sheet is drawn in the middle of the airgap region. Flux vectors are depicted in Fig. 5-6 and Fig. 5-7 from the side and top view, respectively.

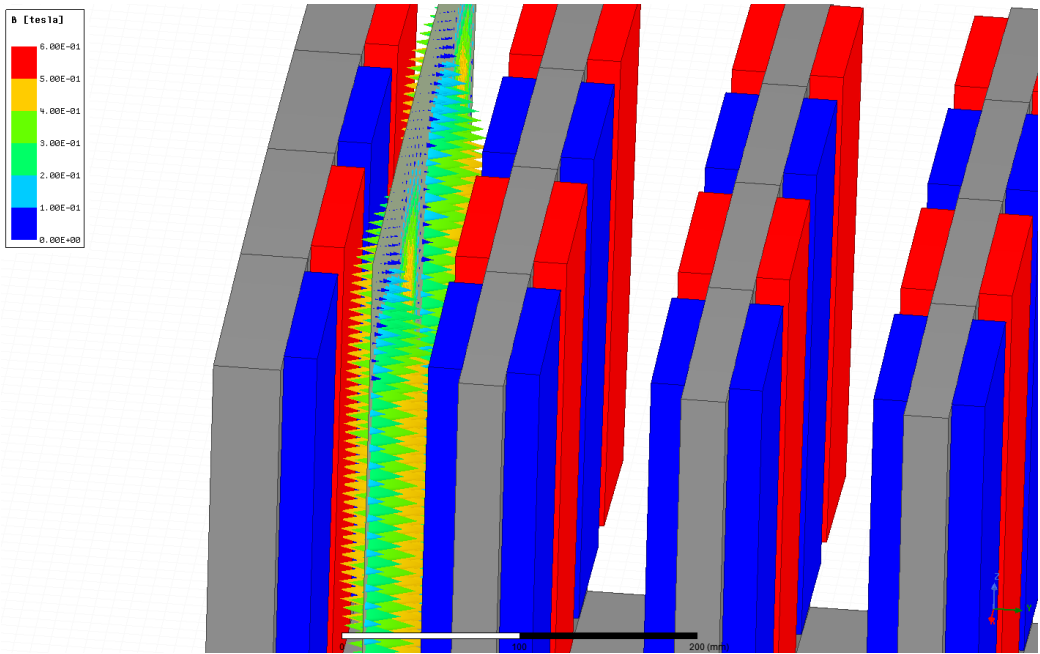


Fig. 5-6. Airgap flux density vectors on the virtual sheet (side view)

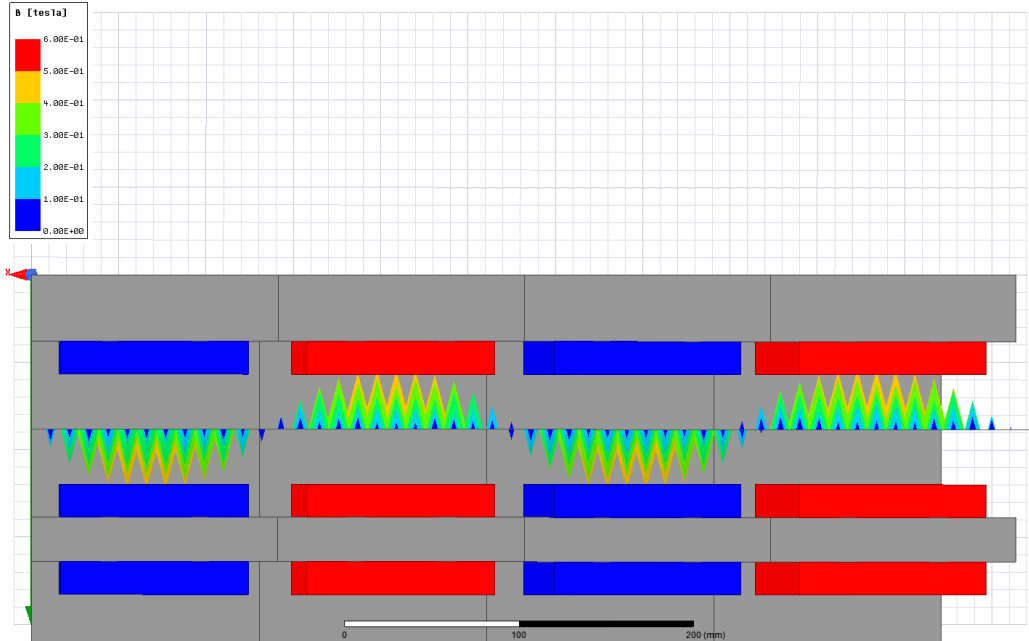


Fig. 5-7. Airgap flux density vectors on the virtual sheet (top view)

In Fig. 5-8, flux density magnitude distribution over the steel core parts is shown.

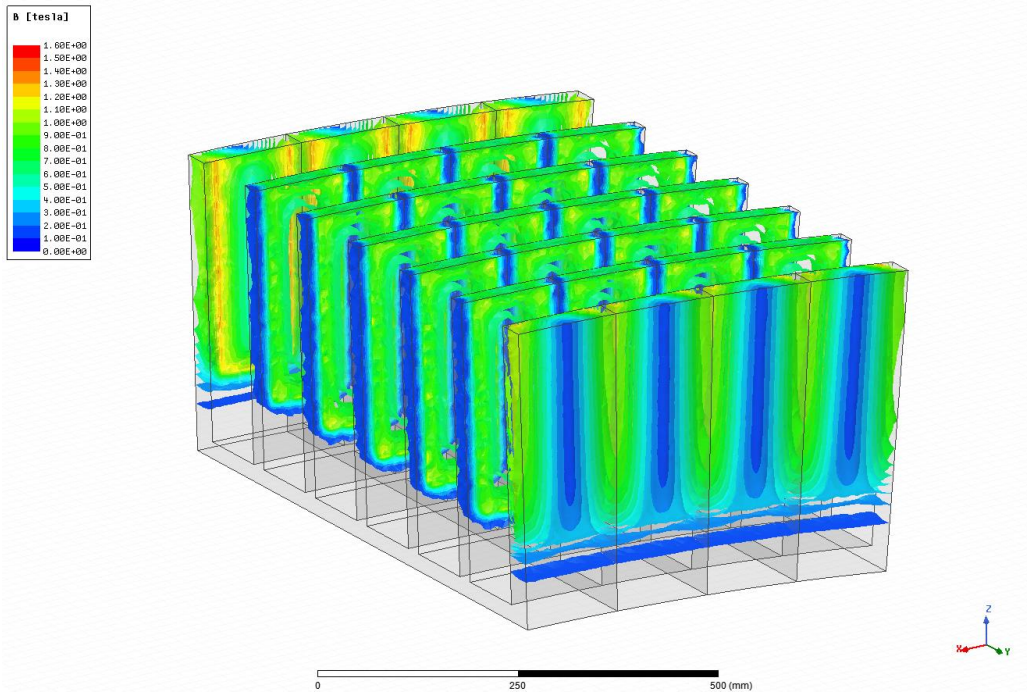


Fig. 5-8. Flux density magnitude distribution over the steel cores of the design

In Fig. 5-9, flux density magnitude distribution over the virtual sheet is shown. As it shown on graph, flux density magnitude values are consistent with the flux density plot magnitudes given in Fig. 5-4.

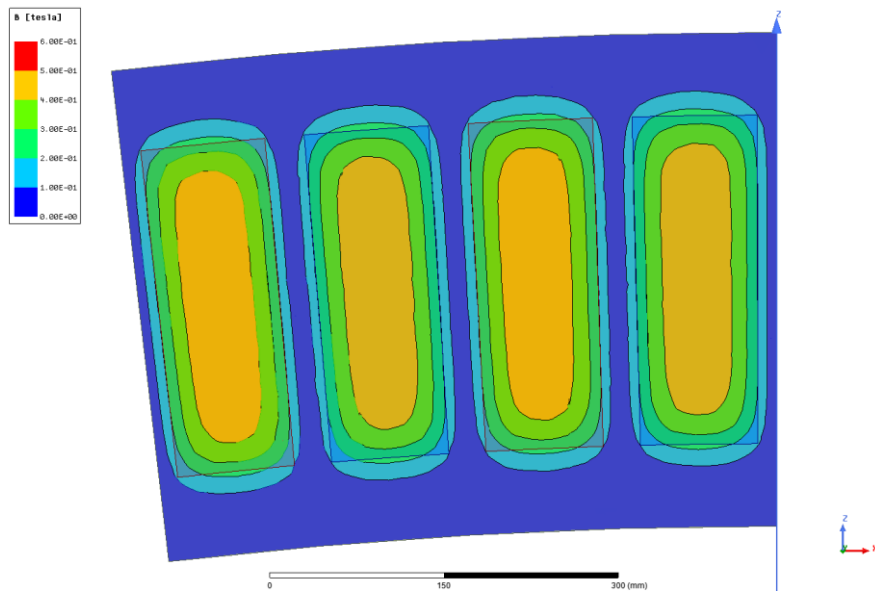


Fig. 5-9. Flux density magnitude distribution over the virtual sheet

According to these FEA results, air gap flux density characteristics of the proposed design and comparison with analytical calculation results are summarized in Table 5-2. In Fig. 5-10, variation of the air gap flux density together with analytical and FEA results are shown. Black labeled flux density is the analytically calculated flux density value with a flat-top value of 0.459 T while red and blue labels show the analytically calculated fundamental harmonic peak air gap flux density and FEA results, respectively. As it was mentioned in the Chapter-3, peak value of the fundamental component of the flux density value is calculated according formula given below,

$$B_{ag,1} = \frac{4}{\pi} B_{ag} \sin(\alpha_i \frac{\pi}{2}) \quad (5-1)$$

Table 5-2. Comparison of the analytical and FEA results for the air gap flux density

Property	FEA	Analytical	Error
Air gap flux density - (peak)	0.474 T	0.459 (flat-top) T	3.1%
Air gap flux density fundamental- (peak)	0.502 T	0.516 T	2.7%

As mentioned in the previous chapters, air gap flux density value is a critical value that has to be verified. It can be seen from the Table 5-2 and Fig.5-3 that analytically calculated values and finite element analysis results of the air gap flux density of proposed AFPM generator are in good agreement and related error values are around 3% . Small difference between FEA results and analytically calculated flux density is due to leakage fluxes that are not included in the analytical method of this study.

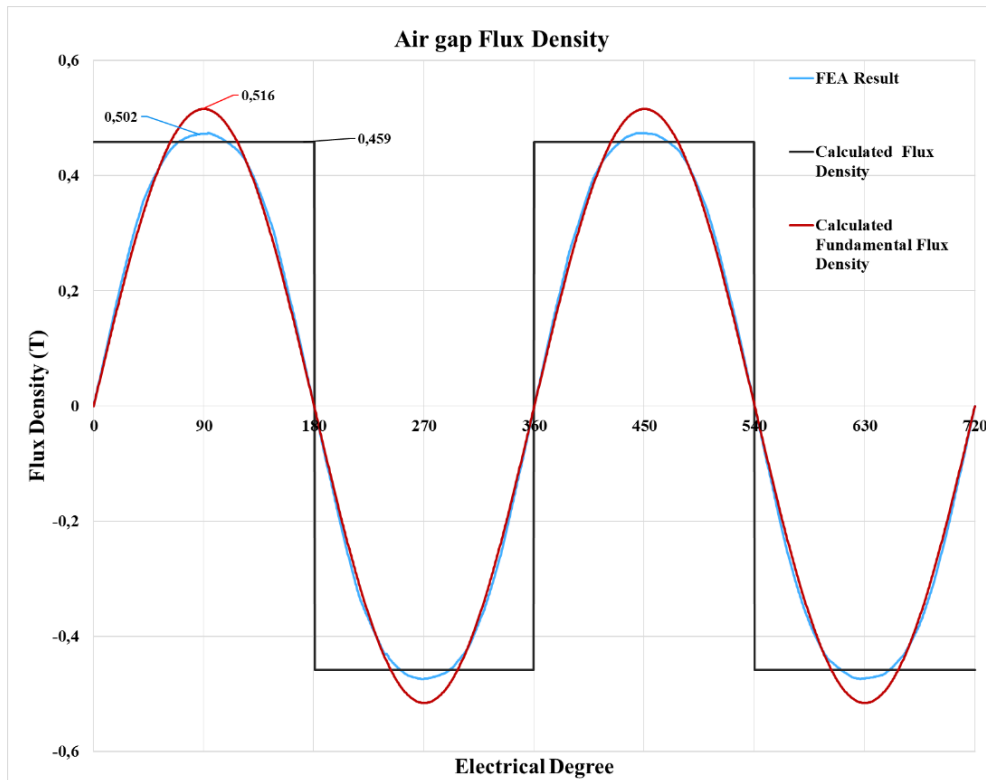


Fig. 5-10. Airgap flux density graph with analytical results for the 5 MW design

5.3. Transient Analysis

In the transient finite element environment, analyses are done in order to estimate the electromagnetic performances of the electromechanical systems under dynamic conditions. Three main objectives of the transient FEA analyses can be listed as; no-load induced emf, full-load phase voltage and full-load eddy loss coefficient estimation.

5.3.1. Transient FEA Configurations

In the transient model, two different mesh sizes are used in order to avoid computational burden of simulation. Configurations of the transient FEA are given below in Table 5-3.

Table 5-3. Transient FEA configurations

Property	Value
Mesh size (no-load)	25 mm
Mesh size (full-load)	30 mm
Time step	1 ms
Stop time	0.1 s
Speed	12 rpm (rated)

5.3.2. No-load Model

In this section, only induced emf of the proposed AFPM generator will be investigated under no-load conditions. For this purpose, zero current value is assigned to three phase windings together with infinitely high resistance values.

a) Induced EMF Verification

Induced EMF E_a is the voltage measured across open phase windings when no current flows through and machine rotates at rated speed of 12 rpm. In Fig. 5-11, circuit schematic of the machine is presented. In Fig. 5-12, induced emf graph from the finite element analysis is given. According to this figure, induced emf per phase rms value is measured as 394.5 V.

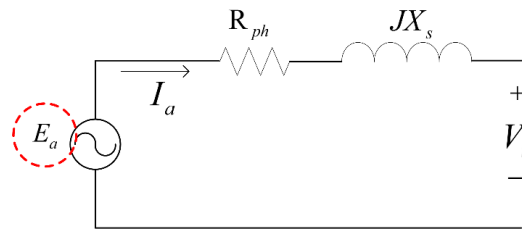


Fig. 5-11. FEA induced emf (E_a) measurement equivalent circuit

Comparison of the analytical results with FEA results for the induced emf per phase is given in Table 5-4 below. As it can be seen from this table, error is 0.27%. Therefore, analytical design method is verified with FEA in terms of induced emf

values. Main reason of difference between errors of flux density and induced emf is the leakage flux coefficient (k_{leak}) used in flux linkage calculations as presented in Eq. 3-42 in the Chapter-3. This coefficient is used in this thesis to compensate the effect of not included air gap leakage fluxes. Therefore, analytically calculated air gap flux density value, which is higher than the FEA flux density result, intentionally multiplied by this predetermined coefficient. Value of this coefficient is determined as 0.95 according to several analyses of FEA induced voltage values before the final design simulation.

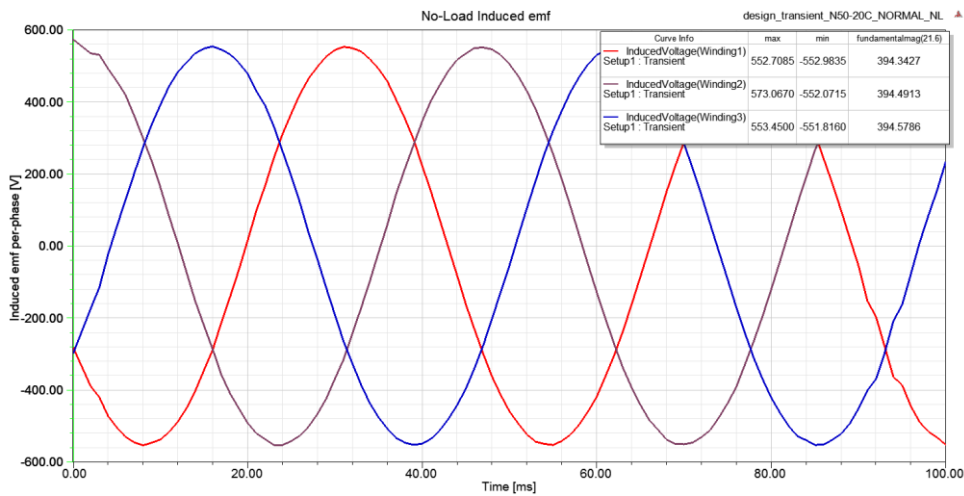


Fig. 5-12. Proposed design induced emf per phase results from FEA

Table 5-4. Comparison of the analytical and FEA results for the induced emf per-phase

Property	FEA Value (V)	Analytical Value (V)	Error
Induced emf per-phase rms (E_a - rms)	394.5	395.6	0.27%

In the optimization stage, 400 V phase voltage convention was selected due to commercial applications and candidate individuals with phase voltage level above 400 V, are penalized. However, there is no lower phase voltage limit value for the penalty. Therefore, optimization converged to not exactly 400 V but very close value

to it. Although there will be a small voltage drop because of the phase impedance in the full-load, FEA induced EMF voltage level is consistent with the selected voltage level target.

5.3.3. Full-load Model

In this section, phase voltages and value of the magnet eddy loss coefficient will be investigated under full-load conditions and related verifications will be presented. For this purpose, three phase windings of the proposed AFPM generator are excited by using rms phase current value which was determined in the previous chapter. During the excitation, load angle which was determined in the previous chapter is added to these excitation equations in order to achieve “in phase” current and voltage waveforms, i.e. unity power factor as it is assumed.

a) Phase Voltage Verification

As mentioned in the previous subsection, phase windings are excited so that current and voltage waveforms are in phase and unity power factor condition is obtained as shown in Fig.5-13.

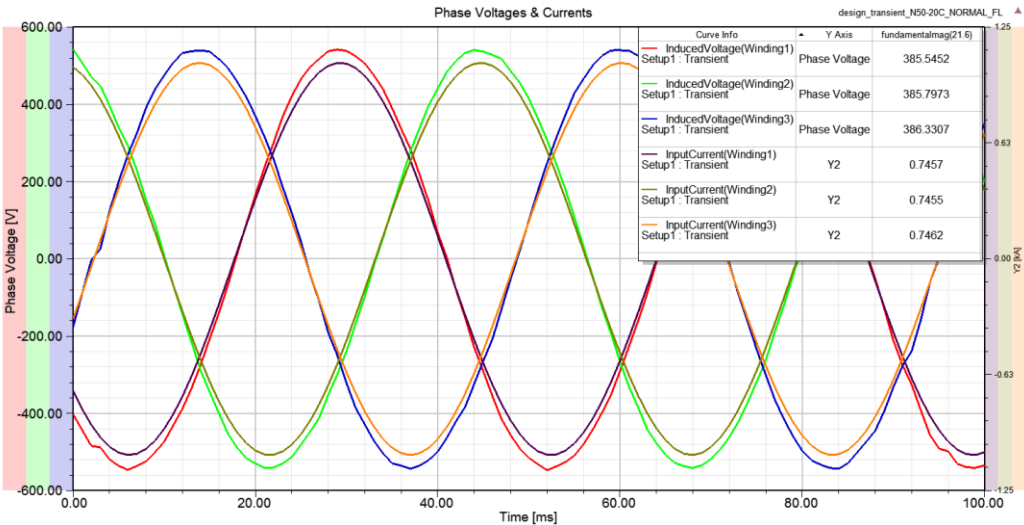


Fig. 5-13. Full-load phase voltages and currents

Although in Chapter-3 phase resistance is omitted when drawing the approximately equivalent circuit and related phasor diagrams, in analytical calculations of this thesis study phase resistance values are taken into account. Therefore, equivalent

circuit given in Fig. 5-11 is used when calculating the phase voltage of the proposed AFPM generator. According to this equivalent circuit, phasor diagram of the proposed design and phase (terminal) voltage equation are given in Fig. 5-14 and Eq. 5-2, respectively.

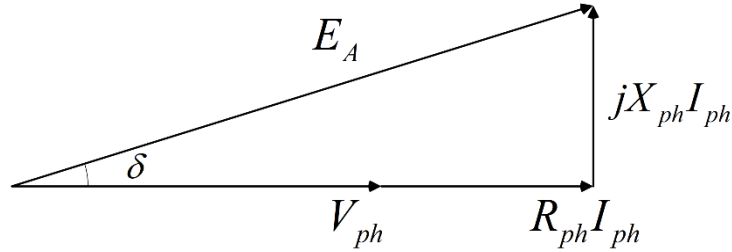


Fig. 5-14. Proposed design phasor diagram including resistance

$$\vec{V}_{ph} = \vec{E}_A - \vec{I}_{ph}(\mathbf{R}_{ph} + jX_{ph}) \quad (5-2)$$

However, Maxwell FEA does not include the resistance into calculation. Therefore, resistive voltage drop should be subtracted from the rms phase voltage value calculated by FEA. This resistive voltage drop can be easily calculated by using the phase resistance (R_{phase_th}) value which was determined in the previous chapter as 0.02 ohm(Ω). Phase reactance X_{ph} of the FEA can be found as follows,

$$X_{ph,FEA} = j\omega L_{phase,FEA} \quad (5-3)$$

Phase inductance value from FEA $L_{phase,FEA}$ is measured as 1.04 mH while analytical design method calculated it as 0.82 mH as it was mentioned in the Chapter-4. Therefore, phase reactance of the FEA can be estimated as follows,

$$X_{ph,FEA} = (2\pi f)L_{phase,FEA} = 2\pi(21.6Hz)(1.04mH) = 0.141 \Omega \quad (5-4)$$

As it can be seen from the Fig. 5-13, rms phase voltage without resistive drop is measured as 385.6 V from FEA. Current and resistance values used in calculations are taken from analytical design results in the previous chapters. Load angle of FEA is found by using geometrical relations according to phasor diagram given in Fig.5-14 and its value is calculated as 15.48° degree. Resulting phase voltage obtained by FEA is calculated according to Eq. (5-1) as follows,

$$\overrightarrow{V_{ph,FEA}} = 394.5 \angle 15.48^\circ - 746.9(0.02 + j0.141) \quad (5-5)$$

$$V_{ph,FEA} = 365.25 \angle 0^\circ \text{ V}$$

Comparison of the analytically calculated results with FEA results for the phase voltage is given in Table 5-5 below. As it can be seen from this table, error rate is 1.81%. Since the proposed generator has an air-cored structure, inductance values are very low and the inductance effect on the resulting phase voltage are very low. Moreover, generator operates at low frequencies, phase reactance values do not become dominant in the calculation of the phase voltage. Therefore, analytical design method is verified with FEA in terms of phase voltage values.

Table 5-5. Comparison of the analytical and FEA results for the phase voltage

Property	FEA Value (V)	Analytical Value (V)	Error
Phase voltage	365.25	371.88	1.81%

In addition to comparison with the analytically calculated results, phase voltage waveforms obtained from FEA are subjected to FFT by using MATLAB/Simulink environment in order to see the harmonic content and THD value. For this purpose, phase voltage waveforms are exported to Excel data file which contains the 100 ms duration of phase windings voltage waveforms, which approximately last 2 cycles. Then this waveform data is utilized by the simulation file generated by the Simulink in order to implement FFT analysis. In Fig. 5-15 exported phase voltage waveforms are presented.

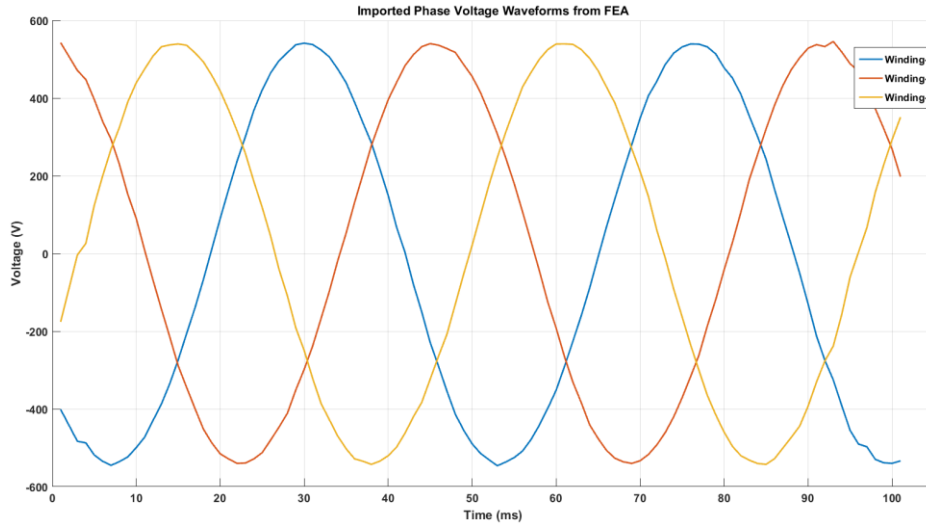


Fig. 5-15. Phase voltage waveforms imported from FEA to Simulink

Imported phase voltage data then subjected to Fast Fourier Transform (FFT) to analyze the harmonic content and Total Harmonic Distortion (THD) is estimated around 2% for three windings. In Fig. 5-16, a screenshot of the simulation block created in Simulink is presented. Workspace data fetch blocks “m1”, “m2” and “m3” are corresponding to “phase winding-1” , “phase winding-2” and “phase winding-3” voltage data, respectively. In Fig. 5-17, Fig. 5-18 and Fig. 5-19, harmonic components of the phase voltage waveforms and corresponding THD values are presented. Frequency of the fundamental harmonic component of the voltage waveform is equal to 21.6 Hz, as mentioned in the previous sections.

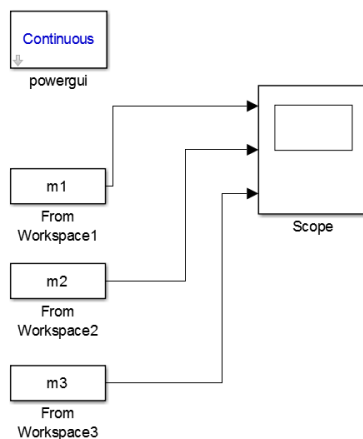


Fig. 5-16. Simulation block in MATLAB/Simulink

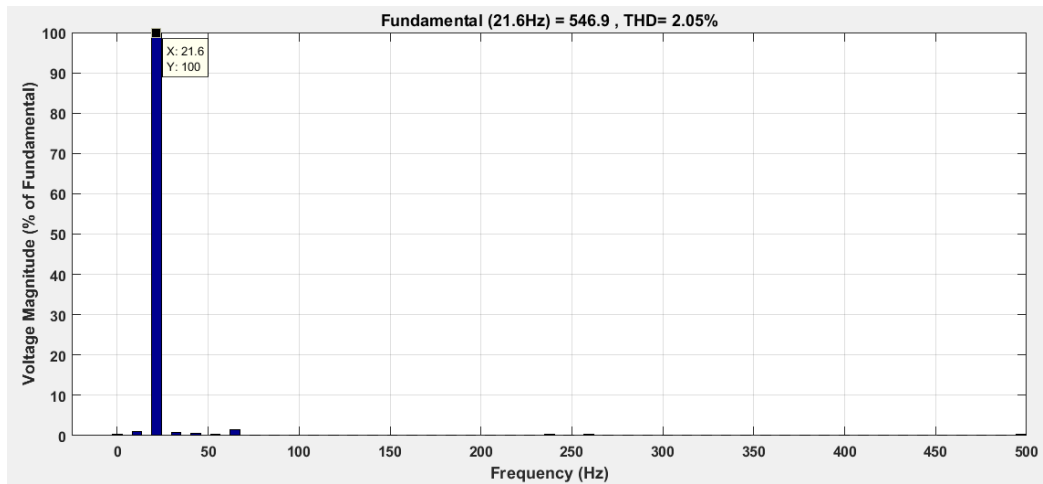


Fig. 5-17. Harmonic component magnitudes and THD for winding-1 voltage

In Table 5-6; frequency, magnitude and percentage magnitude of the fundamental component information of the first 10 voltage harmonics of the Winding-1 are presented.

Table 5-6. Properties of the first 10 voltage harmonics of winding-1

Winding	Harmonic No	Frequency (Hz)	Magnitude	% of Fund. Mag.
Winding-1	1 st (Fundamental)	21.6	546.93	100 %
	2 nd	43.2	2.65	0.48 %
	3 rd	64.8	8.19	1.50 %
	4 th	86.4	0.82	0.15 %
	5 th	108	0.97	0.18 %
	6 th	129.6	0.57	0.10 %
	7 th	151.2	1.17	0.21 %
	8 th	172.8	0.58	0.11 %
	9 th	194.4	1.17	0.21 %
	10 th	216	1.10	0.20 %

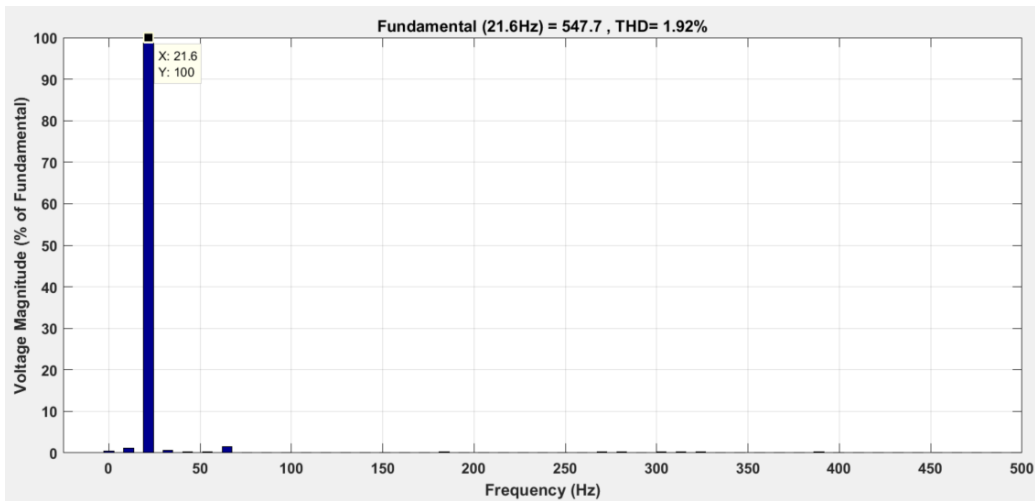


Fig. 5-18. Harmonic component magnitudes and THD for winding-2 voltage

In Table 5-7; frequency, magnitude and percentage magnitude of the fundamental component information of the first 10 voltage harmonics of the Winding-2 are presented.

Table 5-7. Properties of the first 10 voltage harmonics of winding-2

Winding	Harmonic No	Frequency (Hz)	Magnitude	% of Fund. Mag.
Winding-2	1 st (Fundamental)	21.6	547.67	100 %
	2 nd	43.2	1.30	0.24 %
	3 rd	64.8	8.53	1.56 %
	4 th	86.4	0.26	0.05 %
	5 th	108	0.61	0.11 %
	6 th	129.6	0.50	0.09 %
	7 th	151.2	0.71	0.13 %
	8 th	172.8	0.48	0.09 %
	9 th	194.4	0.90	0.16 %
	10 th	216	0.55	0.10 %

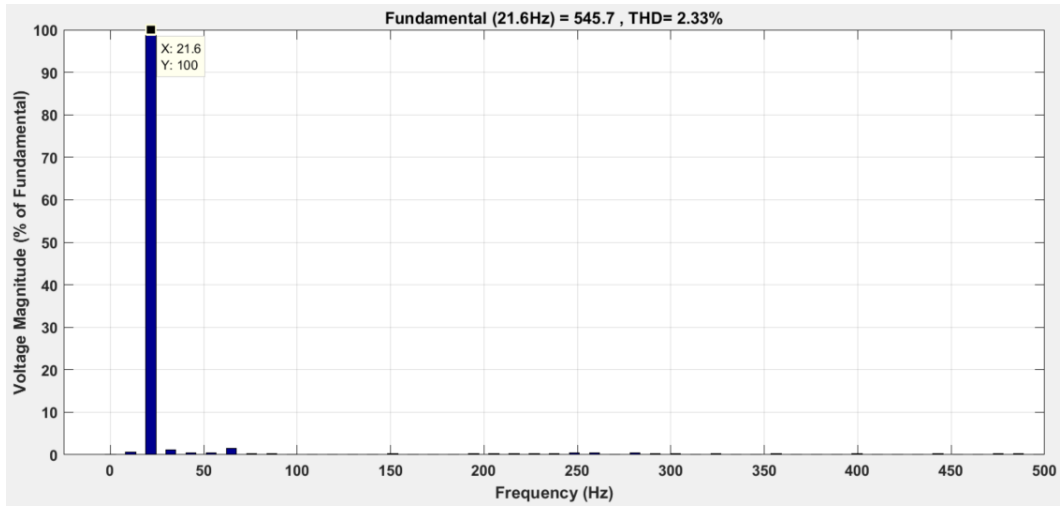


Fig. 5-19. Harmonic component magnitudes and THD for winding-3 voltage

In Table 5-8; frequency, magnitude and percentage magnitude of the fundamental component information of the first 10 voltage harmonics of the Winding-3 are presented.

Table 5-8. Properties of the first 10 voltage harmonics of winding-3

Winding	Harmonic No	Frequency (Hz)	Magnitude	% of Fund. Mag.
Winding-3	1 st (Fundamental)	21.6	545.72	100 %
	2 nd	43.2	2.85	0.52 %
	3 rd	64.8	7.96	1.46 %
	4 th	86.4	1.10	0.20 %
	5 th	108	0.90	0.16 %
	6 th	129.6	0.19	0.03 %
	7 th	151.2	1.25	0.23 %
	8 th	172.8	0.31	0.06 %
	9 th	194.4	1.12	0.21 %
	10 th	216	1.37	0.25 %

As it can be seen from the graphs and tables, harmonic content of the voltage waveforms are normal and THD values for all the three windings are calculated as around 2%. Generated phase voltages of the generator will be utilized in the power electronic converter before the grid connection. Therefore, it's important to supply low-harmonic content voltage at the output of the generator windings in terms of converter losses. Since IEEE Std 519-2014 (Standard for Harmonic Control in Power Systems) recommends maximum THD of 8% at PCC for bus voltages below 1 kV, calculated voltage THD of 2% for proposed AFPM generator design can be evaluated as consistent.

b) Eddy Loss Coefficient Estimation

In analytical calculations part of our proposed design method, eddy current losses on the magnets are taken into account. For this calculation, a coefficient of this loss per unit volume of the magnet is estimated by using FEA simulations for the rated frequency of 21.6 Hz. Coefficient of this loss then used in the analytical calculations fractional to operating speed since eddy losses are dependent to square of the frequency.

In the stage of FEA evaluations, following equation is employed during the generation of FEA calculation for eddy losses for one unit of PM block [87], [88].

$$\int_{V_{magnet}} \frac{J_{eddy}^2}{\sigma_{magnet}} \quad (5-6)$$

FEA integrates the expression above in one whole PM volume where J_{eddy} is the eddy current density and σ_{magnet} is the electrical conductivity of PM, respectively. Conductivity value is taken constant as 5.55×10^5 S/m. In the FEA, first integral value is calculated and then result is divided by the conductance of PM as aforementioned above. In the Fig. 5-20, resultant eddy loss value per one block of PM is presented as 9.97 W/block. In Fig. 5-21, eddy current density vectors on one PM block is depicted.

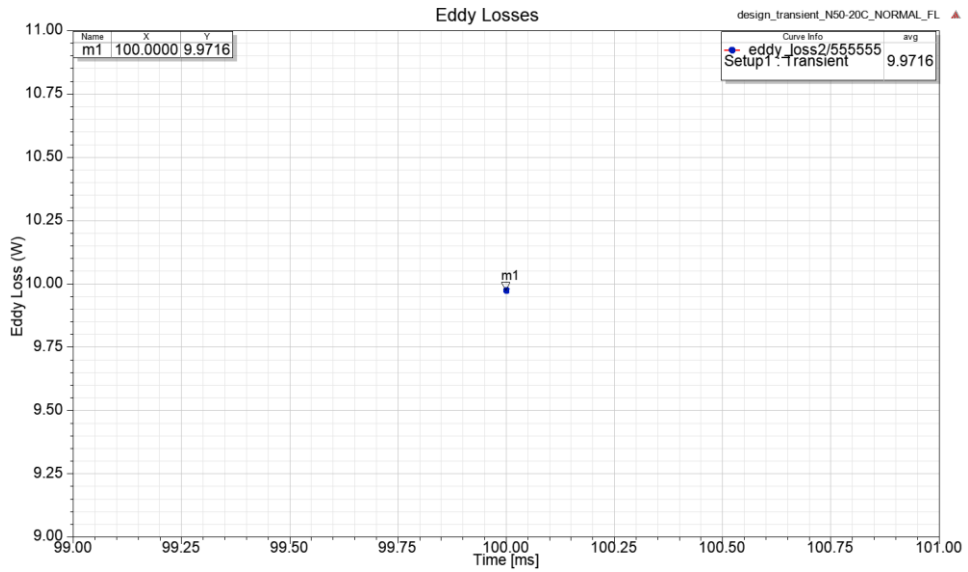


Fig. 5-20. Eddy loss calculated for the one block unit of PM in FEA

Total eddy loss on the magnets at rated frequency of 21.6 Hz (for 12 rpm) can be calculated by using this eddy loss per magnet block value as follows,

$$\text{Magnet eddy loss} = (9.97) \times (216) \times (2) \times (6) = 25.85 \text{ kW} \quad (5-7)$$

This power loss equals to 0.51% of the total power output of 5 MW. Resulting eddy loss coefficient for per unit volume of PM is calculated as follows,

$$\frac{\text{Eddy loss of one PM block (W)}}{\text{Volume of one PM block (m}^3\text{)}} = \frac{9.97 \text{ W}}{5.53 \times 10^{-6} \text{ m}^3} = 18 \text{ kW/m}^3 \quad (5-8)$$

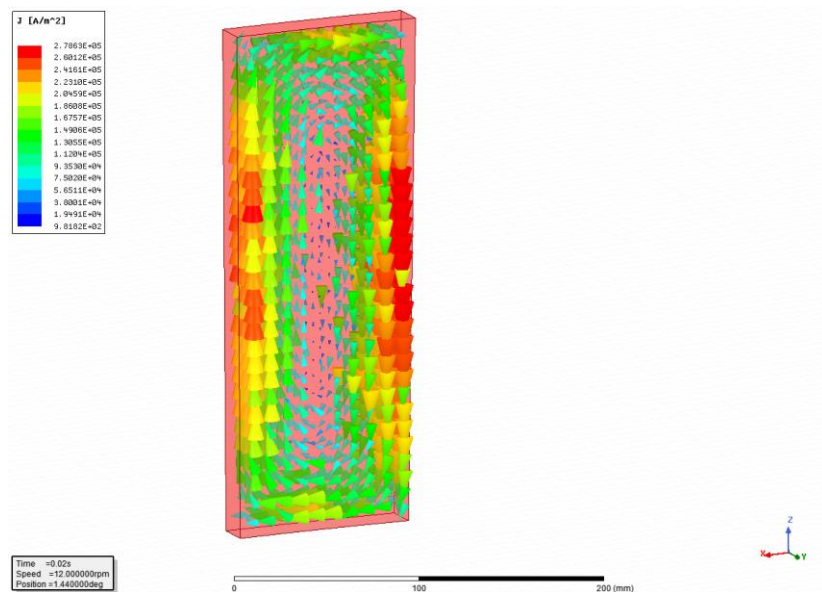


Fig. 5-21. Eddy current density vectors on magnet block

c) PM Demagnetization

PMs used in electrical machines can be demagnetized and hence degrade their field density due to strong magnetic fields applied externally [106], [107]. Such strong fields may be result from the short circuit faults in the generator windings. In this section, demagnetization risk of the N50 grade PMs used in the proposed generator is investigated. In order to do this, three phase short circuit fault is simulated by using FEA and magnetic field intensity values on a block of magnet are compared with B-H curve of the selected N50 grade permanent magnet material. An illustration of three phase short circuit fault on circuit schematic of the proposed AFPM generator is given in Fig. 5-22.

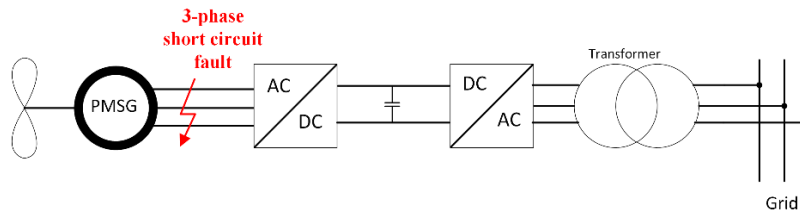


Fig. 5-22. Three phase short circuit fault schematic representation for the proposed system

In Fig. 5-23, B-H curve of the selected N50 grade NdFeB permanent magnet is presented. As it can be seen from this figure as the operating temperature increases, withstand ability (magnitude of the coercive force) of magnet material decreases.

In the FEA simulations, field intensity H (kA/m) is recorded along a line drawn on a PM magnet block during a three phase short circuit fault condition. Simulation is evaluated for 100 ms with 1 ms step size and magnitudes of H aforementioned above are recorded and depicted for every 10 ms periods. Short circuit current waveforms and magnitudes of H plots are given in Fig. 5-24 and Fig. 5-25, respectively.

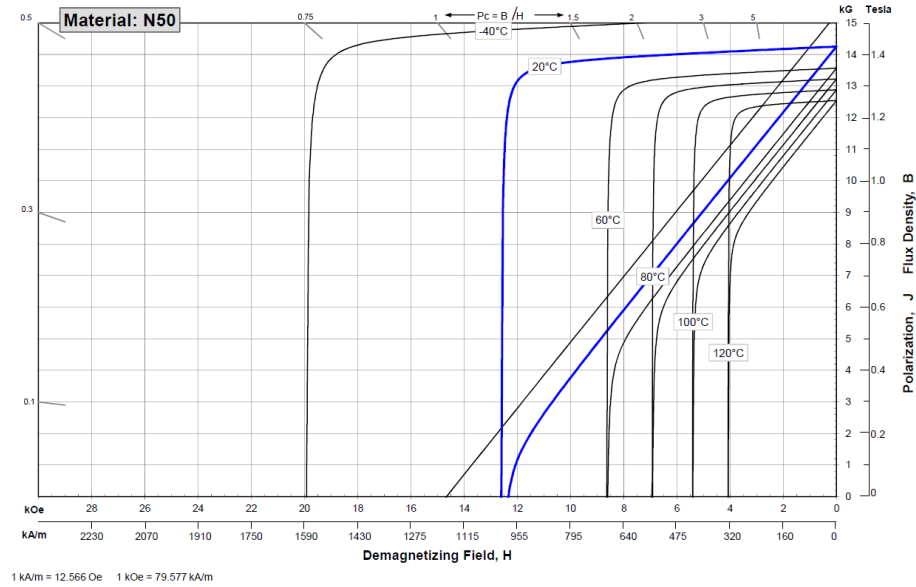


Fig. 5-23. Demagnetization curve of the selected N50 grade PM [78]

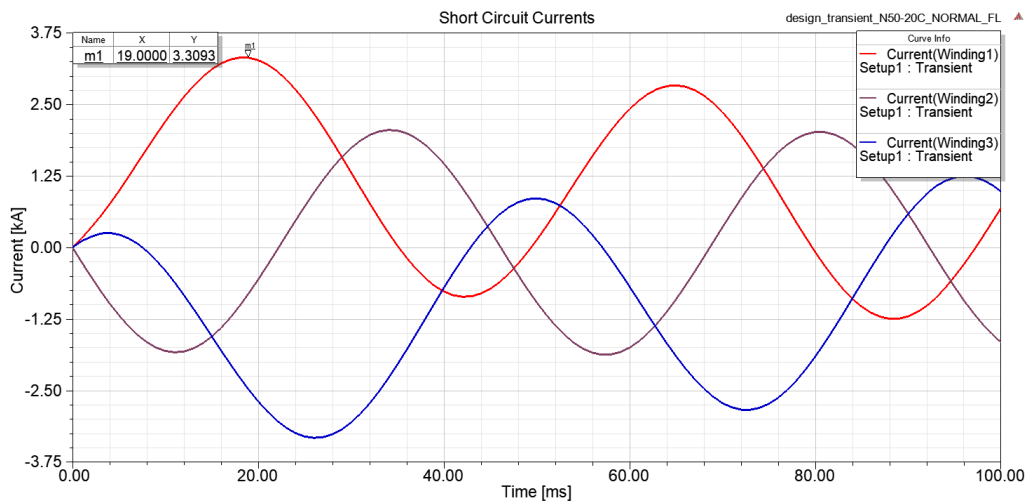


Fig. 5-24. Three phase short circuit current waveforms

According to intrinsic coercivity values given Fig. 5-23 and field intensity values (around 600-850 kA/m) on the magnet block under three phase fault conditions as given in Fig. 5-25, it can be concluded that PMs of the proposed AFPM generator can be demagnetized in case of three phase short circuit faults occur between 20° C – 60° C. Since the inductance of the proposed design is 1.04 mH due to nature of selected air-cored topology, short circuit currents under a faulty condition becomes

3.3 kA as shown in Fig. 5-24. Therefore, there is a risk of demagnetization for the selected N50 grade PMs in the proposed design.

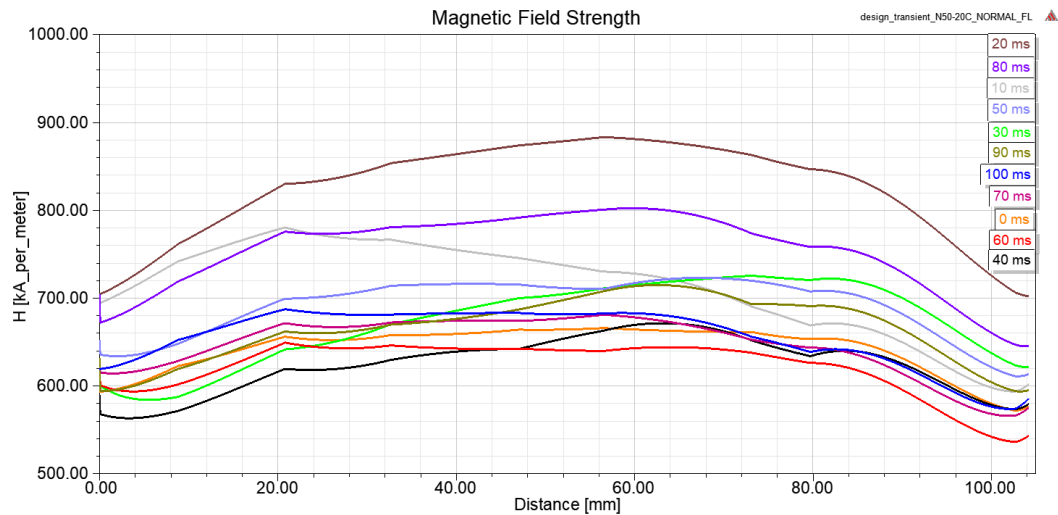


Fig. 5-25. H field intensities under three phase short circuit condition in FEA

5.4. Conclusion

In this chapter, FEA verification is made for the proposed AFPM generator. For this purpose, analytical design parameters, which were calculated in the previous chapters, of the proposed generator are used to model and analyse the performance of AFPM generator in ANSYS Maxwell 3D environment. Magnetostatic and transient analyses are performed for air gap flux density and phase voltage values.

In the magnetostatic simulations of FEA, sinusoidal variation of the air gap flux density is shown for the three different axial stacks of the machine. For these flux density waveforms, analytical result of the air gap flux density is verified by the error rate of 2.7%.

In the transient simulations of FEA, no-load and full load models of the proposed AFPM generator are investigated. For the no-load induced emf, voltage waveforms of the windings under rated speed (12 rpm) condition are depicted and analytical result is verified by the error rate of 0.27%. For the full-load phase voltage simulation, windings are excited by the currents which are calculated analytically in

the previous chapter. In the phase voltage calculation of the FEA, firstly phase inductance value is calculated by the simulations as 1.04 mH while analytically calculated phase inductance is 0.82 mH. Then phase reactance value of the FEA is calculated as 0.141 ohm while this value is calculated analytically 0.111. Phase resistance value is taken from analytical calculations in the previous chapters. Since the proposed machine has an air cored structure and operates at very low rated frequencies, difference of the inductance values does not affected the resultant phase voltage of the FEA markedly. Resultant phase voltage of the FEA model is calculated as 365.25 V and verified by the error rate of 1.81%. In addition to this verification, phase voltages of the FEA are subjected to FFT in order to see the harmonic content in the MATLAB/Simulink environment. THD value of the phase voltages are calculated as approximately 2%, which supports the harmonic content control standards. Related drawings of the harmonic components can be found in the related sub-section.

In the last part of this chapter, coefficient of the eddy loss on the magnets is investigated. For this purpose, volume integration is made in the FEA by using eddy current density, volume of the one PM block and electrical conductivity of PM. Coefficient of this loss is calculated as 18 kW/m^3 while it is responsible of 0.51% of the total output power of the machine. Related drawing of the eddy current vectors and formula used in the FEA, are given in the related sub-section. In addition, risk of PM demagnetization is investigated and it's found that there is a risk for demagnetization if a three phase short circuit fault occurs between 20° C and 60° C .

According to results of the different stages of FEA evaluations presented in this chapter, it can be concluded that the proposed design of AFPM generator is verified in terms of electromechanical performance. Error rates, phase voltages and harmonic contents of the proposed design were found at an acceptable level.

CHAPTER 6

CONCLUSIONS AND FUTURE WORK

6.1. Proposed Model Comparison

In this section, proposed and verified AFPM generator will be compared with other commercial and academic designs of MW-level wind turbine generator systems in terms of power density (Watt/kg) and torque density (Nm/kg). Since unreasonable conditions may be encountered when comparing different drivetrain configurations, mostly low-speed direct drive topologies are compared in this section. In Table 6-1, 13 different commercial and academic wind turbine generator designs are listed including the proposed AFPM generator according to their properties. Property that is not provided by the manufacturer, left blank in the table.

It can be inferred from the property comparison table that, the proposed AFPM generator configuration has a reasonable power density level with 41.8 W/kg, considering the other commercial counterparts. Besides, proposed generator has better torque density than other counterparts with 33.3 Nm/kg thanks to its axial length and volume advantages. Due to axial flux configuration lower axial length, modular axial stacking and increased reliability are the main advantages while large outer diameter and dominant structural mass due to direct drive concept are the main disadvantages of the proposed AFPM generator concept. Since the proposed model has an air cored structure, amount of PM material increased by the design optimization in order to provide necessary air gap flux density. Since wind turbine manufacturers do not share specific data related to magnet mass, axial length of generator or structural mass, exact comparison of these components is not made in this section. The proposed AFPM generator configuration can be preferred by the market especially when modular construction and reliability issues are taken into account.

Table 6-1. Properties of commercially and academically designed wind turbine generator systems including the proposed generator

Model	Type	Power (MW)	Speed (rpm)	Torque (kNm)	Mass (tonne)	Power Density (W/kg)	Torque Density (Nm/kg)
Thesis/Proposed	DD-PMSG	5	12	3980	119.4	41.8	33.3
Harokasan [108]	DD-PMSG	1.5	18	796	47.2	31.7	16.8
Newgen [109]	DD-PMSG	4	19	2011	36.4	109.8	55.2
NREL-AMSC [110]	DD-PMSG	3.1	12.5	2370	90	34.4	26.3
Bang et. al. [111]	DD-TFPM	5	12	3980	90.8	55	43.8
NTNU Thesis [109]	DD-PMSG	10	13	7347	260	38.4	28.2
NREL-AMSC [110]	DD-PMSG	6	12.3	4658	177	33.9	26.3
NREL-AMSC [110]	DD-PMSG	10	11.5	8305	315	31.7	26.3
Bang et al. [112]	DD-PMSG	10	10	9551	325	30.7	29.3
Enercon/E-126-7580 [15]	DD-EESG	7.58	12	6035	220	34.4	27.4
The Switch/PMG4250-16 [113]	DD-PMSG	4.25	16	2537	89	47.7	28.5
The Switch/PMG3200-12 [113]	DD-PMSG	3.20	12	2547	80	40	31.8
The Switch/PMG1650-17 [113]	DD-PMSG	1.65	17	926	50	33	18.5

6.2. Conclusions

With the increased capacities and interconnected electrical networks of wind turbines worldwide, reliability, fault-tolerance and modularity terms have gained importance. As a result of this, wind power plants have become inevitable parts of grids even in failure times. Main motivation of this thesis work is to design a modular direct drive axial-flux permanent magnet (AFPM) generator for wind turbine applications due to its higher energy yield, higher torque density and volume advantages.

In the first chapter, general overview of wind turbine trends and statistics are presented for both in Turkey and worldwide. It's concluded that worldwide trend is going through power output of 10 MW and above in the near future. Moreover, conventional wind turbine practices are changed from fixed speed, low power systems to high power per turbine, reliable and grid-supportive systems.

In Chapter 2, we mainly focused on wind energy conversion systems. Firstly, fundamental equations of wind power harvesting are defined and presented. Then, common challenges of the wind power conversion systems are investigated. According to statistics and literature, main reasons of longest downtimes and failures of wind turbines are gearbox and drivetrain failures. Main disadvantage of direct drive systems are larger outer diameters and mass in order to achieve higher torque values under same power levels. After these findings, existing wind energy conversion technologies and various wind turbine generator concepts are investigated in the literature. Among these generator types doubly-fed induction generators are very popular due to its lower price and experience in both in field and production. However, this type of generator suffers from their partial scale (around 20-30% of generator power) converters and gearbox, considering the grid support and efficiency, respectively. Direct drive permanent magnet synchronous generators (PMSG-DD) are found more reliable and feasible solution in terms of efficiency, reliability and fault-ride-through capability. Thus, direct drive PMSG is chosen for the proposed design in this study. Axial flux orientation is selected and implemented in this thesis study because of its modularity and axial length advantages. Detailed overview of selected topology was given in related sections. For the final part of this

chapter, effects of modularity in modern WECs are discussed and modular concept is chosen, considering the increased importance of modularity and reliability under LVRT conditions.

In the third chapter, analytical design calculations of the proposed AFPM generator and its 50 kW sample FEA verifications are mentioned. For this purpose, detailed mechanical and electromagnetic design equations are described and related drawings are given with corresponding design parameters. In the proposed model outer rotor and C-core configurations are selected. There is a 4/3 ratio between coil pitch and pole pitch, considering the maximum induced voltage. Moreover, magnetic circuit including leakage flux paths are presented and related equations are defined. Leakage coefficient of 0.95 is used for the flux linkage calculations. This value is determined according to finite element analysis results. For the PM excitation of rotor N50 grade NdFeB material, whose remanent flux density value is 1.4 T, is selected. In the proposed design, power factor is assumed as unity due to selected vector control in the power electronics stage, which is out of scope of this thesis. Structural deflection between C-core limbs due to strong magnetic forces, is also modelled in this thesis. Thermal calculations are based on temperature reference ($7A/mm^2$ @100°C) under predetermined current density value according to literature while assuming the ambient temperature is 20°C. Active and structural mass calculations are again presented in this chapter. Eight rotor bars and six stator bars are used for the structural support design of the generator. Eddy losses are calculated analytically for both magnets and windings. For magnet eddy loss calculation, a coefficient of $18 \text{ kW}/m^3$ is used, whose value is determined according to FEA eddy loss calculations. Finally in this chapter, a sample 50 kW AFPM generator is optimized and design method accuracy is tested via FEA. Air gap flux density and induced emf values are chosen for error comparison. According to low error values (3% for air gap flux density and 6.5% for induced emf) between analytical and FEA results, design methodology is considered as a verified method for the proposed AFPM generator.

Fourth chapter mainly describes the implementation of genetic algorithm based optimization and optimized parameters of the 5MW 12 rpm AFPM generator.

Proposed design method followed in this thesis can be described as a cost optimization procedure which is based on analytical design equations presented previously and wind speed time probabilistic for a given site. Proposed optimization procedure determines the 15 different design parameters of the proposed generator. In order to achieve more realistic optimization conditions and more realistic design results, real field based wind speed distributions (taken from a WPP located in Çanakkale/TURKEY) are used in the optimization method. Candidate individuals of the optimization are subjected to 9 different wind speed values in order to determine the optimum solution under not only for the rated speed of 12 rpm but also for the other operation speeds. A real commercial Gamesa wind turbine power production conditions are referenced in this optimization study. Optimum 5 MW 12 rpm AFPM design parameters are found by implementing the proposed method in MATLAB GA toolbox. In this optimization procedure, energy production income according to real wind probabilistic are taken into account. In addition, penalty constraints and phase voltage levels are selected according to real life requirements. Optimization algorithm evaluates the candidate individual current density values and adjust this in order to continue process. Details of the algorithm and performance parameters of the optimum generator is given in this chapter.

10 mm air gap value is selected according to pre-limited stator outer diameter and machine design practices. Seven different penalty functions are employed in order to search for a better optimization result and convert our constrained optimization problem to an unconstrained optimization problem. Optimized generator has an outer diameter of approximately 10 meters and has 6 axial stacks in parallel. According to optimized generator performance results, the most dominant mass component of the generator is the structural mass by 61% while the material cost is less dominant. In addition, PM cost is the most dominant compound of the cost of the generator while it is the least dominant mass component. This can be considered as a disadvantage of the design, as it was predicted before. Therefore, it can be inferred that, optimization algorithm tried minimize the amount of PM used, for the sake of a cheaper solution. Resultant generator has a large outer diameter due to its direct drive nature but very advantageous in axial length aspect. This length advantage is used by the optimization and the optimum design is determined as six-

parallel axially stacked AFPM generators, which gives modular ability and huge advantage in terms of transportation, installation and repair costs. Optimized generator has an efficiency of 95.4%. The material cost and the total cost (including approximately 20% labor cost) are calculated as \$ 1.30 M and \$ 1.56 M, respectively. Total mass is calculated as 119.4 tonne. Total electricity generation is estimated as 11.73 GWh while the annual generation income is found as \$ 857 k.

In the fifth chapter, FEA verification of the proposed 5MW 12 rpm AFPM generator was the main motivation. For this purpose, a parametric model based on the optimized analytical design results is created in Maxwell 3D environment. Air gap flux density and phase voltages are investigated by using magnetostatic and transient analyses. According to these simulation results, it's concluded that air gap flux density and phase voltages are verified by the error rates of under 3% and 2%, respectively. Sinusoidal variation of the flux density in the airgap is shown and flux density vectors are depicted. Also in this chapter coefficient of eddy loss, which acts on magnets, is estimated as 18 kW/m³. Magnet eddy losses in this design was founded responsible for the 0.51% of the total output power of 5MW. In the full load verification, THD values of the phase voltages is found around 2%, which supports the harmonic control standards. In the calculation stage of the phase voltages of the FEA, difference between phase inductances do not affect the resultant voltage because proposed generator has an air cored structure and low speed application. Besides, PM demagnetization is investigated through the FEA simulations by considering a three phase short circuit fault condition. It's found that there is a risk of demagnetization of PMs in case of a three phase short circuit fault occurs between 20°C and 60°C . Main reason of the high short circuit currents (peak of around 3 kA) is air cored structure and hence low inductance (1.04 mH) values, which are expected.

In the earlier sections in the Chapter 6, comparison of proposed and verified generator with commercial wind turbine generator counterparts in terms of power density and torque density. Mostly, similar power level and generator topologies are chosen. According to comparison tables of the generators, power density of proposed AFPM generator is calculated as 41.8 W/kg while the torque density is

found as 33.3 Nm/kg. It's concluded that when compared with other counterparts, proposed generator has reasonable power density and better torque density among them, considering the modularity and reliability advantages.

To sum up, a modular direct drive AFPM generator is analytically designed, optimized under realistic conditions and verified by FEA in this thesis study. This topology is selected due to its higher energy yield, higher efficiency, reliability and axial length advantages. Modular design of the proposed generator allows easier and cheaper transportation, installation and repair conditions thanks to its lighter total mass per axially-stacked machine configuration. Direct drive allows generator to operate more efficient due to eliminated gearbox. However, large outer diameter, which is optimized as 10 meters in this design, and highly magnet price dependent overall cost are the biggest challenges for the proposed design.

6.3. Future Work

Several points can be considered in order to improve the proposed AFPM generator in this study:

- **Detailed Thermal Network:** In this study, optimization is forced to higher efficiency values because of simple thermal approach followed during the design. However, a more detailed thermal network of the generator can be studied for a more realistic design optimization. In addition, thermal flow analysis can be implemented for the design.
- **FEA integrated optimization:** Optimization and FEA verification stages are separated in this study. Therefore, any mistake in the optimization procedure could be understood at the final stage, which makes the overall procedure longer and inefficient. Instead, Maxwell and MATLAB environments can be linked together for the integrated optimization-FEA processes.
- **Prototype testing:** Like the most of the real machine design procedures, low-scale prototype production and testing in a real life conditions after the FEA verification can result in better designed generators in terms of electromechanical and thermal means.

REFERENCES

- [1] S. Debnath and M. Saeedifard, "A new hybrid modular multilevel converter for grid connection of large wind turbines," *IEEE Trans. Sustain. Energy*, vol. 4, no. 4, pp. 1051–1064, 2013.
- [2] S. Debnath, J. Qin, B. Bahrani, M. Saeedifard, and P. Barbosa, "Operation, Control, and Applications of the Modular Multilevel Converter: A Review," *IEEE Trans. Power Electron.*, vol. PP, no. 99, pp. 1–1, 2014.
- [3] P. Samuel, R. Gupta, and D. Chandra, "Grid Interface of Wind Power With Large Split-Winding Alternator Using Cascaded Multilevel Inverter," *IEEE Trans. Energy Convers.*, vol. 26, no. 1, pp. 299–309, Mar. 2011.
- [4] Global Wind Energy Council (GWEC), "Global Wind Statistics Report 2016," 2016.
- [5] Global Wind Energy Council (GWEC), "Global Wind Report Annual Market Update 2015," 2015.
- [6] TÜREB, "Türkiye Rüzgar Enerjisi İstatistik Raporu," 2017.
- [7] V. Yaramasu, B. Wu, P. C. Sen, S. Kouro, and M. Narimani, "High-power wind energy conversion systems: State-of-the-art and emerging technologies," *Proc. IEEE*, vol. 103, no. 5, pp. 740–788, 2015.
- [8] F. Blaabjerg, "Future on Power Electronics for Wind Turbine Systems," *IEEE J. Emerg. Sel. Top. Power Electron.*, vol. 1, no. 3, pp. 139–152, 2013.
- [9] E. Muljadi, C. P. Butterfield, and Y. huie Wan, "Axial-flux modular permanent-magnet generator with a toroidal winding for wind-turbine applications," *IEEE Trans. Ind. Appl.*, vol. 35, no. 4, pp. 831–836, 1999.
- [10] A. Grauers, "Design of Direct-driven Permanent-magnet Generators for Wind Turbines," Chalmers University of Technology, PhD Thesis, 1996.
- [11] DNV/Risø, *Guidelines for design of wind turbines*, Second Edi. Det Norske Veritas, Copenhagen and Wind Energy Department, Risø National

Laboratory, 2002.

- [12] R. Zeinali, “Design and Optimization of High Torque Density Generator for Direct Drive Wind Turbine Applications,” METU,MS thesis, 2016.
- [13] P. Lampola, “Directly Driven, Low-Speed Permanent-Magnet Generators for Wind Power Applications,” 2000.
- [14] “Products-Sinovel Wind Group Co., Ltd.” [Online]. Available: http://www.sinovel.com/english/list/?43_1.html. [Accessed: 30-Dec-2017].
- [15] “Products-Enercon.” [Online]. Available: <https://www.enercon.de/en/products/>. [Accessed: 30-Dec-2017].
- [16] “Products-Vestas.” [Online]. Available: <https://www.vestas.com/en/products>. [Accessed: 30-Dec-2017].
- [17] “Wind Turbines | GE Renewable Energy.” [Online]. Available: <https://www.gerenewableenergy.com/wind-energy/turbines>. [Accessed: 30-Dec-2017].
- [18] “Siemens Gamesa / Products and services / Wind turbines / Catalogue.” [Online]. Available: <http://www.siemensgamesa.com/en/products-and-services/wind-turbines>. [Accessed: 30-Dec-2017].
- [19] “Classic Fleet – Suzlon.” [Online]. Available: <http://www.suzlon.com/products/classic-feet>. [Accessed: 30-Dec-2017].
- [20] “Nordex: Wind turbines.” [Online]. Available: <http://www.nordex-online.com/en/products-services/wind-turbines.html>. [Accessed: 30-Dec-2017].
- [21] “Siemens - Wind Power Turbines and Services - Siemens - Wind Energy - Siemens Global Website.” [Online]. Available: <https://www.siemens.com/global/en/home/markets/wind/turbines-and-services.html>. [Accessed: 30-Dec-2017].
- [22] “Alstom launches the ECO 110 wind turbine - A 3MW turbine with a rotor of 110 metres to maximize energy yield on low to medium wind sites.”

- [Online]. Available: <http://www.alstom.com/press-centre/2010/6/Alstom-launches-ECO-100-wind-turbine/>. [Accessed: 30-Dec-2017].
- [23] “Wind Turbines | servion.com.” [Online]. Available: <https://www.servion.com/global/en/products-services/wind-turbines/>. [Accessed: 30-Dec-2017].
- [24] “Goldwind |.” [Online]. Available: <http://www.goldwindamericas.com/>. [Accessed: 06-Feb-2018].
- [25] Y. Xia, K. H. Ahmed, and B. W. I. E. I. T. on Williams, “Wind Turbine Power Coefficient Analysis of a New Maximum Power Point Tracking Technique,” *IEEE Trans. Ind. Electron.*, vol. 60, no. 3, pp. 1122–1132, 2013.
- [26] F. G. Rossouw, “Analysis and Design of Axial Flux Permanent Magnet Wind Generator System for Direct Battery Charging Applications,” Stellenbosch University, Ms Thesis, 2009.
- [27] Windy Nation, “tip-speed-ratio-how-calculate-and-apply-tsr-blade-selection - Web.” [Online]. Available: <https://www.windynation.com/jzv/inf/tip-speed-ratio-how-calculate-and-apply-tsr-blade-selection>. [Accessed: 30-Dec-2017].
- [28] METU Aerospace Engineering Lecture Notes, “Rüzgar Türbinleri Bölüm 1:Tasarım Kuralları.” [Online]. Available: <http://www.ae.metu.edu.tr/~ae462/12/IEC 61400-1.pdf>. [Accessed: 30-Dec-2017].
- [29] A. N. Celik, “Review of Turkey’s current energy status: A case study for wind energy potential of Çanakkale province,” *Renew. Sustain. Energy Rev.*, vol. 15, no. 6, pp. 2743–2749, 2011.
- [30] H. Polinder, “Overview of and trends in wind turbine generator systems,” *IEEE Power Energy Soc. Gen. Meet.*, pp. 1–8, 2011.
- [31] D. J. Bang, H. Polinder, G. Shrestha, and J. A. Ferreira, “Promising direct-drive generator system for large wind turbines,” *EPE J. (European Power*

Electron. Drives Journal), vol. 18, no. 3, pp. 7–13, 2008.

- [32] H. Polinder, F. F. a. Van Der Pijl, G.-J. De Vilder, and P. J. Tavner, “Comparison of Direct-Drive and Geared Generator Concepts for Wind Turbines,” *IEEE Trans. Energy Convers.*, vol. 21, no. 3, pp. 725–733, Sep. 2006.
- [33] S. Engstrom and S. Lindgren, “Design of NewGen direct drive generator for demonstration in a 3.5 MW Wind Turbine,” *EWEC (European Wind Energy Conf. Exhib. Milan, Italy, May 7-10)*, no. 1, pp. 1–7, 2007.
- [34] J. F. Gieras, R.-J. Wang, and M. J. Kamper, *Axial Flux Permanent Magnet Brushless Machines*, vol. 3 ed. Dordrecht: Springer Netherlands, 2008.
- [35] G. A. M. van Kuik, J. Peinke, R. Nijssen, D. Lekou, J. Mann, J. N. Sørensen, C. Ferreira, J. W. van Wingerden, D. Schlipf, P. Gebraad, H. Polinder, A. Abrahamsen, G. J. W. van Bussel, J. D. Sørensen, P. Tavner, C. L. Bottasso, M. Muskulus, D. Matha, H. J. Lindeboom, S. Degraer, O. Kramer, S. Lehnhoff, M. Sonnenschein, P. E. Sørensen, R. W. Künneke, P. E. Morthorst, and K. Skytte, “Long-term research challenges in wind energy – a research agenda by the European Academy of Wind Energy,” *Wind Energy Sci.*, vol. 1, no. 1, pp. 1–39, 2016.
- [36] H. Li and Z. Chen, “Overview of different wind generator systems and their comparisons,” *IET Renew. Power Gener.*, vol. 2, no. 2, pp. 123–138, 2008.
- [37] Danish Wind Industry Association, “Wind Turbines: Upwind or Downwind Machines?” [Online]. Available: http://drømstørre.dk/wp-content/wind/miller/windpower_web/en/tour/design/updown.htm. [Accessed: 30-Dec-2017].
- [38] O. P. Mahela and A. G. Shaik, “Comprehensive overview of grid interfaced wind energy generation systems,” *Renew. Sustain. Energy Rev.*, vol. 57, pp. 260–281, 2016.
- [39] X. Yang, D. Patterson, and J. Hudgins, “Permanent magnet generator design and control for large wind turbines,” *2012 IEEE Power Electron. Mach.*

Wind Appl., pp. 1–5, 2012.

- [40] M. Liserre, R. Cardenas, M. Molinas, J. Rodriguez, R. Cárdenas, M. Molinas, J. Rodríguez, R. Cardenas, M. Molinas, and J. Rodriguez, “Overview of Multi-MW Wind Turbines and Wind Parks,” *IEEE Trans. Ind. Electron.*, vol. 58, no. 4, pp. 1081–1095, 2011.
- [41] H. Polinder, J. A. Ferreira, B. B. Jensen, A. B. Abrahamsen, K. Atallah, and R. a. McMahon, “Trends in Wind Turbine Generator Systems,” *IEEE J. Emerg. Sel. Top. Power Electron.*, vol. 1, no. 3, pp. 174–185, 2013.
- [42] C. V. Hernández, T. Telsnig, and Anahí Villalba Pradas, “JRC Wind Energy Status Report 2016 Edition,” Petten, The Netherlands, 2016.
- [43] H. Li and Z. Chen, “Overview of different wind generator systems and their comparisons,” *IET Renew. Power Gener.*, vol. 2, no. 2, p. 123, 2008.
- [44] “Official Website of Enercon GmbH.” [Online]. Available: https://www.enercon.de/fileadmin/_processed_/csm_titel_ep4_1d94c9e268.png. [Accessed: 30-Dec-2017].
- [45] M. Cheng and Y. Zhu, “The state of the art of wind energy conversion systems and technologies: A review,” *Energy Convers. Manag.*, vol. 88, pp. 332–347, 2014.
- [46] “Innovations | Offshore Wind Turbines | MHI Vestas™.” [Online]. Available: <http://www.mhivestasoffshore.com/innovations/>. [Accessed: 30-Dec-2017].
- [47] Wind Energy Facts, “Alternative drive train configurations.” [Online]. Available: <https://www.wind-energy-the-facts.org/alternative-drive-train-configurations.html>. [Accessed: 30-Dec-2017].
- [48] J. N. Stander, G. Venter, and M. J. Kamper, “Review of direct-drive radial flux wind turbine generator mechanical design,” *Wind Energy*, vol. 15, no. 3, pp. 459–472, Apr. 2012.
- [49] O. Kütük, “Rüzgar Türbinleri İçin Doğrudan Sürürlü Sürekli Mıknatıslı

Senkron Generator Tasarımı,” İTÜ, Ms Thesis, 2011.

- [50] M. N. Uddin, S. Kahourzade, A. Mahmoudi, H. W. Ping, and N. A. Rahim, “Design and prototyping of an optimised axial-flux permanent-magnet synchronous machine,” *IET Electr. Power Appl.*, vol. 7, no. 5, pp. 338–349, 2013.
- [51] A. Parviainen, M. Niemela, J. Pyrhonen, and J. Mantere, “Performance comparison between low-speed axial-flux and radial-flux permanent-magnet machines including mechanical constraints,” *IEEE Int. Conf. Electr. Mach. Drives, 2005.*, pp. 1695–1702, 2005.
- [52] F. Giulii Capponi, G. De Donato, and F. Caricchi, “Recent advances in axial-flux permanent-magnet machine technology,” *IEEE Trans. Ind. Appl.*, vol. 48, no. 6, pp. 2190–2205, 2012.
- [53] F. Caricchi, F. Crescimbeni, E. Fedeli, and G. Noioa, “Design and construction of a wheel-directly-coupled axial-flux PM motor prototype for EVs,” *Proc. 1994 IEEE Ind. Appl. Soc. Annu. Meet.*, pp. 254–261, 1994.
- [54] F. Sahin, “Design and development of an high-speed axial-flux permanent-magnet machine,” Eindhoven University of Technology, PhD Thesis, 2001.
- [55] A. Mahmoudi, N. a. Rahim, and W. P. Hew, “Axial-flux permanent-magnet machine modeling, design, simulation and analysis,” *Sci. Res. Essays*, vol. 6, no. 12, pp. 2525–2549, 2011.
- [56] S. Kahourzade, A. Mahmoudi, H. W. Ping, and M. N. Uddin, “A comprehensive review of axial-flux permanent-magnet machines,” *Can. J. Electr. Comput. Eng.*, vol. 37, no. 1, pp. 19–33, 2014.
- [57] M. Aydin, S. Huang, and T. Lipo, “Axial flux permanent magnet disc machines: a review,” 2004.
- [58] F. Profumo, A. Tenconi, Z. Zhang, and A. Cavagnino, “Novel axial flux interior PM synchronous motor realized with powdered soft magnetic materials,” *Conf. Rec. 1998 IEEE Ind. Appl. Conf. Thirty-Third IAS Annu. Meet. (Cat. No.98CH36242)*, vol. 1, pp. 152–158, 1998.

- [59] F. Profumo, A. Tenconi, Z. Zhang, and A. Cavagnino, "Design and realization of a novel axial flux interior PM synchronous motor for wheel-motors applications," *Electr. Mach. Power Syst.*, vol. 28, no. 7, pp. 637–649, 2000.
- [60] J. S. Hsu, D. J. Adams, and USPatent:5952756, "Permanent Magnet Energy Conversion Machine With Magnet Mounting Arrangement," 1999.
- [61] A. Chen, R. Nilssen, and A. Nysveen, "Performance comparisons among radial flux, multi-stage axial flux and three-phase transverse flux pm machines for downhole applications," *2009 IEEE Int. Electr. Mach. Drives Conf. IEMDC '09*, pp. 1010–1017, 2009.
- [62] A. E. Fitzgerald, J. Charles Kingsley, and S. D. Umans, *Electric machinery*, Sixth. McGraw-Hill Higher Education, 2003.
- [63] O. Keysan, A. S. McDonald, and M. Mueller, "Integrated Design and Optimization of a Direct Drive Axial Flux Permanent Magnet Generator for a Tidal Turbine," in *International Conference on Renewable Energies and Power Quality - ICREPQ'10*, 2010.
- [64] A. Parviainen, M. Niemelä, and J. Pyrhönen, "Modeling of axial flux permanent-magnet machines," *IEEE Trans. Ind. Appl.*, vol. 40, no. 5, pp. 1333–1340, 2004.
- [65] J. F. Gieras and M. Wing, *Permanent Magnet Motor Technology: design and applications*, 2nd Ed. Marcel Dekker, Inc, 2002.
- [66] T. F. Chan and L. L. Lai, "An axial-flux permanent-magnet synchronous generator for a direct-coupled wind-turbine system," *IEEE Trans. Energy Convers.*, vol. 22, no. 1, pp. 86–94, 2007.
- [67] A. S. McDonald, "Structural analysis of low speed, high torque electrical generators for direct drive renewable energy converters," University of Edinburgh, PhD Thesis, 2008.
- [68] O. Keysan, A. S. McDonald, and M. Mueller, "A direct drive permanent magnet generator design for a tidal current turbine(SeaGen)," *2011 IEEE*

Int. Electr. Mach. Drives Conf. IEMDC 2011, pp. 224–229, 2011.

- [69] “Sintered Neodymium Iron Boron (NdFeB) Magnets.” [Online]. Available: http://www.eclipsemagnetics.com/media/wysiwyg/brochures/neodymium_grades_data.pdf. [Accessed: 09-Aug-2017].
- [70] B. S. Guru and H. R. Hiziroglu, *Electric Machinery and Transformers*, Third Edit. Oxford University Press, 2001.
- [71] J. R. Bumby and R. Martin, “Axial-flux permanent-magnet air-cored generator for small-scale wind turbines,” *IEE Proc. - Electr. Power Appl.*, vol. 152, no. 5, pp. 1065–1075, 2005.
- [72] A. S. McDonald, “Structural analysis of low speed, high torque electrical generators for direct drive renewable energy converters,” University of Edinburgh, UK, 2008.
- [73] H. Polinder, D. Bang, A. S. McDonald, and M. A. Mueller, “10 MW Wind Turbine Direct-Drive Generator Design with Pitch or Active Speed Stall Control,” in *2007 IEEE International Electric Machines & Drives Conference (IEMDC)*, 2007, pp. 1390–1395.
- [74] M. A. Mueller, A. S. McDonald, and D. E. Macpherson, “Structural analysis of low-speed axial-flux permanent-magnet machines,” *IEE Proceedings-Electric Power Appl.*, vol. 152, no. 6, pp. 1417–1426, 2005.
- [75] C. Rans, S. Teixeira, and D. Freitas, “Bending Deflection – Macaulay Step Functions.” [Online]. Available: <https://ocw.tudelft.nl/wp-content/uploads/Deflection-via-step-functions.pdf>. [Accessed: 16-Aug-2017].
- [76] W. C. Young and R. G. Budynas, *Roark’s Formulas for Stress and Strain*, Seventh Ed. McGraw-Hill, 2002.
- [77] “NEMA Insulation Classes.” [Online]. Available: http://www.engineeringtoolbox.com/nema-insulation-classes-d_734.html. [Accessed: 27-Sep-2017].

- [78] “Neodymium Magnets | Arnold Magnetic Technologies.” [Online]. Available: <http://www.arnoldmagnetics.com/en-us/Products/Neodymium-Magnets>. [Accessed: 27-Sep-2017].
- [79] V. Ruuskanen, “Design Aspects of Megawatt-Range Direct-Driven Permanent Magnet,” Lappeenranta University of Technology, PhD Thesis, 2011.
- [80] A. Parviainen, “Design of Axial-Flux Permanent-Magnet Low-Speed Machines and Performance Comparison between Radial-Flux and Axial-Flux Machines,” Lappeenranta University of Technology, PhD Thesis, 2005.
- [81] J. Braid, A. van Zyl, and C. Landy, “Design, analysis and development of a multistage axial-flux permanent magnet synchronous machine,” *Africon Conf. Africa, 2002. IEEE AFRICON. 6th*, vol. 2, pp. 675–680, 2002.
- [82] A. Zavvos, A. S. McDonald, M. Mueller, D. J. Bang, and H. Polinder, “Structural comparison of permanent magnet direct drive generator topologies for 5MW wind turbines,” *Power Electronics, Machines and Drives (PEMD 2012), 6th IET International Conference on*. pp. 1–6, 2012.
- [83] A. S. McDonald, M. A. Mueller, and H. Polinder, “Structural mass in direct-drive permanent magnet electrical generators,” *Renew. Power Gener. IET*, vol. 2, no. 1, pp. 3–15, 2008.
- [84] A. S. McDonald, M. Benatmane, and M. a. Mueller, “A multi-stage axial flux permanent magnet machine for direct drive wind turbines,” *IET Conf. Renew. Power Gener. (RPG 2011)*, vol. 1, 2011.
- [85] E. Spooner, P. Gordon, J. R. Bumby, and C. D. French, “Lightweight ironless-stator PM generators for direct-drive wind turbines,” *IEE Proceedings-Electric Power Appl.*, pp. 17–26, 2005.
- [86] “Miles Platts - E1080701GN6NAT.” [Online]. Available: <http://www.milesplatts.co.uk/product/e1080701/e1080701gn6nat>. [Accessed: 16-Aug-2017].

- [87] T. Gerlach, R. Steckel, T. Hubert, and A. Kremser, “Eddy current loss analysis in permanent magnets of synchronous machines,” in *2016 6th International Electric Drives Production Conference (EDPC)*, 2016, pp. 246–252.
- [88] P. P. Parthasaradhy and S. V Ranganayakulu, “Hysteresis and eddy current losses of magnetic material by Epstein frame method-novel approach,” *Int. J. Eng. Sci. (I)*, pp. 85–93, 2014.
- [89] Umut Güvengir, “Online Application of Shem to Grid-Connected Inverters with Variable DC Link Voltage by Particle swarm Optimization,” METU, MS Thesis, 2014.
- [90] K. M. Leung, “Genetic Algorithms,” 2003. [Online]. Available: <http://cis.poly.edu/~mleung/CS4744/f04/ch06/GA3.pdf>. [Accessed: 16-Aug-2017].
- [91] M. Mitchell, *An introduction to genetic algorithms*. The MIT Press, 1999.
- [92] S. N. Sivanandam and S. N. Deepa, *Introduction to genetic algorithms*. 2008.
- [93] P. Vrtić and M. Vrač, “Design of an Axial Flux Permanent Magnet Synchronous Machine Using Analytical Method and Evolutionary Optimization,” *IEEE Trans. Energy Convers.*, vol. 31, no. 1, pp. 150–158, 2016.
- [94] G. Papa, B. Korousic-Seljak, B. Benedicic, and T. Kmecl, “Universal motor efficiency improvement using evolutionary optimization,” *IEEE Trans. Ind. Electron.*, vol. 50, no. 3, pp. 602–611, Jun. 2003.
- [95] M. Łukaniszyn, M. Jagieła, and R. Wróbel, “Optimization of permanent magnet shape for minimum cogging torque using a genetic algorithm,” *IEEE Trans. Magn.*, vol. 40, no. 2 II, pp. 1228–1231, 2004.
- [96] J. Azzouzi, N. A. Karim, G. Barakat, and B. Dakyo, “Axial flux PM synchronous generator design optimization: robustness test of the genetic algorithm approach,” *2005 Eur. Conf. Power Electron. Appl.*, vol. 9, p. 10

pp.-pp.P.10, 2005.

- [97] “MATLAB Documentation.” [Online]. Available: <https://www.mathworks.com/help/matlab/>. [Accessed: 08-Aug-2017].
- [98] F. G. Capponi, G. De Donato, G. A. Rivellini, and F. Caricchi, “Fractional-Slot Concentrated-Winding Axial-Flux Permanent-Magnet Machine With Tooth-Wound Coils,” *IEEE Trans. Ind. Appl.*, vol. 48, no. 2, pp. 630–641, 2012.
- [99] T. Veflingstad, “Axial flux machines with super high torque density or super high efficiency,” Norwegian University of Science and Technology, MS Thesis, 2014.
- [100] “Rüzgar Santralleri (RES) YEKDEM Geliri.” [Online]. Available: <http://www.enerjiatlasi.com/epias/res-yekdem-geliri>. [Accessed: 23-Oct-2017].
- [101] Gamesa, “Gamesa G128-5 MW Catalog.” [Online]. Available: <http://www.gamesacorp.com/recursos/doc/productos-servicios/aerogeneradores/catalogo-g10x-45mw-eng.pdf>. [Accessed: 12-Oct-2017].
- [102] S. X. Liu, S. Li, and J. He, “Unity Power Factor Control of a Direct-Driven Permanent Magnet Synchronous Wind-Power Generator Based on Three-Level Converter,” *Adv. Mater. Res.*, vol. 347–353, no. m, pp. 2227–2230, Oct. 2011.
- [103] A. Rokke, “Permanent Magnet Generators for Marine Current Tidal Turbines,” Norwegian University of Science and Technology, PhD Thesis, 2017.
- [104] “Nordex Delta Generation Brochure.” [Online]. Available: http://www.nordex-online.com/fileadmin/MEDIA/Produktinfos/EN/Nordex_Delta_Broschuere_en.pdf. [Accessed: 09-Aug-2017].
- [105] “Generators for wind power Proven generators – reliable power.” [Online].

Available: <http://new.abb.com/docs/default-source/ewea-doc/abb-brochure-generators-for-wind-power.pdf?sfvrsn=2>. [Accessed: 09-Aug-2017].

- [106] “Why Magnets Lose Strength | Dura Magnetics.” [Online]. Available: <https://www.duramag.com/techtalk/tech-briefs/why-magnets-lose-strength-the-effects-of-volume-loss-geometry-elevated-temperature-and-demagnetization-from-external-fields/>. [Accessed: 06-Feb-2018].
- [107] S. Sjökvist and S. Eriksson, “Investigation of Permanent Magnet Demagnetization in Synchronous Machines during Multiple Short-Circuit Fault Conditions,” *Energies*, vol. 10, no. 10, p. 1638, 2017.
- [108] Y. Duan and R. G. Harley, “Present and future trends in wind turbine generator designs,” in *2009 IEEE Power Electronics and Machines in Wind Applications*, 2009, pp. 1–6.
- [109] O. Keysan, “Superconducting Generators for Large Offshore Wind Turbines,” The University of Edinburgh, PhD Thesis, 2014.
- [110] B. Maples, M. Hand, and W. Musial, “Comparative Assessment of Direct Drive High Temperature Superconducting Generators in Multi-Megawatt Class Wind Turbines,” 2010.
- [111] D. J. Bang, H. Polinder, G. Shrestha, and J. A. Ferreira, “Ring-shaped transverse flux PM generator for large direct-drive wind turbines,” *Proc. Int. Conf. Power Electron. Drive Syst.*, pp. 61–66, 2009.
- [112] D. Bang, H. Polinder, G. Shrestha, and J. A. Ferreira, “Review of generator systems for direct-drive wind turbines,” *Eur. Wind Energy*, pp. 1–11, 2008.
- [113] “Permanent magnet generators - The Switch.” [Online]. Available: <http://theswitch.com/wind-power/permanent-magnet-generators/>. [Accessed: 07-Feb-2018].
- [114] J. M. PEÑA, “Heuristic Optimization Introduction and Simple Heuristics.” [Online]. Available: <http://mat.uab.cat/~alseda/MasterOpt/IntroHO.pdf>. [Accessed: 16-Aug-2017].